EXPERIMENTAL SETUP FOR FAST BEC GENERATION AND NUMBER-STABILIZED ATOMIC ENSEMBLES

Von der QUEST-Leibniz-Forschungsschule der
Gottfried Wilhelm Leibniz Universität Hannover

zur Erlangung des Grades

Doktor der Naturwissenschaften
- Dr. rer. nat. -

genehmigte Dissertation von

M. Sc. Cebrail Pür

2022

Referent:	apl. Prof. Dr. Carsten Klempt, Institut für Quantenoptik, Leibniz Universität Hannover
Korreferent:	Prof. Dr. Jan Arlt, Department of Physics and Astronomy, Aarhus University
Korreferent:	Dr. Dennis Schlippert, Institut für Quantenoptik, Leibniz Universität Hannover
Tag der Promotion:	04.03.2022

Abstract

Ultracold atomic ensembles represent a cornerstone of today's modern quantum experiments. In particular, the generation of Bose-Einstein condensates (BECs) has paved the way for a myriad of fundamental research topics as well as novel experimental concepts and related applications. As coherent matter waves, BECs promise to be a valuable resource for atom interferometry that allows for high-precision sensing of gravitational fields or inertial moments as accelerations and rotations. In general, the sensitivity of state-of-the-art atom interferometers is fundamentally restricted by the Standard Quantum Limit (SQL). Multi-particle entangled states (e.g. spin-squeezed states, Twin-Fock states, Schrödinger cat states) generated in BECs can be employed to surpass the SQL and shift the sensitivity limit further towards the more fundamental Heisenberg Limit (HL). However, in current real-world atom interferometric applications, ultracold but uncondensed atomic clouds are employed, due to their speed advantage in the sample preparation. The creation of a BEC can take up several tens of seconds, while standard high-precision atom interferometers operate with a cycle rate of several Hz. In addition, the pursued entangled states can be only beneficial if technical noise sources, such as magnetic field or detection noise are not dominating the measurement resolution. These challenges need to be overcome in order to fully exploit the potential sensitivity gain offered by a quantum-enhanced atom interferometer.

This thesis describes the design and implementation of a new experimental setup for Heisenberg-limited atom interferometry, which incorporates a high-flux BEC source and the manipulation and detection of atoms at the single-particle level.

The presented fast BEC preparation includes a high-flux atom source in a double magneto-optical trap (MOT) configuration that allows to collect ^{87}Rb atoms in a 3D-MOT, which is supplied by a 2D$^+$-MOT with 2×10^{10} atoms/s. Forced evaporative cooling of the atoms is divided into two stages, which is sequentially carried out in a magnetic quadrupole trap (QPT) and a crossed-beam optical dipole trap (cODT). The high-flux atom source together with the hybrid evaporation scheme allows to consistently produce BECs with an average of 2×10^5 atoms within 3.5 s.

The capabilities of the single-particle resolving detection are demonstrated by realizing a feedback control loop to stabilize the captured number of atoms in a small MOT. A proof-of-principle measurement is demonstrated for the successful stabilization of a target number of 7 atoms with sub-Poissonian fluctuations. The number noise is suppressed by 18 dB below shot noise, which corresponds to a preparation fidelity of 92%.

Based on this success, the thesis presents an even improved single-particle resolution. The system comprises a six-channel fiber-based optical setup, which provides independent intensity stabilization and frequency detuning, improved pointing stability as well as a better spatial overlap of the MOT beams. The presented high-speed BEC production combined with accurate atom number preparation and detection, as the two main features of the experimental apparatus, pave the way for a future entanglement-enhanced performance of atom interferometers.

Key words: Bose-Einstein condensates, number-stabilized ensembles, quantum-enhanced atom interferometry

Contents

1 Introduction 1

2 Experimental Apparatus 5
- 2.1 Overview of the experimental procedure . . . 5
  - 2.1.1 Preparation . . . 6
  - 2.1.2 Experiment . . . 7
  - 2.1.3 Detection . . . 8
- 2.2 Vacuum system . . . 8
- 2.3 Coil System . . . 10
- 2.4 Laser System . . . 13
  - 2.4.1 Laser system for laser cooling . . . 13
  - 2.4.2 Laser system for optical dipole trapping . . . 15
- 2.5 Microwave setup . . . 17
- 2.6 Detection system . . . 19
- 2.7 Experimental control . . . 20

3 BEC generation with high repetition rates 21
- 3.1 High-flux atom source . . . 22
  - 3.1.1 MOT operation . . . 23
  - 3.1.2 $2D^+$-MOT setup . . . 24
  - 3.1.3 3D-MOT setup . . . 26
  - 3.1.4 $2D^+$-/3D-MOT characterization . . . 29
- 3.2 Hybrid evaporation . . . 33
  - 3.2.1 Magnetic trapping . . . 33
  - 3.2.2 State preparation . . . 35
  - 3.2.3 Loading into the quadrupole trap . . . 37
  - 3.2.4 Radio-frequency evaporation in the quadrupole trap . . . 39
  - 3.2.5 Optical dipole trapping . . . 41
  - 3.2.6 Evaporation efficiency . . . 47
  - 3.2.7 BEC characterization . . . 49

4 Preparation of number-stabilized atomic ensembles 55
- 4.1 Fluorescence detection of individual atoms in a MOT . . . 55
  - 4.1.1 Fluorescence image acquisition . . . 56

- 4.1.2 Atom number estimation . . . 56
- 4.1.3 Characterization and calibration of the detection system . . . 57
- 4.1.4 Noise limitations . . . 59
- 4.2 Atom number stabilization in a MOT . . . 61
  - 4.2.1 Stabilization sequence . . . 61
  - 4.2.2 Loss characterization and preparation fidelity . . . 63

5 Fiber-based detection MOT system **67**
- 5.1 Optical setup of the fiber-based detection MOT . . . 68
- 5.2 Intensity stabilization . . . 72
  - 5.2.1 Feedback control system . . . 72
  - 5.2.2 Radio-frequency setup . . . 73
  - 5.2.3 Photodiode sensors . . . 74
  - 5.2.4 Noise suppression . . . 75
- 5.3 Frequency stabilization . . . 77
  - 5.3.1 Modulation transfer spectroscopy . . . 77
  - 5.3.2 Feedback control system . . . 78
  - 5.3.3 Optical setup of the modulation transfer spectroscopy . . . 79
  - 5.3.4 Modulation transfer spectroscopy sensor signal . . . 81
- 5.4 Preliminary single-atom counting data . . . 84

6 Outlook **91**
- 6.1 Improving the BEC cycle time . . . 91
- 6.2 Improving the new detection system . . . 93

Bibliography **95**

Appendix **113**

A Appendix **113**
- A.1 Summary of the BEC preparation sequence . . . 113
- A.2 Four-wave mixing resonances . . . 114
- A.3 Single-atom counting measurement scaling . . . 114
- A.4 Photodiode schematics . . . 115
- A.5 Six-way intensity stabilization schematics . . . 116

Publications **119**

Curriculum Vitae **121**

Danksagung **123**

Acronyms

Notation	**Description**
AOM	acousto-optic modulator
ARTIQ	Advanced Real-Time Infrastructure for Quantum physics
BEC	Bose-Einstein condensate
CCD	charge-coupled device
CF	ConFlat
cODT	crossed-beam optical dipole trap
CPM	center-position modulation
CW	continuous-wave
DDS	Direct Digital Synthesis
ECDL	external cavity diode laser
FMS	frequency modulation spectroscopy
FPGA	field-programmable gate array
FWHM	full width at half maximum
FWM	four-wave mixing
HL	Heisenberg Limit
IGBT	insulated-gate bipolar transistor
IGP	ion getter pump
LIAD	light-induced atomic desorption
LO	local oscillator
LTI	Linear Time-Invariant
MOT	magneto-optical trap
MTS	modulation transfer spectroscopy
PBS	polarizing beam splitter
PCB	printed circuit board
PCI	Peripheral Component Interconnect

Notation	**Description**
PID	Proportional-Integral-Derivative
PM	polarization-maintaining
PSD	phase space density
QPT	quadrupole trap
QUIC	quadrupole-Ioffe-configuration
RF	radio frequency
SQL	Standard Quantum Limit
TA	tapered amplifier
TOF	time-of-flight
TOP	time-averaged-orbiting-potential
TSP	titanium sublimation pump
UHV	ultra-high vacuum
VCA	voltage-controlled attenuator

CHAPTER 1

Introduction

The foundation of quantum mechanics in the beginning of the last century lead to a substantial change from the paradigm of classical mechanics and opened up a groundbreaking perspective for understanding and perceiving physical reality, as it prevails to this date [1]. Intriguing, but counter-intuitive concepts as *particle-wave duality* [2], *superposition* and *entanglement* [3] emerged from the underlying theory. The attempt to observe and understand nature by the new set of rules had put the seed for the so-called *first quantum revolution.* In the last 100 years, this knowledge brought incredible scientific and technological breakthroughs that underpin modern society as we experience today. The progress of semiconductor electronics, lasers and fiber optics are among the hallmarks of this first-generation quantum technologies.

Since the turn of the millennium, the technological progress has also improved scientific approach to take advantage of the quantum principles in order to explore new systems from the single-particle level up to the mesoscopic domain. The preparation, control and measurement of such many-particle quantum systems lay the first stone towards the development of new quantum technologies. The *second quantum revolution* is now thriving through the emerging field of quantum engineering. In order to construct technologies based on the laws of quantum physics, a set of required tools have been identified and conceptualized [4]. The main pillars quantum information, quantum communication, quantum simulation and quantum metrology will be at the heart of new emerging technologies.

As one of the fields, quantum metrology sets the keystone for novel quantum technologies aiming at high-precision measurements. In this context, interferometers belong to today's most precise measurement tools and are extensively used for a variety of metrological tasks, such as sensing accelerations [5–7], rotations [8–11], magnetic fields [12] or time [13, 14]. However, the sensitivity of state-of-the-art atom interferometers is fundamentally limited by quantum fluctuations, which is a consequence of uncorrelated particle states. The so-called Standard Quantum Limit $\Delta\varphi \geq 1/\sqrt{N}$ can only be beaten by employing entangled states that shift the sensitivity limit towards the ultimate Heisenberg Limit $\Delta\varphi \geq 1/N$ [15]. The most prominent example for quantum-enhanced interferometry was demonstrated by a large-scale, earthbound gravitational wave detector [16], which had successfully detected gravitational waves by employing squeezed states of light [17, 18]. Up to this date, the gain in interferometric sensitivity was also explored for numerous other systems including trapped ions [19–25], cold thermal atoms [26–36] and Bose-Einstein condensates [37–46].

BECs promise to be a valuable resource for quantum-enhanced interferometry, since they offer nonlinear interactions as spin-changing collisions [47, 48] or one-axis twisting [49] to generate entangled states, such as spin-squeezed states [50] or Twin-Fock states [51]. Additionally, BECs offer low expansion rates and superior mode control. Because of the magnetically sensitive internal spin states, suitable applications can be found for example in magnetometry [52, 53]. It was also recently demonstrated that in a BEC the entanglement can be transferred from the spin degree of freedom to two distinct spatially separated modes [54–56] or momentum states [57], paving the way for enhanced inertial and gravitational sensing.

Many applications of high-precision atom interferometers using BECs require short preparation times. The preparation time is defined as the dead time of the interferometric sensor and affects its bandwidth and its vulnerability to technical or environmental noise sources. In addition, the preparation time often predominates the rate of data acquisition, preventing short averaging times and high cycle rates. The preparation of BECs is typically a very time consuming part compared to non-condensed atomic clouds. It can be generally regarded as a two-step process and defined by the time needed to supply a sufficient initial number of laser cooled atoms and the time needed for evaporative cooling. Over the last decades, different strategies have been followed to generate Bose-Einstein condensates for various species of neutral atoms. A summary of different techniques that demonstrated to produce BECs with a final condensed fraction of atom numbers as a function of the total experimental cycle time is illustrated in Fig. 1.1 and the corresponding references are listed in Table 1.1.

One of the first BECs had been achieved with the pioneering work on magnetic trapping and evaporative cooling in a harmonic potential [74, 78]. Magnetic traps typically consist of large coil configurations driven by electrical currents that provide large trapping volumes to efficiently load laser-cooled atoms. The symmetric linear potential offers efficient evaporative cooling. However, a tighter confinement and thus faster cooling rate often leads to an increased power consumption, which usually limits the preparation time to several tens of seconds [75, 65]. In addition, the number of condensed atoms in a magnetic quadrupole trap suffers from unwanted Majorana spin-flip losses [79] at lower temperatures, which limit the achievable phase-space density.[1] These limitations are relaxed in compact atom-chip-based experiments, where the high-gradient trapping fields are produced by micrometer-sized wire structures on the chip surface. Because of the proximity and therefore faster switching times there is almost no cost in terms of power consumption [58–62]. The superior performance of atom-chip experiments exhibits by far the fastest BEC production time with a reasonable final number of atoms. The highest reported flux

---

[1] This limitation can be overcome by employing a blue-detuned optical plug [80] or other trapping schemes as a time-averaged-orbiting-potential (TOP) trap [81], a Ioffe-Pritchard trap [82] or a quadrupole-Ioffe-configuration (QUIC) trap [83].

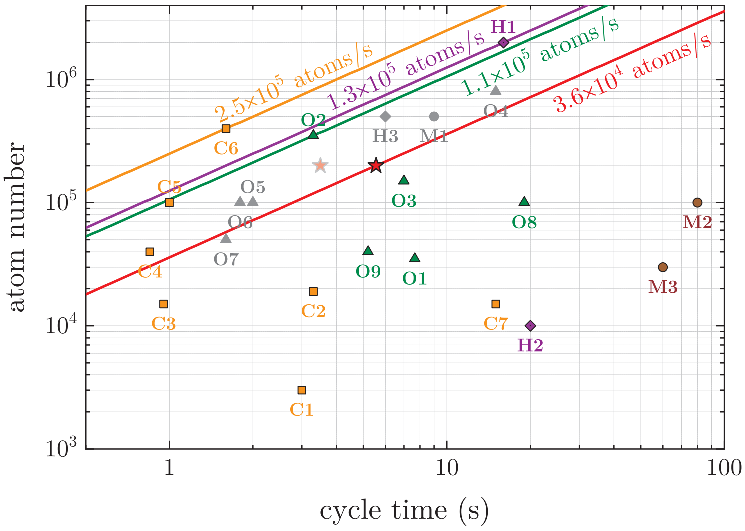

Atom chip evaporation		
C1	[58]	Horikoshi et al., 2006
C2	[59]	Farkas et al., 2010
C3	[60]	Farkas et al., 2014
C4-6	[61]	Rudolph et al., 2015
C7	[62]	Abend et al., 2016
Hybrid evaporation		
H1	[63]	Lin et al., 2009
H2	[64]	Zaiser et al., 2011
H3	[65]	Bouton et al., 2015
All optical evaporation		
O1	[66]	Barrett et al., 2001
O2	[67]	Kinoshita et al., 2005
O3	[68]	Clément et al., 2009
O4	[69]	Landini et al., 2012
O5	[70]	Stellmer et al., 2013
O6-7	[71]	R. Roy et al., 2016
O8	[72]	Xie et al., 2018
O9	[73]	Condon et al., 2019
All magnetic evaporation		
M1	[74]	Davis et al., 1995
M2	[75]	Ernst et al., 1998
M3	[76]	Arlt et al., 1999

Figure 1.1 & Table 1.1: Overview of experimentally demonstrated BEC cycle times and final atom numbers. Logarithmic map comparing the production time and the final atom number of various BEC sources for different experimental realizations. Orange squares are atom-chip-based experiments, brown circles correspond to magnetically trapped ensembles, green triangles show all optical (static and dynamic) evaporation and purple diamonds represent hybrid, two-staged methods, which combine magnetic and optical evaporation. Grayed out data points mark atom sources other than ^{87}Rb. The corresponding publications are referenced by the accompanied table on the right hand side of the figure. The red star marks the BEC cycle time reported in this thesis. The transparent red star depicts the scenario for a reduced waiting time without a heating of the magnetic trap coils. The diagonal lines give the production rates for the corresponding experiments with respect to the highest achieved final atom number. Adapted from Ref. [77] and extended.

is 2.5×10^5 atoms/s. The only drawback is that atom chips as well employ magnetic fields for trapping, which limits them to only magnetically sensitive atomic states. In contrast, optical dipole traps can host atoms regardless of their magnetic moment [66–73], which allow to manipulate their internal states.[1] The tight confinement of optical dipole traps generally allows a good evaporation efficiency. The evaporation in static optical dipole traps is usually forced by lowering the laser power, which leads to a mutual reduction of the trap depth and the confinement. Additionally, a typical problem is the efficient loading of laser-cooled atoms into a small-volume optical dipole trap. A compromise must be found between the spatial size and a high collision rate. This problem is addressed by dynamical optical dipole trap configurations that try to transform an initial large-volume trap into a deep small-volume trap during evaporation [84]. Alternatively, time-averaged "painted" potentials generated by center-position modulated optical dipole beams have also been demonstrated [71]. The highest flux for all-optical and dynamical evaporation was achieved by Ref. [67] and corresponds to 1.1×10^5 atoms/s.

---

[1] This is particularly a key necessity to generate entangled states for quantum-enhanced atom interferometry.

In this thesis, a two-stage hybrid evaporation scheme following the proposal by Ref. [85] is used, which was previously demonstrated by a different workgroup that achieved a flux of 1.3×10^5 Hz [63]. The evaporation scheme takes the advantages of both magnetic and optical dipole traps, namely the large initial trapping volume and tight confinement of the magnetic trap and the fast evaporation in the optical dipole trap. The underlying apparatus consistently produces BECs every 5.6 s, which corresponds to a flux of 3.6×10^4 Hz. The current BEC cycle time is technically limited by the waiting time for the magnetic traps to cool down, due to a large power consumption.

The preparation process of BECs is in general of probabilistic nature. The high-flux BEC operation only allows to reach the intended statistical uncertainties in shorter averaging times, but does not reduce them. The preparation of the anticipated Quantum states requires high fidelity, in order to harness their full potential. Especially in the context of quantum-enhanced atom interferometry, the suppression of initial number fluctuations will help to generate pure non-classical quantum states instead of mixed states. The search for deterministic preparation of single particles up to mesoscopic ensembles has lead to several proof-of-principle demonstrations in different systems. One example is the loading of a few Cs atoms from a magneto-optical trap into an optical dipole trap with 100% efficiency. Single Cr atoms were loaded with a 98.7% occupation probability into a magneto-optical trap by applying feedback through the recorded fluorescence signal [86, 87]. Larger ensembles of 10^6 ^{87}Rb atoms inside a magnetic trap were stabilized by means of a series of dispersive Faraday imaging. The feedback between the images is used to send radio-frequency pulses that expel atoms from the trap in a controlled way. In this thesis, a dedicated fluorescence imaging system is used to prepare on-demand atom numbers in a magneto-optical trap by employing a controlled feedback loss mechanism.

The scope of this thesis is structured as follows. The second chapter presents the design of the experimental apparatus and describes its individual components necessary for a fast BEC production. The setup is motivated by giving an outline of the envisioned experimental measurements in view of atom interferometry with entangled particles. Chapter 3 describes the procedure for the BEC generation with high repetition rates and presents the optimized experimental parameters. In particular, the two main features of a high-flux atom source and the two-step hybrid evaporation scheme are presented. In Chapter 4, the featured results of the first-generation detection system for accurate preparation and detection are covered. The single-particle detection enabled a number-stabilized preparation of 7 atoms. This setup is replaced by a new, second-generation optical fiber-based detection setup that provides an even better performance with respect to spatial and temporal stability, which is presented in Chapter 5. Finally, Chapter 6 summarizes the results of this thesis and provides an outlook to potential optimization steps in view of aspired applications.

CHAPTER 2

Experimental Apparatus

The following chapter describes the details of the experimental apparatus that has been designed and developed as part of this thesis. It is a new dedicated setup, which will make it possible to conduct quantum-enhanced interferometry experiments with ultracold atomic ensembles. The experimental procedure for this ambitious task poses challenging requirements on the capabilities of the underlying apparatus, which have direct implications for the properties of the individual components.

The first section of this chapter sketches the plan for the experimental sequence and phrases the substantial requirements for the envisioned performance. The following sections describe the physical properties of the components that are key for accomplishing the imposed tasks[1]. Starting with the second section, the vacuum system is presented as the main platform of the experiment that provides the essential environment for the preparation and investigation of ultracold atomic ensembles. Sections three and four explain the coil and laser systems, which provide the required magnetic as well as light fields used for the cooling, trapping and manipulation of atoms. Section five describes the microwave setup that will be used for internal state manipulations. Section six is devoted to the imaging systems that allow for evaluation of measurement results, such as temperature and density measurements of thermal atomic clouds or the detection of atom numbers with single-particle resolution. Finally, the last section lays out the architecture for the control of the experimental apparatus.

2.1 Overview of the experimental procedure

The design goals of the experimental apparatus are targeted at performing high-precision and high-sensitivity interferometric measurements with ultracold ensembles of entangled ^{87}Rb atoms, which will be created in a Spinor-BEC using spin-changing collisions. They can be defined by means of a corresponding experimental scheme, which is outlined in Fig. 2.1. The experimental sequence of a quantum-enhanced atom interferometer can generally be divided into three main stages: the preparation of a BEC, the execution of

---

[1] A more detailed description of the physical qualifications and specifications of the experimental parts has been elaborated in the PhD thesis [88].

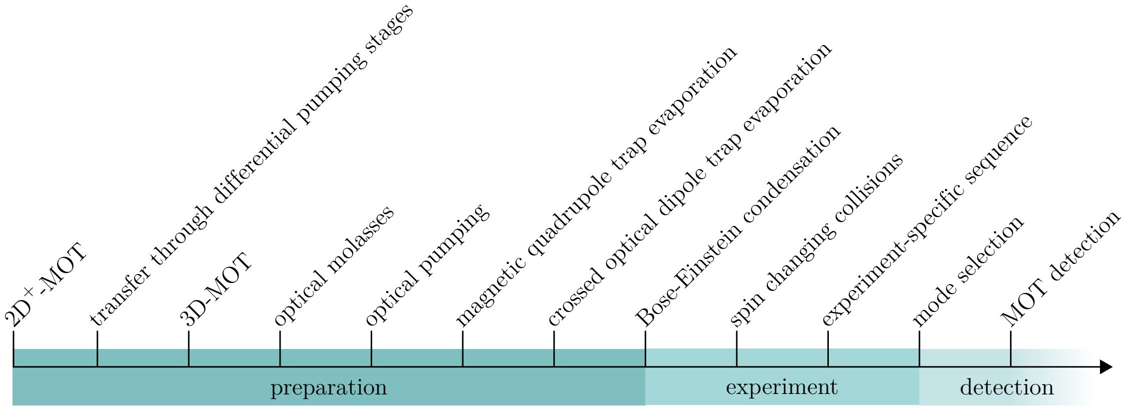
2D+-MOT
transfer through differential pumping stages
3D-MOT
optical molasses
optical pumping
magnetic quadrupole trap evaporation
crossed optical dipole trap evaporation
Bose-Einstein condensation
spin changing collisions
experiment-specific sequence
mode selection
MOT detection
preparation
experiment
detection

Figure 2.1: Experimental concept. The timeline depicts the different steps to be followed in the experimental sequence, which is divided into three main stages. The preparation starts with a 2D$^+$-MOT that generates a pre-cooled beam of atoms, loaded from a background gas, and guides them through differential pumping stages into a 3D-MOT inside the ultrahigh vacuum science chamber. An optical molasses phase is applied to cool the atoms below the Doppler limit. After laser cooling, atoms are optically pumped into a magnetically sensitive state in order to efficiently load into a quadrupole trap, in which a forced radio-frequency evaporation step is employed. The evaporative cooling is completed in a strongly focused crossed optical dipole trap by lowering the optical power until a Bose-Einstein condensate is created. The basis for conducting future experiments is the generation of entanglement amongst the condensed atoms by preparing the initial spin state and employing spin changing collisions. A state-selective fluorescence detection is accomplished by spatial separation of the different magnetic spin components, which are illuminated by the MOT beams of the detection system.

the interferometric experiment and the detection of the outcome in terms of atom numbers. The following subsections will summarize the planned experimental procedure, after which the underlying hardware is presented.

2.1.1 Preparation

The preparation time of large ultracold atomic ensembles is crucial for a state-of-the-art atom interferometer. A high sample rate allows for short averaging times, increased temporal resolution and a smaller susceptibility to long-term drifts. However, the cycle time of a BEC apparatus can depend on many properties of its individual components. There are two main steps that can slow down the production time most significantly. The initial loading of atoms into a three-dimensional magneto-optical trap can take several seconds, if loaded from a low-flux source or directly from a background gas. Even more drastically, the evaporative cooling processes can suffer from shallow trap configurations, which inherently slow down the evaporation dynamics. These challenges are addressed by the dedicated setup and are discussed in Chapter 3.

The preparation stage begins with the trapping of ^{87}Rb atoms inside a large-volume three-dimensional magneto-optical trap (3D-MOT), which is loaded from an enhanced two-dimensional magneto-optical trap (2D$^+$-MOT) [89–91]. This loading scheme employs a pushing beam that is pointed along the longitudinal direction towards the center of the 3D-MOT and generates a high-flux stream of pre-cooled atoms. While being trapped, the rubidium atoms are laser-cooled to the Doppler temperature limit by the six circularly polarized MOT beams driving the cooling $\left|5^2S_{1/2},F=2\right\rangle \rightarrow \left|5^2P_{3/2},F'=3\right\rangle$ and repumping $\left|5^2S_{1/2},F=1\right\rangle \rightarrow \left|5^2P_{3/2},F'=2\right\rangle$ transitions.[1] Further cooling down the atomic cloud to few tens of microkelvin is achieved by using polarization gradient cooling, for which the magnetic field gradient is turned off, the magnetic offset fields are cancelled and a short, far red detuned optical molasses pulse is applied. After the laser cooling stages, the atoms are transferred into a large-volume magnetic quadrupole trap (QPT) by ramping up the magnetic field gradient for subsequent evaporative cooling. In order to efficiently load the atoms into the QPT, an optical pumping beam with σ^+-polarization, which is driving the $|F=2\rangle \rightarrow |F'=2\rangle$ transition, in conjunction with a small homogeneous magnetic field is applied to transfer the unpolarized atoms into the magnetically trappable hyperfine state $|F=2,m_F=2\rangle$. Forced evaporative cooling in the QPT is realized by ramping down a continuous radio frequency (RF) field that drives transitions in the $|F=2\rangle$ manifold. The RF ramps are rather fast and not used to evaporate all the way to quantum degeneracy. Instead, the RF evaporation is used to increase the initial phase space density (PSD) of the atomic cloud for a better mode-match and transfer into the steep crossed-beam optical dipole trap (cODT) potential, where the final evaporation stage takes place. After loading the atoms into the cODT, the last evaporation step is realized by ramping down the optical power of the corresponding dipole laser beams until a Bose-Einstein condensate is created.

2.1.2 Experiment

The basis of the experiment stage is set by the preparation of a BEC in the $|F=2,m_F=2\rangle$ hyperfine spin state. In order to drive spin changing collisions, the atoms will be prepared in the $|F=1,m_F=0\rangle$ Zeeman state by employing a sequence of three resonant microwave π-pulses $|F=2,m_F=2\rangle \rightarrow |F=1,m_F=1\rangle \rightarrow |F=2,m_F=0\rangle \rightarrow |F=1,m_F=0\rangle$.[2] Residual populations in the $|F=2,m_F\rangle$ manifold can be removed by using interleaved resonant light pulses with respect to the $|F=2,m_F\rangle \rightarrow |F'=3,m_F\rangle$ transition. After the initial spin state preparation, a microwave dressing field with respect to the $|F=1,m_F=-1\rangle \rightarrow |F=2,m_F=-2\rangle$ transition will be applied that shifts the $|F=1,m_F=-1\rangle$ state and thereby equalizes the asymmetric splitting of the $|F=1,m_F=\pm 1\rangle$ sublevels. This allows spin changing collisions to take place and generate entangled states, which will be used as a starting point for subsequent experimental measurements.

---

[1] In the following the fine structure terms will be omitted, where F,F' will refer to $5^2S_{1/2}$,$5^2P_{3/2}$ and represented by the Dirac notation $|F,m_F\rangle$, respectively.

[2] Principally, spin changing collisions can also be realized in the $|F=2,m_F\rangle$ hyperfine manifold, but with the disadvantage of a significant two-body mechanism caused by hyperfine-changing collisions.

2.1.3 Detection

For a high-performance experiment, precision and accuracy of the detection system is as important as the fast preparation of the atomic samples. In a state-of-the-art atom interferometer measurement, the output signal is derived from the detection of the final number of atoms in the corresponding output ports at the end of the experimental sequence. An inaccurate counting of atoms is typically imprinted by technical imperfections that are limiting the resolution of the underlying detection system, which in turn leads to an increased instability. The ultimate accuracy can be accomplished by a detection system that provides single-atom resolution. This can be accomplished by using a fluorescence detection scheme, in which atoms are recaptured in a dedicated small three-dimensional detection MOT (d-MOT). Long interrogation times provide a large signal-to-noise-ratio, given that the atomic lifetime is much larger than the detection time. The fluorescence signal of the atoms is collected by a large-numerical-aperture objective lens and imaged onto a high-quantum-efficiency charge-coupled device (CCD) camera. The atom number is then estimated by dividing the total signal count by the expected count level of a single atom. Ultimately, the resolution at the single-atom level is witnessed by a discretization of the output of multiple integers of the single atom signal. The scattering rate of the fluorescence light of the atoms is very sensitive to changes in the laser frequency and intensity, which makes an active stabilization of both a necessity. In addition, the pointing stability of the six MOT beams are challenging the stability of the single-atom resolution.

2.2 Vacuum system

The vacuum system is the basic structure of the experimental apparatus, which provides a suitable environment for conducting experiments with ultracold ensembles of ^{87}Rb atoms (Fig. 2.2). In particular, the vacuum conditions for the two main tasks of preparing and investigating the atoms are subject to mutually exclusive requirements that must be met simultaneously. An efficient preparation of large numbers of atoms requires a sufficient background gas pressure, whereas a reliable investigation calls for an ultra-high vacuum (UHV) condition, in the expectation of minimizing collisions with the thermal background gas. Hence, a good vacuum quality ultimately results in an increased lifetime of the atoms and therefore longer lasting interrogation times. In order to bring the two seemingly contradictive requirements into agreement, the vacuum system assembly encompasses a two-chamber setup, where the corresponding tasks are taken over separately. The atoms are initially prepared in the rectangular 2D$^+$-MOT chamber and then transferred to the octagon-shaped science cell for further investigation.

A custom-made four-way cross connects both chambers together, along with all the other vacuum components that are used to maintain and monitor the pressure (Fig. 2.3). Two successive differential pumping stages divide the vacuum into three regions and allow the necessary pressure gradient to be maintained between the two glass chambers. The first high-pressure section inside the 2D$^+$-MOT chamber is established by means of one of three dispensers generating a background gas of rubidium atoms. The 2D$^+$-MOT is

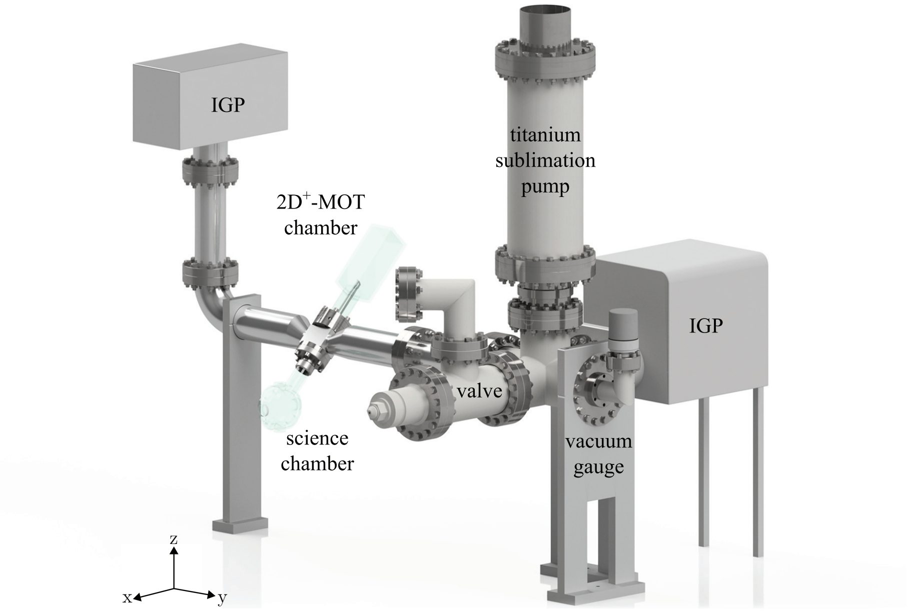

Figure 2.2: Ultrahigh vacuum system assembly. The vacuum system is constructed by a framework of custom made aluminum and stainless steel tubes interconnected with different sized ConFlat (CF) flanges and sealed with copper gaskets. The evacuated structure represents a closed system, where the initial vacuum of 10^{-8} mbar was generated by connecting a turbomolecular pump to the valve. Two IGPs are active to attain and sustain a UHV pressure below 10^{-11} mbar. In case of residual leakage, an additional titanium sublimation pump can be used. A vacuum gauge monitors the pressure contained in the science chamber. The $2D^+$-MOT and science chambers represent the two main environments for the atoms and are manufactured from quartz glass with anti-reflection coatings for 780 nm. Adapted from Ref. [88].

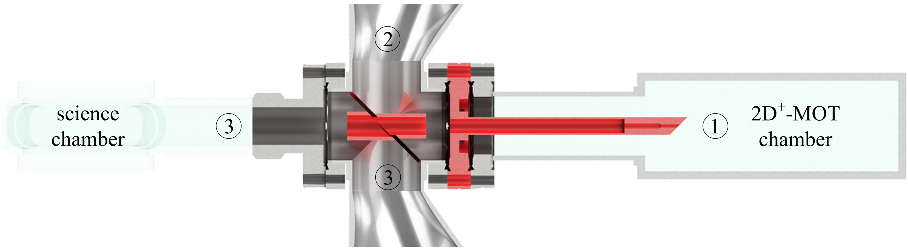

Figure 2.3: Two-chamber setup. The $2D^+$-MOT chamber and the science chamber are connected by a four-way cross and share a common line of sight. The vacuum is divided into three distinct regions by two successive differential pumping stages, indicated by circled numbers. The first pumping stage is 100 mm long and has a 2 mm diameter entrance port that expands to an 8 mm inner diameter at a distance of 25 mm. The second pumping stage is located right behind the first one and is embedded in a diagonal wall that separates the vacuum within the four-way cross. Adapted from Ref. [88].

connected to the rest of the vacuum via the first differential pumping stage, which ensures that the high background pressure is retained. The second differential pumping stage divides the vacuum into two more sections, which can be pumped separately by two ion getter pumps (IGPs) (VacIon Plus 150 Star Cell Model 919 - 0104, Varian Large Star cell Model 929 - 0172). The IGPs shield the ultra-high vacuum in the science chamber and maintain a pressure of less than 10^{-11} mbar. In the case of residual leakage of the vacuum or contamination with different atoms, a titanium sublimation pump (TSP) can be fired to bind the undesired background atoms to the respective titanium-coated wall surfaces. A vacuum gauge measures the pressure inside the science chamber. Apart from the $2D^+$-MOT chamber, the pressure in the remaining regions can also be estimated from the current flowing through the IGPs. With this arrangement, a pressure gradient of at least two orders of magnitude between the two chambers can be achieved.

2.3 Coil System

In the experimental procedure, a number of different magnetic fields are necessary for atomic ensembles to be trapped, cooled and manipulated. Most neutral atoms exhibit an internal magnetic moment that can interact with external magnetic fields. The needed magnetic fields are provided by a set of bulk coil configurations that are mainly composed of copper wire windings. The specified magnetic field strengths and gradients at the position of the atoms are in principle defined by the distances, winding densities and the current flow through the coils. In order to generate sufficient magnetic field strengths and gradients, it is therefore beneficial to position the coils as close as possible to the atoms. However, a trade off must be found between high optical access to the science glass chamber and low power consumption for the corresponding coil configurations to prevent unwanted heat sources. In the following section, the design of the different coil structures along with the involved magnetic fields is discussed with the main objective of maximizing the optical access to the science chamber, as it is of upmost importance for the conduction of interferometric sequences in conjunction with the utilization of the single-particle detection system (see Section 2.6).
The coil system is composed of a standalone $2D^+$-MOT coil setup (Fig. 2.4) and a composite assembly that encompasses the science chamber (Fig. 2.5).

The $2D^+$-MOT coils in conjunction with the $2D^+$-MOT beams are used to prepare a pre-cooled beam of rubidium atoms inside the $2D^+$-MOT glass cell, which can be transferred via a push beam to the science chamber. A set of four coils with 81 windings are wound on a cuboid aluminum frame, which encloses the $2D^+$-MOT glass chamber. The coils generate a two-dimensional magnetic quadrupole field with a normalized gradient of 3.3 G/A cm. The current of each coil can be tuned independently, which allows to shift the center of the magnetic trap, such that the atoms can pass through the differential pumping stages. For the operation of the $2D^+$-MOT the coil currents are set to a mean value of 4.5 A, which corresponds to a gradient of 14.5 G/cm. The $2D^+$-MOT setup is elevated by 45° to allow optical access to the science chamber in the horizontal plane.

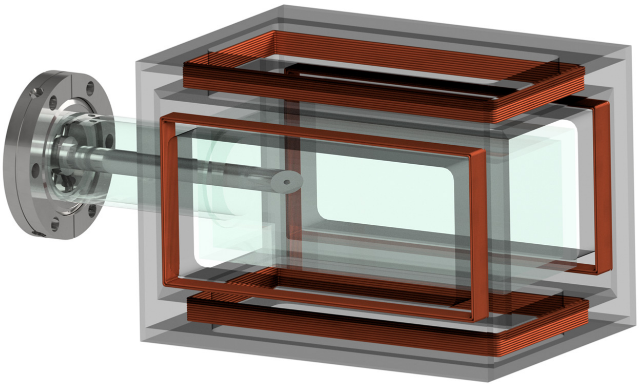

Figure 2.4: 2D$^+$-MOT coil setup. A set of four rectangular coils are arranged around the transversal surfaces of the 2D$^+$-MOT chamber. The coils produce a magnetic quadrupole field with the minimum aligned along the longitudinal direction to the entrance of the differential pumping stage.

The science chamber is surrounded by a coil system assembly that satisfies the optical constraints posed by the laser fields and detection systems (see Sections 2.4 and 2.6). The 3D-MOT coils are located symmetrically on top and bottom of the science chamber at a distance of 93.75 mm to its center. They consist of 20 windings wrapped around copper mounts and have an inner radius of 18.4 mm. The normalized magnetic field gradient is 0.118 G/A cm and the maximum field gradient of 44 G/cm is determined by the total coil wire resistance of 0.04 Ω. The 3D-MOT coils provide the quadrupole field, which is used for the cooling and trapping of atoms. The coils are run by two power supplies (Gen-7.5-1000, TDK Lambda) that are connected in series and can deliver currents and voltages of up to 1000 A and 15 V, respectively.

The QPT coils are aligned inbetween the MOT coils along the circumference of the 3 inch viewports of the science cell with their principal axes pointing along the y-direction. The coils with a total winding number of 72 are separated by a distance of 48.75 mm and have an inner radius of 48.4 mm. The anti-Helmholtz configuration of the QPT coils provides a three-dimensional quadrupole field for the magnetic trapping and cooling of the atoms. The conical wedges along the inner circumferences provide larger optical access and enable to bring the main detection objective closer to the 3 inch viewport of the science chamber, while the 3D-MOT beams have an angle of incidence of 45° with respect to the glass cell surface. A uniform field gradient of 1.790 G/A cm together with a total wire resistance of 0.18 Ω yields a maximum field gradient of 597 G/cm. The coils are connected to a power supply (Gen-60-250, TDK Lambda) that can provide 250 A and 60 V.

A pair of Helmholtz coils with the principle axis aligned in the x-direction is attached to the copper mounts of the 3D-MOT coils. With 12 turns each, a small magnetic field of about 3 G can be generated by currents of up to 5 A. The Helmholtz coils provide a homogeneous magnetic field that sets the quantization axis for the magnetic moments of the atoms and splits the corresponding Zeeman levels. A counter-propagating beam with

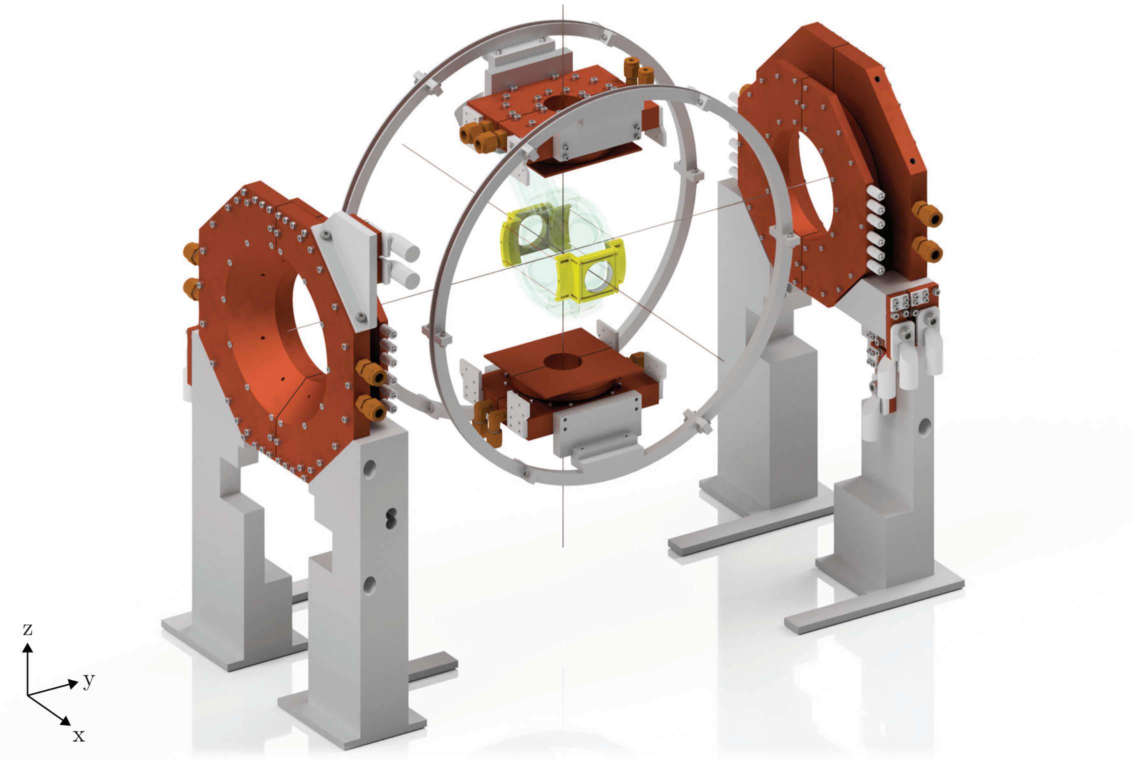

Figure 2.5: Coil system assembly. The CAD drawing shows the set of four coils for the cooling, trapping and manipulation of the atoms. The quadrupole coils, with the principle axis along the y-direction are pulled out from the assembly in order to expose the science chamber and the RF coils for a better visibility. The RF coils are mounted on 3D-printed coil mounts wrapped and spanned around the two 1 inch viewports of the science chamber. The positions of the 3D-MOT coils and homogeneous field coils is unaltered. Eddy currents are prevented by splitting the coil mounts in two halfs with an insulating layer inbetween. Because of the high power consumption, solely the mounting frames for the 3D-MOT and QPT coils have water in- and outlets in order to carry away the dissipated heat.

respect to the homogeneous magnetic field direction and its frequency detuned with respect to the $|F = 2\rangle \rightarrow |F' = 2\rangle$ transition is used in order to optically pump the atoms to the magnetically most sensitive state $|F = 2, m_F = 2\rangle$ and prepare them for magnetic trapping in the QPT.

The RF coils are formed by two 0.5 mm thin copper wires, which are spanned and wrapped around two 3D-printed coil mounts attached to the 1 inch viewports on the front and back side of the science chamber. A Direct Digital Synthesis (DDS) device in conjunction with a 15 W, 10 kHz – 250 MHz power amplifier (15A250, Amplifier Research) is used to generate radio frequencies in the range of about 3 – 30 MHz for evaporative cooling in the quadrupole trap.

In addition, a Stern-Gerlach coil with 0.8 mm wire thickness and 44 windings is placed in front of the 1 inch viewport of the science chamber. The Stern-Gerlach coil at a distance of 50 mm to the center of the science chamber produces a magnetic field gradient that allows to spatially split the different spin components within a BEC along the horizontal x-direction. For the different components to be visible, the separation needs to be on the order of a few 100 μm. This requires a peak current of ~600 A, which is generated by the discharge of a large capacitor (EPCOS 100V, 0.047F). The discharge is switched via an insulated-gate bipolar transistor (IGBT) transistor that is controlled by an opto-coupler-MOSFET driver (FOD3182).

2.4 Laser System

The following section describes the optical setup of the two laser systems used in the experiment for the cooling, trapping and manipulation of ^{87}Rb atoms. The first laser system provides the frequencies necessary for the operation of the 2D$^+$- and 3D-MOT, the molasses cooling, the optical pumping and the detection. It consists of two interference-filter-stabilized external cavity diode lasers (ECDLs) [92], which are controlled by home-built current drivers and Proportional-Integral-Derivative (PID) controllers. The second laser system provides the light to create the optical dipole trap. It is a commercial Nd:YAG laser with table-top master laser and amplifier controllers.

2.4.1 Laser system for laser cooling

The ECDL system provides all frequencies that are necessary to drive hyperfine transitions from the ground state $\left|5^2S_{1/2}\right\rangle$ to the excited state $\left|5^2P_{3/2}\right\rangle$ of the rubidium D2-line, which has a natural linewidth of $2\pi \times 6.067\,\mathrm{MHz}$ (Fig. 2.6). For this reason, two narrow spectral linewidth ECDLs are used, which incorporate a built-in interference filter for the coarse selection of the central wavelength of 780.24 nm. The first laser is frequency-locked and actively stabilized via modulation transfer spectroscopy with respect to the $|F = 2\rangle \rightarrow |F' = 3\rangle$ closed hyperfine transition [93]. The spectroscopy setup introduces a 200 MHz frequency offset that leaves the frequency inbetween the |F'=2⟩ and |F'=3⟩ hyperfine states. From this point all other transitions can be addressed by shifting the laser frequency with acousto-optic modulator (AOM). In order to reach the cooling transition, two successive 200 MHz AOMs in single- and double-pass configuration are used, where the former shifts the frequency to the red by the negative first order and the latter shifts to the blue by twice the positive first order. The double-pass AOM takes a special role, since it allows to change the frequency detuning and power for the cooling light by adjusting the modulation and power of the AOM radio frequency. The frequency for resonance fluorescence detection corresponds to the cooling light with zero detuning. However, the number-resolved detection of the atoms involves a frequency detuning, which can be changed by the cooling AOM. The optical pumping frequency is driving the $|F = 2\rangle \rightarrow |F' = 2\rangle$ transition and derived by adding a 80 MHz AOM in double-pass configuration. The second ECDL provides the repumping light for the operation of the two magneto-optical traps. Due to the close separation between excited hyperfine levels, there is a non-zero probability for the cooling light to excite atoms to the $|F' = 2\rangle$ state, from which they can decay back

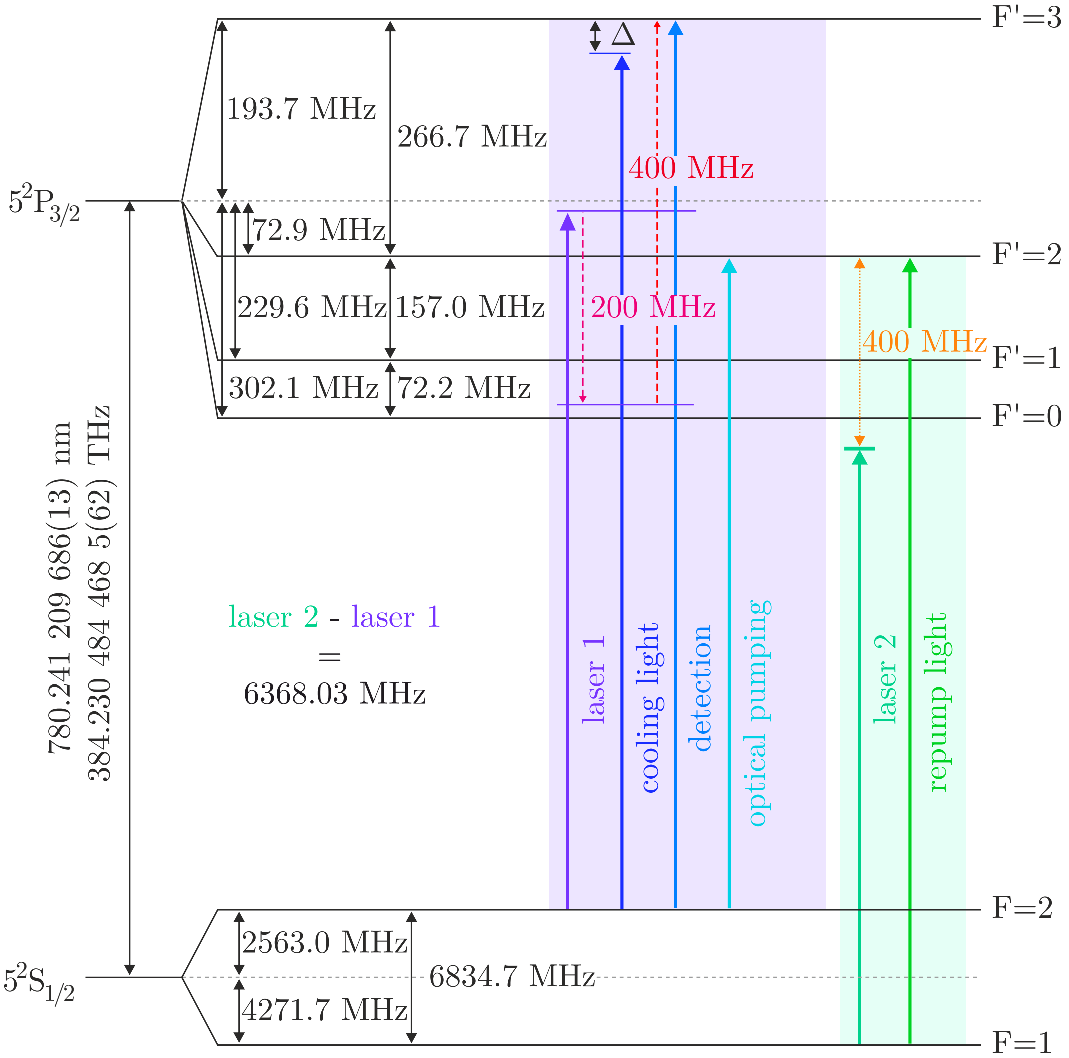
F'=3
F'=2
F'=1
F'=0
F=2
F=1
5²P3/2
5²S1/2
193.7 MHz
266.7 MHz
72.9 MHz
229.6 MHz
157.0 MHz
302.1 MHz
72.2 MHz
Δ
400 MHz
200 MHz
400 MHz
2563.0 MHz
4271.7 MHz
6834.7 MHz
780.241 209 686(13) nm
384.230 484 468 5(62) THz
laser 2 - laser 1
=
6368.03 MHz
laser 1
cooling light
detection
optical pumping
laser 2
repump light

Figure 2.6: Energy level diagram of the ^{87}Rb D$_2$ line transition. The energy levels are split up by the hyperfine interaction. The cooling light transitions are depicted in shades of blue and the repumping laser in green. The corresponding shifting AOM frequencies are represented by dashed arrows. Adapted from Ref. [88] and extended.

into the $|F = 1\rangle$ ground state. The large separation of 6.8347 GHz between the ground states makes it difficult to address these atoms with a single cooling laser only. Therefore, the repumping laser is locked with respect to the hyperfine transition $|F = 1\rangle \rightarrow |F' = 2\rangle$ by beating it with the first laser and feeding the signal into a microwave interferometer with an adjustable delay stage [94]. The beating frequency is stabilized to 6.368 GHz above the frequency of the first laser. An additional 200 MHz AOM in double-pass configuration allows to set the detuning for the repumping light. Both ECDLs have typical output powers of 30 – 40 mW, which is not sufficient for the MOT operations. For this reason, the ECDL output powers are injected into four tapered amplifiers (TAs), which are used to generate the sufficient laser power. The optical setup of the ECDL system is spread across a dedicated optical table, where the required frequencies and powers for the different applications are generated (Fig. 2.7). The derived light fields are distributed to the optical setups on the vacuum system table via polarization-maintaining single-mode fibres, after which free-space optics provide beam shaping, polarizing and splitting. Table 2.1 summarizes the total optical powers for each light source and the corresponding AOM frequencies. The optical setups on the vacuum table are described in Sections 3.1.3, 3.2.5 and 5.1.

Table 2.1: ECDL system parameters

light source	AOM frequency (MHz)	optical power (mW)
$2D^+$-MOT cooling	188.5	431
$2D^+$-MOT repump	199.5	10.5 (TA seed)
3D-MOT cooling	187.6	152
3D-MOT repump	199.5	12.8
optical molasses	168	106.4
optical pumping	73	0.46

2.4.2 Laser system for optical dipole trapping

A high-stability continuous-wave (CW) Mephisto Mopa (Coherent) laser system provides the light at 1064 nm and a total power of 55 W used for the crossed optical dipole trap. The laser head contains a master laser with a monolithic Nd:YAG crystal and four amplifier stages, which are pumped by corresponding temperature-stabilized pump diodes. The laser crystal itself is additionally temperature stabilized to further improve the frequency stability. The output power is tuned by the master laser and amplifier drivers that provide a low noise injection current for the laser diodes of up to 3 A and 60 A, respectively. A built-in intensity stabilization of the master laser can be used to suppress the amplitude noise close to the shot noise and thus to minimize potential heating rates of the cold atoms.

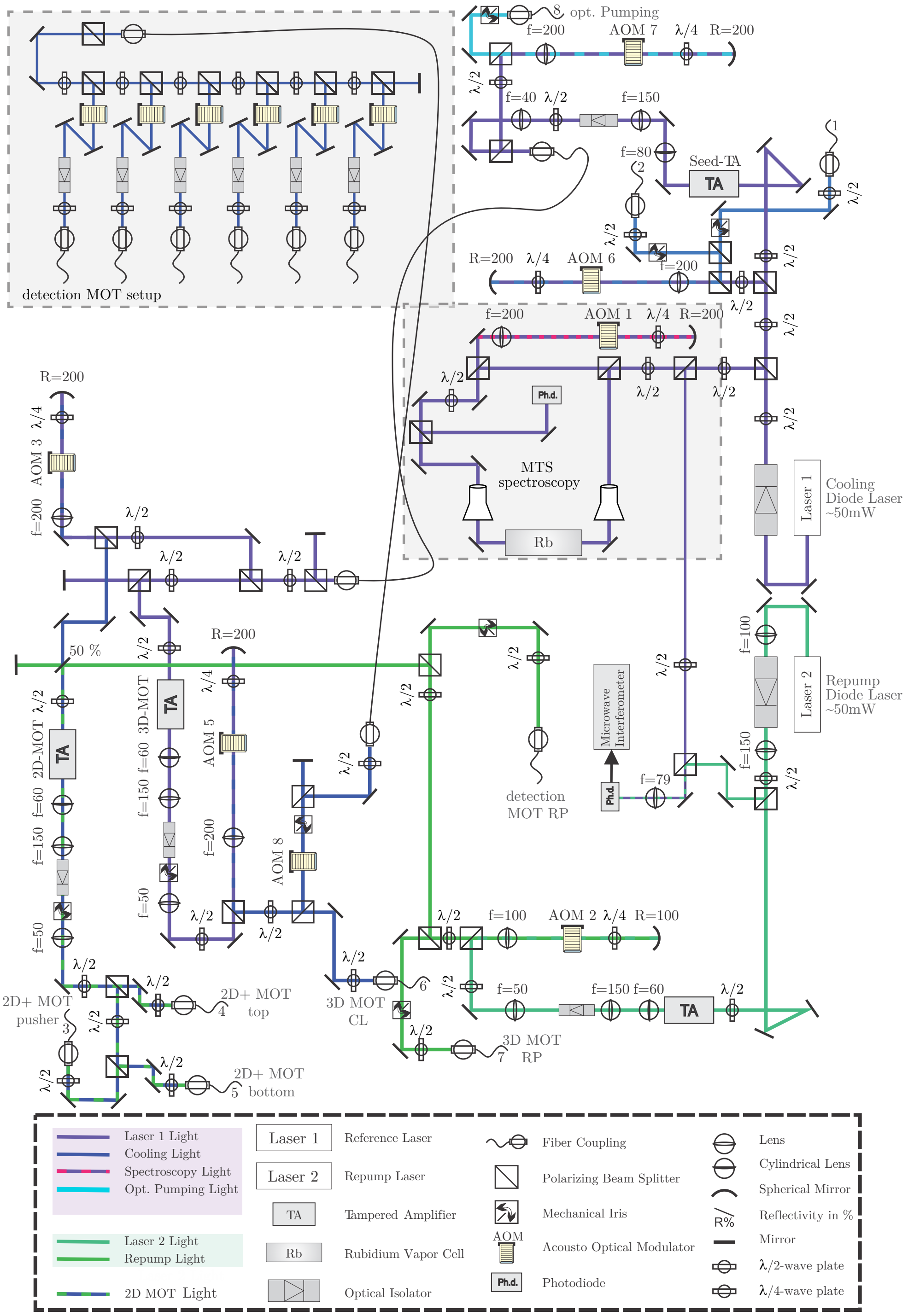
8
opt. Pumping
f=200
AOM 7
λ/4
R=200
λ/2
f=40
λ/2
f=150
f=80
2
Seed-TA
TA
1
λ/2
λ/2
R=200
λ/4
AOM 6
f=200
λ/2
detection MOT setup
f=200
AOM 1
λ/4
R=200
λ/2
λ/2
λ/2
λ/2
λ/2
Ph.d.
MTS
spectroscopy
Rb
Laser 1
Cooling
Diode Laser
~50mW
R=200
λ/4
AOM 3
f=200
λ/2
λ/2
λ/2
50 %
R=200
λ/2
2D-MOT
TA
f=60
f=150
f=50
λ/2
3D-MOT
TA
f=60
f=150
f=50
λ/4
AOM 5
f=200
AOM 8
λ/2
λ/2
λ/2
λ/2
λ/2
λ/2
detection
MOT RP
Microwave
Interferometer
Ph.d.
f=79
λ/2
f=100
Laser 2
Repump
Diode Laser
~50mW
f=150
λ/2
λ/2
λ/2
f=100
AOM 2
λ/4
R=100
λ/2
f=50
f=150
f=60
TA
λ/2
6
3D MOT
CL
λ/2
3D MOT
7
RP
λ/2
λ/2
2D+ MOT
4
top
2D+ MOT
pusher
3
λ/2
λ/2
λ/2
2D+ MOT
5
bottom
Laser 1 Light
Cooling Light
Spectroscopy Light
Opt. Pumping Light
Laser 2 Light
Repump Light
2D MOT Light
Laser 1
Reference Laser
Laser 2
Repump Laser
TA
Tampered Amplifier
Rb
Rubidium Vapor Cell
Optical Isolator
Fiber Coupling
Polarizing Beam Splitter
Mechanical Iris
AOM
Acousto Optical Modulator
Ph.d.
Photodiode
Lens
Cylindrical Lens
Spherical Mirror
R%
Reflectivity in %
Mirror
λ/2-wave plate
λ/4-wave plate

Figure 2.7: Layout of the ECDL system. The scheme shows the optical setup that generates the laser powers and frequencies shown in Fig. 2.6. The corresponding light fields are distributed via fiber couplers to the vacuum table. The new detection MOT setup is elaborated in Section 5.1. This setup is an updated version of the diagram shown in Ref. [88].

2.5 Microwave setup

A microwave source is essential for a coherent control of the internal hyperfine structure of ultracold atomic ensembles. Especially, for the anticipated experimental tasks, such as state preparation, manipulation as well as detection, continuous and pulsed microwave fields will be utilized. In the context of atom interferometry, the operation of the microwave source requires extraordinary precise control. Microwave pulses are used to drive transitions between different atomic hyperfine states and act as beam splitters or mirrors. The fidelity of the microwave pulses can be affected by amplitude or phase noise, which will be directly imprinted as fluctuations on the measured interferometer phase. Therefore, technical imperfections, such as fluctuations in the microwave power or frequency need to be kept at a minimum. The microwave source is also required to provide dynamical and fast changes in its parameters, such as amplitude, phase and frequency. In particular, the employed microwave transitions will require a succession of pulses with variable frequencies and short pulse durations. This is important to suppress decoherence, as shorter pulses are less sensitive to small changes of the frequency detuning, due to a broader distribution in the frequency domain. In addition, the shape of the microwave pulses will be crucial for high transfer efficiencies, since simple rectangular box pulses can generate several side peaks in the Fourier space, which can contribute to the population of neighboring hyperfine levels. Tailored microwave pulses with short pulse durations will require amplitude modulation and a sufficient microwave power. Therefore, a dedicated versatile microwave setup is used, which is illustrated in Fig. 2.8. The design of this setup was developed in the framework of a Master's thesis [96], which covers the subject in greater detail. Here, the main properties and components of the microwave setup are outlined.

The microwave setup is designed to drive transitions and provide off-resonant dressing fields between the two hyperfine manifolds $|F=1\rangle$ and $|F=2\rangle$ of the ^{87}Rb D$_2$ line in the frequency range of 6.835 GHz ± 5 MHz. The microwave frequencies are derived from two commercially available frequency synthesizers. An ultra-low-phase-noise local oscillator (LO) (Wenzel MXO-PLD) generates a stable output frequency at 7 GHz close to the hyperfine transition frequency. A DDS (Urukul) provides four independently controllable radio-frequency output channels with adjustable frequencies up to 460 MHz.[1] Two output channels of the DDS are used to provide the frequencies for the pulse and dressing path, respectively. The center frequencies of both output channels are set to 165 MHz and mixed with the LO frequency. The two mixers (Mini Circuits ZMX-8GLH) produce lower and higher sidebands, of which the lower is the desired transition frequency $f_{Rb} = f_{LO} - f_{DDS}$. Narrow bandpass filters (Wainwright WBCQV3) with a passband of 20 MHz and 50 dB attenuation enable the selection of the lower sideband and simultaneously the reduction of the carrier and higher sideband frequencies. Due to insertion losses after the mixing,

---

[1] The DDS module is embedded in the Advanced Real-Time Infrastructure for Quantum physics (ARTIQ) and controlled by an field-programmable gate array (FPGA) (Kasli), which enables dynamic parameter changes with maximal timing resolution. A digital I/O module offers the triggered execution and control of microwave switches via TTL logic signals.

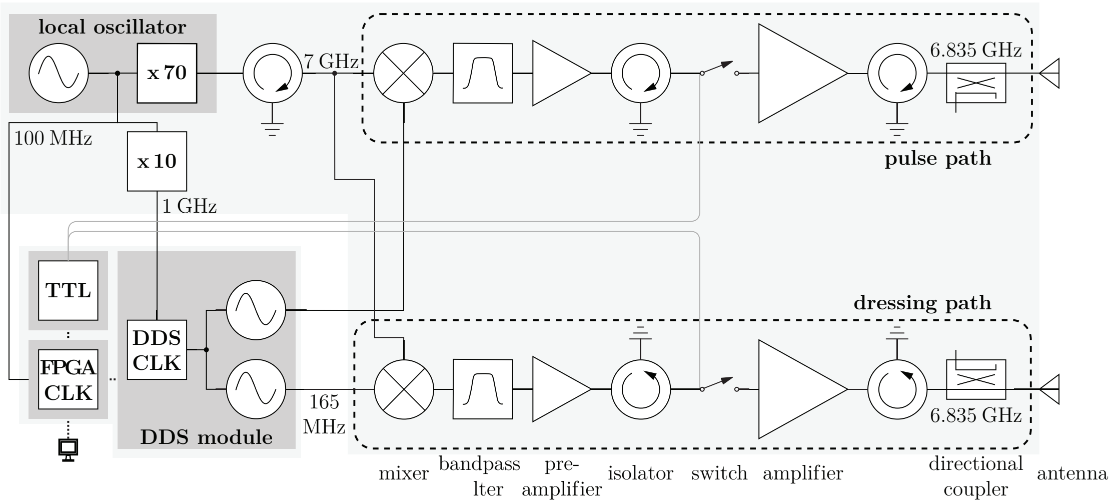

Figure 2.8: Schematic diagram of the microwave setup. The direct digital synthesizer (DDS) generates two independently controllable radio-frequency signals with a center frequency of 165 MHz. Both signals are mixed with the 7 GHz output frequency of the ultra-low-phase-noise local oscillator, which is protected by an isolator against back reflections. The two microwave signals are split into two paths that consist of a narrow bandpass filter and a pre-amplifier that generates the optimal input power for the final amplifier stage. In addition, isolators protect the amplifiers from potential back reflections from the switch and the antenna. A directional coupler allows for monitoring of a small reflected fraction of the output signal. Both paths use the same schematics, however the pulse path has a stronger power amplifier than the dressing path. For a stable phase relation of the mixed radio- and microwave frequency sources, the 100 MHz output of the local oscillator is split into two paths, while one of them is multiplied by 10. These signals act as a reference for the FPGA and DDS clocks, respectively. The components in the light gray shaded box are mounted on a water-cooled aluminum plate. Adapted from Ref. [95].

low-noise pre-amplifier stages are used to raise the power level to the desired input level of 0 dBm for the high-power amplifiers. In order to completely switch off the microwave power of both paths, additional power switches (Mini Circuits ZFSWA2-63DR+) with 40 dB attenuation are employed. The pulse and the dressing path are equipped with high power amplifiers with 40 W (Microwave Amps AM43) and 10 W (Kuhne KU PA 640720-10 A), respectively. Directional couplers (RF Lambda RFDDC2G8G30 and MCLI C39-20) in the pulse and dressing paths before the emitting antennas, as well as isolators in front of the switches protect the amplifiers from potential back reflections. The directional couplers additionally offer the possibility to monitor the final output powers. Both microwave frequencies are referenced with respect to the 100 MHz frequency of the LO, in order to provide a stable phase relation. The amplitude and frequency noise of this setup was characterized in Ref. [95].

2.6 Detection system

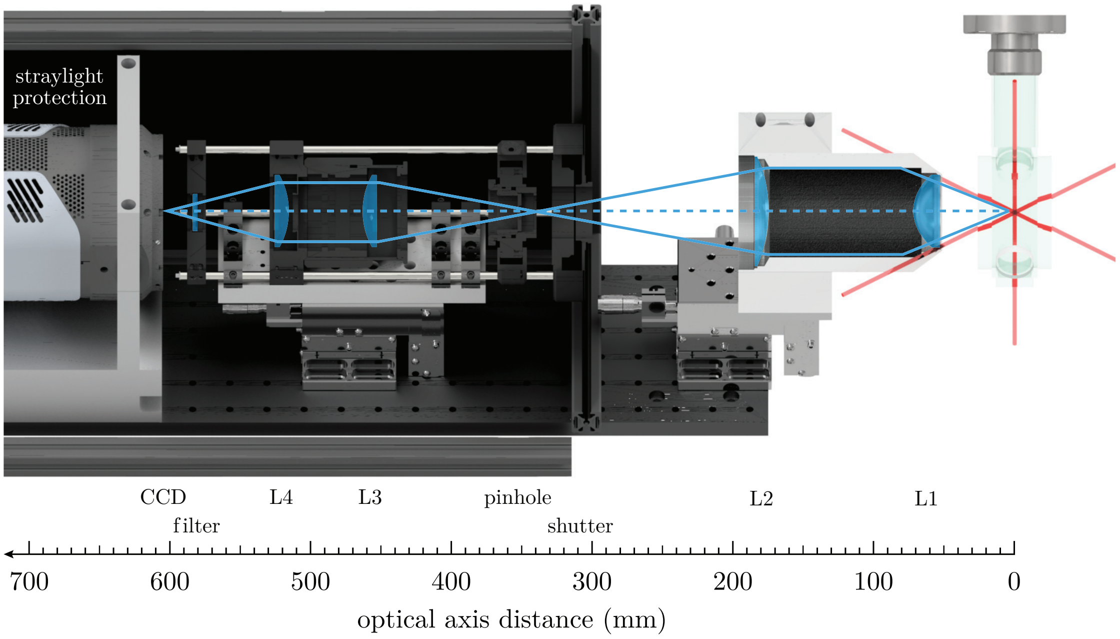

Figure 2.9: Detection system. Assembly of the optical components for the number-resolved detection of single atoms. A half-section view of the optical components reveal the lens (light blue), pinhole and shutter positions. Apart from the first objective lens, the remaining optics are encapsulated inside an anodized straylight protection box. The side and top covers are removed for illustration purposes.

Throughout the experiments, a fluorescence imaging scheme is used to measure the number of atoms. In particular, the experimental apparatus is dedicated to distinguish the fluorescence signal of individual atoms, which corresponds to optical powers less than 10^{-12} W. In order to measure such low levels of light power, a main detection setup that is composed of a low-noise, high-quantum-efficieny $QE = 98\%$ CCD camera chip (Princeton Instruments, 1024 BR eXcelon) and a large-numerical-aperture (NA ≈ 0.4) objective lens is used (Fig. 2.9). The objective lens is placed closely (≈ 50 mm) to the atomic cloud position in front of the 3 inch viewport of the science chamber. It consists of two lenses inside a cylindrical aluminum housing, mounted on a three-dimensional translation stage, which allows precise focus alignment. The first aspherical lens (Edmund Optics GmbH, ED67283) is focused onto the atomic cloud position and collects the emitted fluorescence light of the covered $\Omega = \mathrm{NA}^2/4 \approx 5\%$ solid angle. An anti-reflection coating for 780 nm reduces the reflection of the collected light. The second objective lens (Edmund Optics GmbH, ED86917) focuses the light onto a pinhole, in order to suppress straylight originating from out-of-focus regions in the object plane. Two additional lenses image the pinhole positon onto the CCD camera. A shortpass filter with a cut-off wavelength at 850 nm is placed right in front of the CCD chip in order to reduce the transmission of the 1064 nm wavelength dipole beam. The measured transmission for 780 nm is 99.5 %. A cage system that holds the pinhole, the lenses and the shortpass filter, is mounted onto another three-dimensional translation stage, which allows for focus adjustment along the optical axis and for the selection of the region of interest in the lateral directions. The overall detection efficiency can be quantified by the sum of all transmission coefficients of the relevant optical component surfaces in conjunction with the covered solid angle and the quantum efficiency of the camera as $\eta \approx 4.21\%$. The two objective lenses additionally magnify the fluorescence image by a factor of $M = 2.62$. The CCD chip of the camera has 1024×1024 pixels with a physical size of $13\,\mu\text{m} \times 13\,\mu\text{m}$, which corresponds to an active area of $13.3\,\text{mm} \times 13.3\,\text{mm}$.

The main detection system is suited for the measurement of small atomic clouds, as it is the case for a BEC or a small detection MOT. For the investigation of larger clouds, such as in the 3D-MOT or in the quadrupole trap, two supplementary CCD cameras (UI-2210SE-M-GL, IDS) with C-mount connections are used. The first camera (K1) with a 25 mm objective lens (C2514-M, Pentax) is placed opposite to the main detection and pointing down at an angle of approximately 27° towards the 3 inch viewport of the science chamber. The second camera (K2) with a 25 mm objective lens (MeVis-C 1.6/25, Linos) and a working distance of 260 mm is positioned orthogonal to the main optical detection axis and elevated by approximately 45°, pointing to the science chamber through the 1 inch viewport. Both cameras are especially practical to evaluate the temperature of the atomic clouds by evaluating the size of the corresponding optical column density. The scale factor for the positions have been calibrated by conducting time-of-flight (TOF) measurements. The parabolic trajectories have been fitted by assuming a gravitational constant of $g = 9.81\,\text{m/s}^2$.

2.7 Experimental control

The operation of the experimental apparatus requires a precise control of the experimental parameters. The dynamical changes of the parameters need to be accurate and fast. To this end, a FPGA is used. A standard Peripheral Component Interconnect (PCI) card holding the FPGA is built on a dedicated computer system. The FPGA provides a total of 48 analog channels and 40 binary output ports (TTL-standard). The experiment control is driven by a LabView-based software program with a graphical user interface that runs on the FPGA.

CHAPTER 3

BEC generation with high repetition rates

This chapter describes the process of generating Bose-Einstein condensates with short cycle times by means of the underlying experimental setup, presented in the previous chapter. In general, the speed of the experimental apparatus is an important feature and can have a great impact on the performance of the conducted experiments. The capability of repeated high-speed measurements can provide reproducibility as well as reliability for the anticipated measurement results. In contrast, a prolonged experimental sequence will suffer from low sampling rates, which lead to a reduced temporal resolution and consequently longer statistical averaging times. For a BEC experiment, obtaining accurate and precise measurement results heavily relies on a set of various environmental and experimental control parameters, which are often subject to noise. The noise sources that can have an influence on the statistical error are in principle of two types: short- and long-term fluctuations. The distinction is defined by the cycle time of the experimental sequence. Fluctuations, such as in laser frequency or intensity are controlled and suppressed by negative feedback loops. Fast fluctuations are typically better controlled than slow drifts, which nevertheless can be tracked and corrected in post. A fast operation of the underlying apparatus and its underlying sequence will allow to be less sensitive to long term drifts.

The main objective in order to prepare a BEC is cooling a dilute atomic gas down to its critical temperature. Typical BEC experiments share similar procedures in the preparation process, which is often confronted with two main steps and usually attributed with a relatively large time consumption: the initial loading of a large number of atoms inside a 3D-MOT and the ensuing evaporative cooling process in a magnetic or optical trapping potential. The time needed for loading a 3D-MOT with a sufficiently large atom number primarily depends on the background gas pressure and the loading configuration, whereas the evaporation time scales with the trap confinement and the achievable collision rate, as well as the initial phase space density. As discussed in Chapter 1, the typical timescales for the preparation of a BEC can range from hundreds of milliseconds up to tens of seconds.

In the following sections of this chapter, the individual steps for a fast BEC preparation along with the corresponding optimization processes are explained. This chapter is divided into two parts, where the first part describes the double-MOT setup as a high-flux atom source. The second part lays out the approach of a hybrid evaporation scheme, where the total evaporation process is split into two steps that occur inside a magnetic quadrupole trap and a crossed optical dipole trap. A review of the full BEC sequence is given in the Appendix 6.2 and the specific limitations of the experimental setup, as a consequence of the speed requirements are discussed in Chapter 6.

3.1 High-flux atom source

The generic process for the production of a BEC with neutral alkali metal atoms requires the provision of an appropriate source, in order to supply a conservative trapping potential for the subsequent evaporative cooling steps. The further course of the experiment with respect to its overall speed can already be affected by the performance of the atom source in a considerable way. The most common limitation to a fast BEC generation is a relatively long evaporation time in the employed magnetic or optical dipole trap due to an insufficient number of trapped atoms or the lack of confinement strength. The speed and efficiency of the evaporation dynamics, which are driven and limited by the ratio of elastic to inelastic collisions, primarily depend on the provided initial number of atoms. Consequently, the initial supply of a large number of atoms, paired with a high density within the trapping potentials, allow to maintain or even enhance the elastic collision rate and thereby helps to significantly accelerate the evaporation process.[1] The provision of a large initial atom number not only benefits the speed of the experiment, but also ensures that a BEC with a large number of atoms is produced. This is particularly important for the pursued tasks of interferometric measurements, where the phase sensitivity can generally be improved by larger numbers of atoms.

Large numbers of atoms can principally be trapped by directly loading them from a background vapor into a 3D-MOT with sufficiently large MOT beams providing a large trapping volume. However, the loading from the background enforces the trapping potentials to be exposed to a persistent background pressure, which can deteriorate the atomic lifetimes in the subsequent steps of the experimental procedure.[2] This problem can be circumvented by transferring the trapped atoms into a separate ultra-high vacuum region, where they are shielded against the high background pressure. One example to transfer atoms between different vacuum regions is the principle of magnetic transport, where the atoms are guided by a magnetic conveyor belt consisting of an array of quadrupole coils operated with suitable currents [97]. A simpler version following the idea of transportation is achieved by mechanically driving a slider with a set of magnetic field coils [98], which transports the trapped atoms through differential pumping stages that ensure a pressure ratio of two orders of magnitude between the two vacuum regions [99]. For this method to be fast, a strong acceleration and deceleration of the heavy transport coils would be necessary, which could lead to concussion and unwanted vibrations to the overall vacuum system.

---

[1] Accelerated or "runaway" evaporation occurs when cooling the atomic sample leads to an increase in the density, which in turn leads to an increased elastic collision rate and thus a faster evaporation.

[2] The background pressure in the trapping region is particularly crucial for the employed fluorescence detection system. Loading and loss events due to a non-zero background level are detrimental for the single-atom-resolution.

On the other hand, different techniques have been established, in which a cold atomic beam is produced as a source to efficiently load a 3D-MOT. Well known examples for the usecase of a cold atomic beam are the Zeeman slower [100], chirp cooling setups [101] or two-dimensional magneto-optical traps [102]. The Zeeman and chirp cooling methods typically use powerful cooling beams that decelerate a thermal beam of atoms originating from an oven by means of radiation pressure. This is particularly useful for elements from the alkaline earth metal group, which have the property of extremely small vapour pressures at room temperature in contrast to alkali metals. In both cases, the atoms are slowed down only along the cooling beam axis, while spontaneous emission processes can result in the heating of atoms in the transverse directions. As a consequence a stronger diverging atomic beam with a flux of up to 10^{12} atoms/s can be achieved [103]. However, there are certain disadvantages, such as the bulk design and exceedingly large magnetic fields of a Zeeman slower or the need for a tunable cooling laser frequency, which make the utilization of a 2D-MOT setup more attractive towards a fast operating atom source [104]. This is especially practical for rubidium atoms, which can be produced by dispenser sources that are set up in a compact glass cell. A 2D-MOT has the additional benefit of transferring only a selected isotope within the natural abundance of rubidium atoms. Therefore, in this work, a double-MOT configuration is used in accordance to the two-chamber vacuum setup described in Section 2.2.

The following chapter describes the features of the double-MOT setup as a high-flux atom source and characterizes the 3D-MOT loading rate, which is a figure of merit for the speed of the first BEC preparation part.

3.1.1 MOT operation

The basic principle of a magneto-optical trap is to simultaneously cool and confine atoms of a thermal gas using a combination of a magnetic quadrupole field and a set of counter-propagating laser beams [105]. In this way, atoms can be cooled down to the sub-milli Kelvin range exploiting the dissipative scattering force provided by the laser beams. Photons moving in the opposite direction imprint their momentum onto the atoms by absorption, which results in a deceleration of the atoms. The confinement is ensured by a magnetic field gradient, which introduces a spatial dependence to the light forces. The linear magnetic field leads to a Zeeman splitting of the magnetic energy levels with the separation becoming larger further away from the trap center. The combination of the Doppler shift and Zeeman splitting keep each velocity class of the atoms at different magnetic field positions on resonance with the red detuned laser beams [106]. Figure 3.1 (a) shows the working principle of a magneto-optical trap in one dimension, which can be extended to two- and (b) three-dimensional configurations.

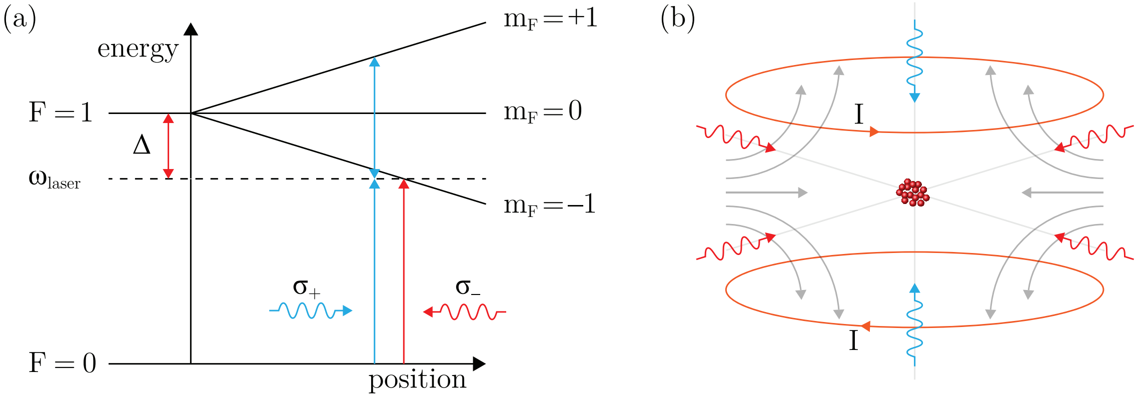

Figure 3.1: Principle of magneto-optical trapping. (a) The working principle of magneto-optical trapping is illustrated on the basis of an atom having two hyperfine levels $F = 0{,}1$ and moving in one dimension. The x and y axes represent the position and the internal energy of the atom. The dashed line depicts the laser frequency ω_{laser}, which is detuned by $\varDelta$ with respect to the $|F = 0\rangle \rightarrow |F = 1\rangle$ transition. The atom can be simultaneously cooled and trapped by letting it interact with two counter-propagating beams within the magnetic quadrupole field. The moving atom undergoes stimulated absorption and spontaneous emission cycles and thereby changes its resonance frequency due to the Doppler effect. In order to keep the atom always on resonance, a constant magnetic field gradient is applied, which leads to a linear splitting of the corresponding Zeeman levels m_F. This makes the atom selective to either left-handed σ_- or right-handed σ_+ circular polarization. Using the convention of the point of view of the receiver, only the σ_- polarization can drive the cooling transition. (b) Illustration of the trapping configuration in three dimensions. Two anti-Helmholtz coils with a current I produce an inhomogeneous magnetic quadrupole field with a minimum at the center. A pair of three counter-propagating beams with corresponding left- and right-handed polarizations cool the atoms inside the trap center.

3.1.2 2D$^+$-MOT setup

The optical setup for the 2D-MOT is built on a 750 mm × 450 mm breadboard table, which is elevated and rotated by 45° with respect to the main vacuum table. The breadboard is aligned parallel to the 2D-MOT glass chamber at a distance of 75 mm below its center. Figure 3.2 shows a top view of the setup in the breadboard's frame of reference. It has a rectangular cutout profile for the 2D-MOT glass chamber in order to provide access for the perpendicular direction along the z-axis. The optical components are therefore built on both sides of the breadboard. This inclined alignment opens the opportunity for optical access to the science chamber in the horizontal plane with respect to the main vacuum table. The 2D-MOT is realized inside the rectangular UHV glass cell with 59 mm × 59 mm × 149 mm dimensions. Three dispensers that contain a salt of rubidium in its natural abundance provide the atomic sources. They are attached onto the CF flange in a triangular arrangement around the differential pumping stage. One of the dispensers is

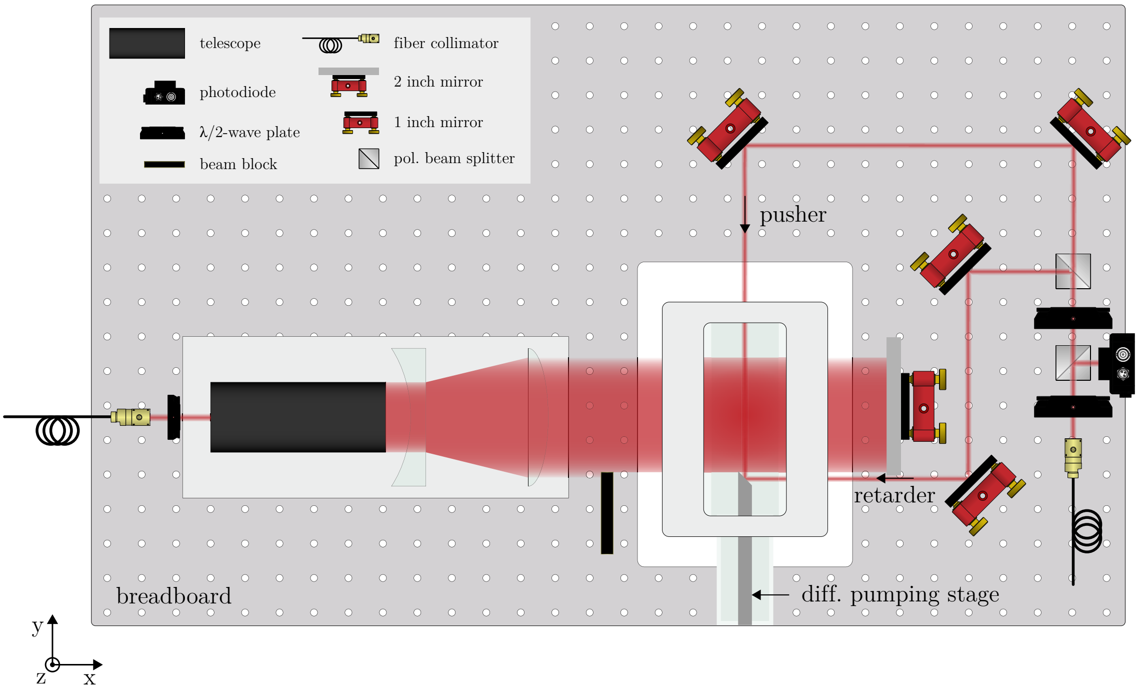

Figure 3.2: 2D$^+$-MOT setup. All light sources that are needed for the operation of the 2D$^+$-MOT are coupled via three PM fibers. The two cooling beams that contain a fraction of the repumping light are expanded by two telescopes and enter the 2D-MOT glass chamber from transverse directions (x- and z-direction). Due to the identical setup, only the respective optics of the second 2D-MOT beam path in the vertical direction are not shown. The pushing and retarding beams are overlapped with each other and aligned in longitudinal direction parallel to the differential pumping stage.

heated up by applying a current, which is fed through vacuum-sealed wire connections. As a consequence the salt is chemically reduced, which leads to the emission of atoms. The remaining two dispensers serve as spare rubidium sources until the first one is entirely depleted. The emitted particles can cause a coating of the inner glass cell surfaces, if the applied dispenser current is too high or the time duration running the dispensers is too long. In order to avoid immediate adsorption, the emitting slits of the dispensers are pointed towards the center of the trap and can be operated in a pulsed fashion.

The 2D-MOT light beams are derived from the optical setup table as described in Section 2.4.1. Two single-mode polarization-maintaining (PM) fibers deliver the mixed cooling and repumping light with 200 mW optical power, respectively. The beams are coupled out on both sides (top and bottom) of the breadboard and shaped by two identical telescope setups to elliptical waists of 43.5 mm × 15 mm [107]. A $\lambda/4$-wave plate in front of the telescopes ensures the circular polarization of the beams. After the telescopes the collimated beams enter the glass cell from transverse directions. The top beam follows a parallel beam path with respect to the breadboard plane and is retro-reflected by a rectangular $\lambda/4$-wave plate with a high-reflection coating on its backside. The same is true for the bottom beam, which is deflected by a mirror below the breadboard through the cutout profile and the glass cell until it is retro-reflected by another $\lambda/4$-wave plate mirror on top of the breadboard. The quarter-wave plates ensure the opposite circular polarizations of the counter-propagating beams. In addition, the glass cell is manufactured with anti-reflection coatings for 780 nm on its surfaces, which reduces the power imbalance of the counter-propagating beams.

The two light fields in conjunction with the set of four coils, as described in Section 2.3, form the 2D-MOT with the ability to shift the center of the trap by altering each individual coil current. In this way atoms can be guided to the science chamber through the differential pumping stage. For an even better performance of the 2D-MOT, a third light source with 5 mm diameter pointing along the longitudinal direction of the 2D-MOT glass cell is used. An additional fiber couples the same light as used for the 2D-MOT beams from the optical table to the top side of the 2D-MOT breadboard. The light first passes through a $\lambda/2$-wave plate and polarizing beam splitter (PBS), after which the reflected part of the light is used to monitor the power on a photodiode. A second $\lambda/2$-wave plate and polarizing beam splitter split the light into two orthogonally polarized beams. The reflected retarding beam is directed by two mirrors onto the 45° polished tip of the differential pumping stage. The entrance cap of the differential pumping stage imprints a spatial ring profile onto the retarding beam, which decelerates atoms not cold enough to stay in the trap center. Additionally, a beam block in the line-of-sight with the tip of the differential pumping stage is placed on the incoming horizontal 2D-MOT beam side, in order to avoid an acceleration of atoms away from the entrance cap. The transmitted pushing beam is directed by two mirrors to the differential pumping stage and overlapped with the counter-propagating retarding beam. The pushing beam is used to accelerate the longitudinally cooled atoms towards the science chamber. The total power of both beams is tuned to 16 mW for optimal loading of the 3D-MOT. This enhanced 2D-MOT setup is entitled as a 2D$^+$-MOT and enables a larger flux, lower mean longitudinal velocity and as a result a smaller width of the velocity distribution [108, 90].

3.1.3 3D-MOT setup

The optical setup for the 3D-MOT is necessarily realized on the vacuum system table (Fig. 3.3). A set of two fibers delivers the cooling and repumping light for the 3D-MOT distribution optics, which are supported by three breadboards around the glass chamber at a height of 225 mm. The fibers are connected to two fixed focus triplet collimators, which provide a beam diameter of 3 mm. This corresponds to a rayleigh length of $z_R \sim 9\,\mathrm{m}$. The outcoupled beams are first cleaned in polarization by Glan-Thompson polarizers with an extinction ratio of $\eta \approx 10^5$. The intensities of both beams are stabilized by sending a fraction of each light source onto two respective photodiodes by $\lambda/2$-wave plates and polarizing beam splitters. These signals are then used as a feedback for the input of home-build PID controllers. The controllers regulate the radio-frequency power of each AOM and thereby the power of the light in front of the fibers. Both beams are then overlapped by a polarizing beam splitter, forming the driving fields for the 3D-MOT. The resulting beam is split up in power by a 90:10 beam splitter, which allows to operate the 3D-MOT in two configurations: the initial 3D-MOT that provides the atoms for loading into the quadrupole trap and the detection MOT (d-MOT) that is suited for the detection of the atomic ensembles with single-particle-resolution, as discussed in Section 4.1.3. The 3D-MOT path with high intensity is sent through a beam expander, which increases the beam diameter to ~15 mm and provides a large trapping volume. In contrast, the d-MOT path has less total power and a smaller beam size in order to minimize fluorescence noise for the detection resulting from possible glass cell surface reflections. After the power splitting and beam shaping both beams are overlapped again by a 50:50 beam splitter, after which they share the same common beam paths. The MOT configurations can be switched by two respective shutters in front of the combining beam splitter. Both output ports of the combining beam splitter distribute the power into six concatenated beam paths by passing combinations of additional $\lambda/2$-wave plates and polarizing beam splitters, which are used to adjust the power imbalance of the counterpropagating beam pairs. The horizontal beams enter the 3 inch viewports of the science chamber at an angle of 45°. This arrangement has the advantage of a comfortable detection direction and allows to get close to the science chamber and exploit the high numerical aperture objective lens. Conical chamfers on the front edge of the first objective lens mount, as well as on the quadrupole coils copper mounts are constructed in order not to cut the big horizontal 3D-MOT beams. The vertical top and bottom beams are first directed with periscope setups to levels above (third breadboard) and below (main vaccum table) the center level and then guided through the vertical 1-inch viewports of the science chamber. As it is discussed in Section 5.1, the detection MOT configuration is replaced by an optical fiber-based MOT setup, which will improve the capabilities for single-atom-resolved detection.

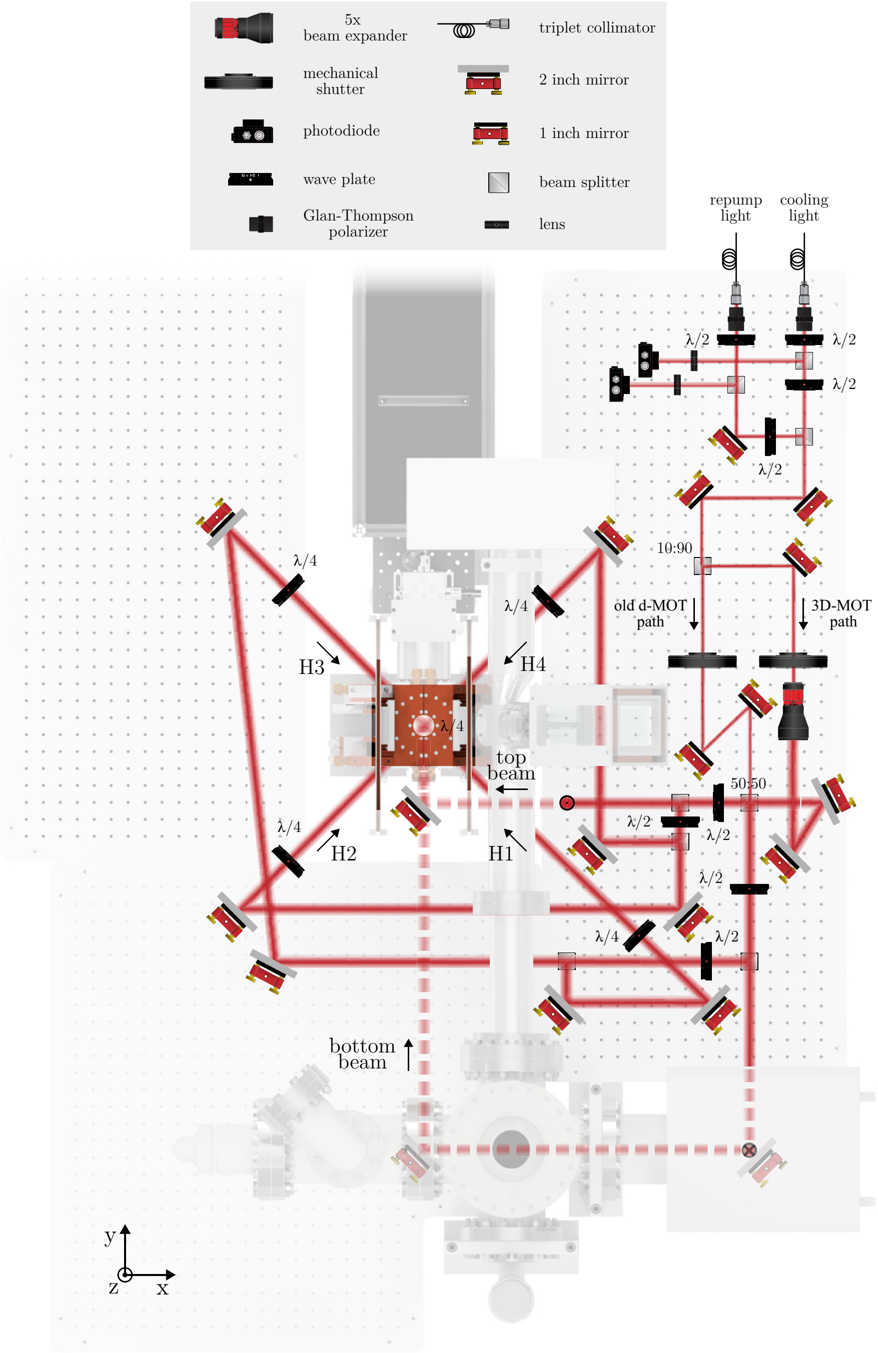
5x beam expander
triplet collimator
mechanical shutter
2 inch mirror
photodiode
1 inch mirror
wave plate
beam splitter
Glan-Thompson polarizer
lens
repump light
cooling light
λ/2
λ/2
λ/2
λ/2
10:90
old d-MOT path
3D-MOT path
λ/4
λ/4
H3
H4
λ/4
top beam
50:50
λ/2
λ/2
λ/4
H2
H1
λ/2
λ/4
λ/2
bottom beam
y
z
x

Figure 3.3: 3D-MOT setup. The layout of the 3D-MOT setup with a top view on the vacuum table. The 3D-MOT setup can be used in two independent configurations: the enlarged 3D-MOT beams are used to prepare large numbers of atoms, whereas the small 3D-MOT beams can be used for detection. Both configurations are overlapped at a 50:50 beam splitter and share the same optical paths.

3.1.4 2D$^+$-/3D-MOT characterization

The performance of the double-MOT setup and thus the time needed for the preparation of large atom numbers is characterized by the number of atoms per second that can be transferred from the 2D-MOT into the science chamber, where they are loaded into the 3D-MOT and held for further magnetic trapping. A crucial figure of merit is the initial loading rate of the 3D-MOT, which depends on a set of contiguous 2D- and 3D-MOT parameters. The 2D-MOT setup that is used in this apparatus was part of a different experimental setup and had been characterized in detail in a former PhD thesis [109]. Almost all components of the 2D-MOT were adopted due to its former excellent performance. However, during the rebuilding of the 2D-MOT new dispensers were implemented. In the following, the characterization of the 2D-MOT is mainly focused on the characteristic behaviour of the employed dispensers and their influence on the loading rate of the 3D-MOT. For this, the number of atoms inside the 3D-MOT was recorded with two different detection methods. The fluorescence of the atoms was captured with a CCD camera (see Section 2.6) and additionally imaged onto a photodiode by a single lens with a diameter of $d = 25.4\,\mathrm{mm}$ and a focal length of $f = 100\,\mathrm{mm}$. In addition to the CCD camera, the benefit of the photodiode is the continuous measurement of the atom number during the loading time, which enables to estimate the loading rate on the fly.

Loading rate measurements

A significant impact on the 2D-MOT flux can be expected by the influence of the dispensers, since they are the direct source of rubidium atoms. The current through the dispensers regulates the emission of atoms and consequently the background pressure inside the 2D-MOT chamber. The dispensers can be operated in two modes: a continuous operation with a static current and a pulsed operation, where the current is remotely switched on only during the loading time and switched off otherwise. In order to quantify the influence of the dispensers, the loading rate of the 3D-MOT is investigated for different dispenser current values both in pulsed and continuous operation. Figure 3.4 (a) shows typical loading curves of the 3D-MOT, where the number of atoms is measured as a function of the loading time. The dispenser is operated in a pulsed fashion and the current is varied from 0 A to 5.2 A. The number of atoms inside the 3D-MOT increases for higher dispenser currents, as more and more atoms are released. The initial loading rates are extracted from the loading curves by linear fits and are shown in Fig. 3.4 (b). The loading rate scales nonlinearly with increasing dispenser current. Although, a supposedly exponential increase of the loading rate marks up, there will be a certain threshold until the loading rate breaks down again. This is a result of flooding the glass chamber with too many rubidium atoms, such that light-assisted collisions of excited cold atoms with the background increase to a point where the cooled atoms are predominantly lost. This behavior is shown in the aforementioned PhD thesis with a similar 2D-MOT setup [109]. The dispenser current is intentionally increased up to only 5.2 A in order to avoid flooding the science chamber with too much rubidium and accompanied contaminants. This is a precaution measure for keeping the ultrahigh vacuum condition in the science chamber, while preventing the

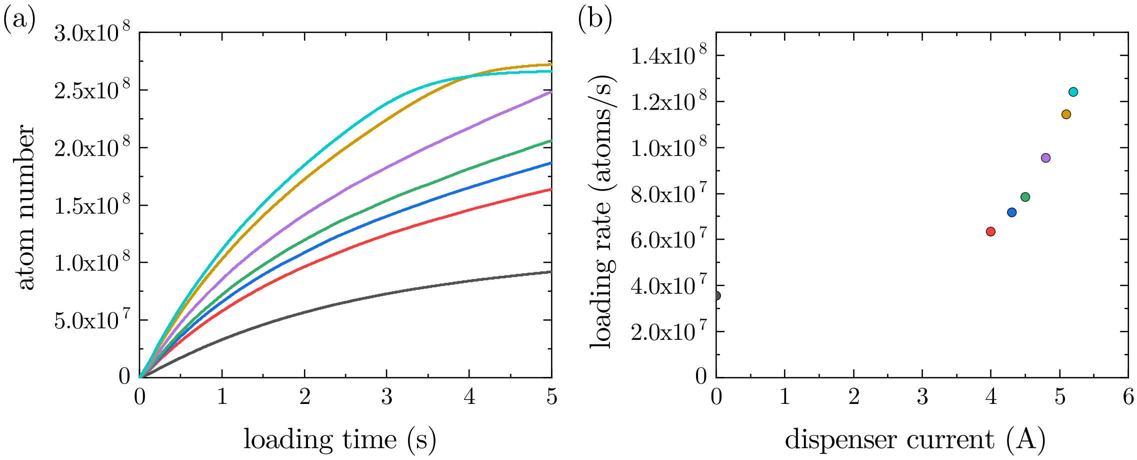

Figure 3.4: 3D-MOT loading rates and atom numbers for a pulsed dispenser operation. Increasing atom numbers and loading rates are marked in color starting with 0 A (black) to 5.2 A (cyan). (a) 3D-MOT loading curves as a function of loading time for different dispenser currents. The loading curves are statistical averages over many experimental cycles and are low-pass filtered. (b) Initial loading rate of the 3D-MOT as a function of loading time for different dispenser currents. The error bars are smaller than the symbol sizes.

blow-off of the dispenser. Running the dispensers at a high current and for a long time resulted in the loading of the 3D-MOT solely from the background gas inside the science chamber. This behaviour is illustrated in Fig. 3.4 (b). For zero dispenser current, a persistent background pressure exists, which is sufficient to load atoms from. This residual background pressure is a result of the operation mode and duty time of the dispensers, which to this date are running for four years. The reported loading rates in Ref. [109] are about three orders of magnitude higher for similar dispenser currents, except in continuous operation. In contrast, the loading rate measurements from Fig. 3.4 were interleaved in a sequence, which additionally measured the lifetime of the dipole trap as a quality check for the ultrahigh vacuum inside the science chamber.[1] The holding time for the dipole trap was incremented from $0-10\,\mathrm{s}$ in steps of 2 s, which in conjunction with the 5 s loading time of the 3D-MOT yields an effective average duty cycle of ∼50% for the dispenser. Timetrace measurements in Fig. 3.5 (a,b) show the qualitative dynamic behaviour of the dispenser for different currents and modes of operation. The loading rate and final atom number in the 3D-MOT are measured over a time period of one hour. The onset with 0 A dispenser current marks the offset. After 13 minutes the dispenser current is switched on to 4 A and ran continuously, which immediately increased the loading rate and consequently the final atom number by one order of magnitude. After 27 minutes the dispenser is switched

---

[1] The monitoring of the vacuum condition with this criterion or with the pressure gauge was not sensitive enough. A more precise insight about the vacuum can be achieved by monitoring the background loading of the 3D-MOT.

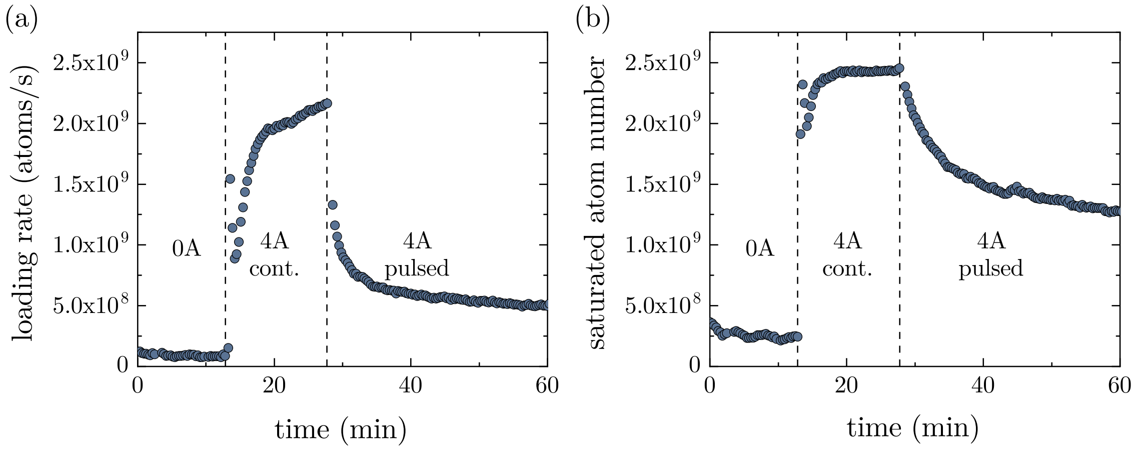

Figure 3.5: 3D-MOT loading rates and saturated atom numbers for different dispenser operations. The time trace measurements show the dynamical evolution of (a) the loading rates and (b) final atom numbers. The solid vertical lines indicate the change of the dispenser operation.

on for 5 s with a duty cycle of 54% and caused a quick drop in the loading rate as well as in the final atom number. A comparison with Fig. 3.4 (b) shows that the increase in duty cycle for a pulsed operation leads to an increase in the loading rate by a factor of 3. However, it is important to note that a consistent loading rate can only be defined, if the pressure level does not change with time and the background gas is in thermal

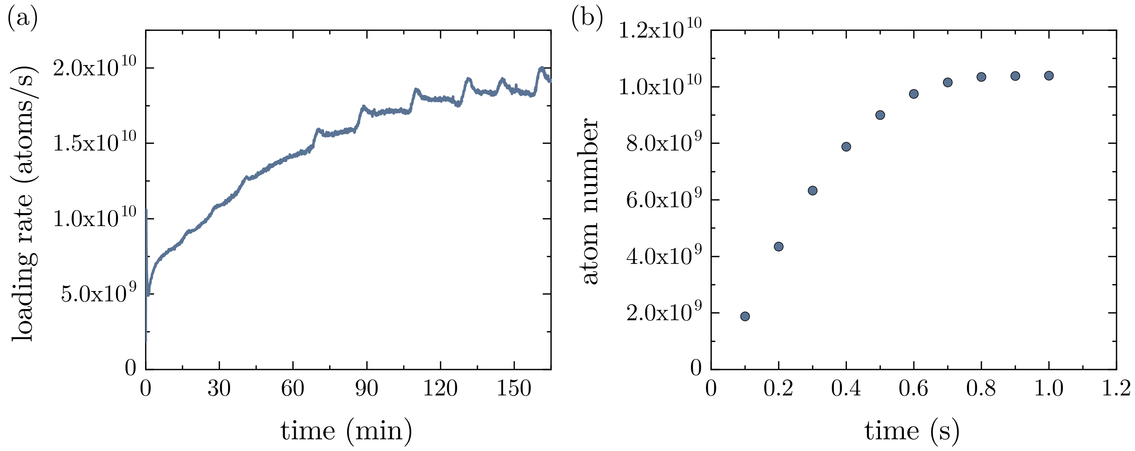

Figure 3.6: 3D-MOT Loading rate and atom number for a continuous dispenser operation. The dispenser is operated continuously at a current of 4 A. (a) The 3D-MOT loading rate increases after turning on the dispenser and slowly starts saturating after approximately two hours. (b) After saturation of the loading rate, a final atom number of $\sim 10^{10}$ atoms in the 3D-MOT is reached within 600 ms.

equilibrium. The recorded data does not fully cover the settled values for the different cases, as more time would be needed. In particular, for the continuously operated dispenser at 4 A the background pressure is still building up. Therefore a longer timetrace was recorded for about two and a half hours and is shown in Fig. 3.6 (a). By the end of the measurement time, the loading rate increased by about a factor of two until it seemingly starts to equilibrate at 2×10^{10} atoms/s. With the increased loading rate, in comparison to the pulsed mode in Fig. 3.4 (a), the 3D-MOT is loaded faster within 600 ms as shown in Fig. 3.6 (b). The optimum loading rate for the continuous dispenser operation is in good agreement with a previous characterization for a given total cooling light power of 400 mW. As the experiment is aimed for fast cycle rates and the fact that much more current is needed in order to achieve the same loading rate in the pulsed mode, the decision was made to run the dispenser continuously, but at a rather moderate dispenser current. It is worth to mention that a compromise needs to be found between the optimum loading rate and the background gas pressure inside the science chamber.

Frequency detuning

In order to quantify the influence of the 2D-MOT cooling light frequency detuning Δ with respect to the $\left|5^2S_{1/2},\mathrm{F}=2\right\rangle \rightarrow \left|5^2P_{3/2},\mathrm{F'}=3\right\rangle$ hyperfine transition, the final number of atoms in the 3D-MOT was measured as a function of the 2D-MOT AOM center frequency, normalized by the natural linewidth Γ given in MHz (Fig. 3.7). The asymmetric lineshape yields the optimum frequency detuning at $-3.1\,\Gamma$. This result is in accordance with a previously optimized characterization.

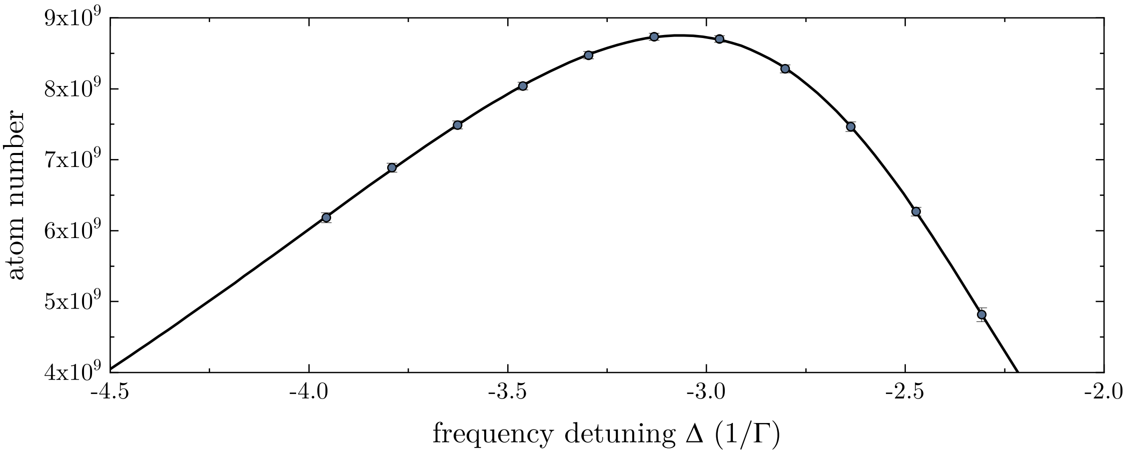

Figure 3.7: 2D-MOT frequency detuning. 3D-MOT atom number as a function of the detuning Δ in units of the natural linewidth Γ. The detuning was scanned by changing the center frequency of the 2D-MOT AOM in double-pass configuration.

3.2 Hybrid evaporation

Laser cooling of large numbers of atoms inside a MOT provides Doppler temperatures of a few hundreds of microkelvins and a good starting point towards increasing the spatial density of the atomic cloud. However, upon adding more and more atoms, at a certain point, the cloud becomes opaque to the cooling light. This leads to a rescattering of the photons and as a result to an effective repulsive force between the atoms [110, 111]. The densities of standard achievable MOTs are typically limited to $n \approx 10^{10}–10^{11}\,\mathrm{cm}^{-3}$. Any further increase of the atom number results in a constant density $n = N/L^3$, where the size scales with $L \propto N^{1/3}$ [112]. Therefore, in order to reach the quantum phase transition for Bose-Einstein condensation, one has to resort to evaporative cooling techniques, where the further reduction of the temperature (i.e. gain in phase space density) is connected with a deliberate ejection of atoms from the trapping potential. The efficiency and the speed of the evaporative cooling process depend on the elastic collision rate.

Evaporative cooling until quantum degeneracy can be employed in different magnetic or optical potentials. This work describes the generation of Bose-Einstein condensates using a hybrid evaporation approach combined in a magnetic quadrupole (QPT) and a crossed optical dipole trap (cODT), which avoids their individual weaknesses. The QPT is utilized as the connecting link between the 3D-MOT and the cODT, due to its efficient capture of atoms from the 3D-MOT and subsequent transfer into the cODT. In the QPT, a first forced radio-frequency evaporation step is employed in order to increase the initial spatial density of the cloud. The strong spatial confinement in the vicinity of the magnetic trap center allows to transfer atoms into the steep dipole trap, by adiabatically lowering the magnetic field gradient below gravity. Atoms are thereby loaded from a linear to a Gaussian potential. This is realized by focusing the cODT beams approximately a waist size below the quadrupole trap center. The final evaporation step in the cODT is realized by quickly lowering the optical power.

The following sections describe the properties, the transfers and evaporation processes within the employed magnetic and optical trapping potentials.

3.2.1 Magnetic trapping

Magnetic trapping relies on the interaction between the internal magnetic moment $\boldsymbol{\mu}$ of the atom and an external inhomogeneous magnetic field $\boldsymbol{B}(\boldsymbol{r})$, which leads to a shift in the atomic energy levels

$$\mathit{\Delta} E = -\boldsymbol{\mu}\boldsymbol{B}(\boldsymbol{r}). \tag{3.1}$$

The magnetic moment is proportional to the total angular momentum $\boldsymbol{F}$, which defines the atomic hyperfine states. In the presence of an external magnetic field, the hyperfine states split up into Zeeman sublevels m_F and the energy shift is given by

$$\mathit{\Delta} E = m_F g_F \mu_B |\boldsymbol{B}|, \tag{3.2}$$

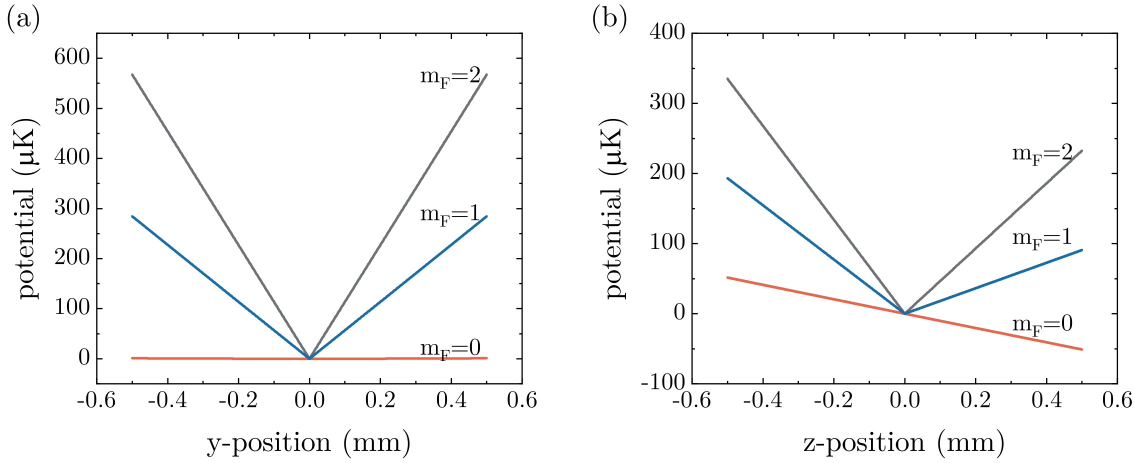

Figure 3.8: Magnetic potential for different Zeeman states. The Zeeman energy levels are calculated for the two low-field seeking hyperfine states with $m_F = +2,+1$ and the non-magnetic state $m_F = 0$ along (a) the strong confinement axis and (b) the radial z-direction. The positive z-direction points along gravity. The energy levels are are given with respect to the trap center.

where g_F is the Landé factor and μ_B is the Bohr magneton. The alignment of the magnetic moment with respect to the magnetic field axis classifies, whether the atoms are attracted to regions with small ($m_F g_F > 0$) or large ($m_F g_F < 0$) magnetic field magnitudes. According to Earnshaw's theorem the trapping of atoms is only possible for magnetic fields with a local minimum [113]. This is realized by the quadrupole trap in an anti-Helmholtz configuration (see Section 2.3) and is described by a three-dimensional linear potential

$$U(x,y,z) = \alpha\sqrt{4x^2 + y^2 + z^2}, \qquad \alpha = \frac{1}{2} m_F g_F \mu_B dB/dx \tag{3.3}$$

where dB/dx is the magnetic field gradient along the strong confinement axis [114]. The two hyperfine ground state manifolds $|F = 1{,}2, m_F\rangle$ of ^{87}Rb yield in total three magnetically trappable states $|1,-1\rangle$, $|2{,}1\rangle$ and $|2{,}2\rangle$. The strongest confinement by the quadrupole field is realized for the $|2{,}2\rangle$ state, which contains the largest magnetic moment. The calculated energy levels for the $|F = 2, m_F = +2,+1,0\rangle$ states are illustrated in Fig. 3.8 (a,b). Only the $|2{,}1\rangle$ and $|2{,}2\rangle$ states are confined in the quadrupole trap, whereas the $|2{,}0\rangle$ is magnetically insensitive.

At the center of the trap, the magnitude of the magnetic field is zero and the potential has a minimum. The magnetic field gradient along the longitudinal x-axis is constant and has a value of 169 G/cm. In the radial y- and z-directions, the gradient is a factor of two smaller. This value is sufficient in order to compensate the gravitational potential for the atoms in the $m_F = 2$ substate, for which the magnetic field gradient needs to be equal to or larger than 15.3 G/cm.

3.2.2 State preparation

Molasses cooling

The temperature of the atomic cloud inside the MOT is typically close to the Doppler limit with a few hundreds of μK and its size extends over a large trapping volume, provided by the 3D-MOT beams. As a next step, the atoms need to be transferred into the magnetic quadrupole trap. In comparison to the MOT, the quadrupole trap provides a large trapping volume. Thus for an efficient loading, the temperature of the atomic cloud is reduced even further by employing polarization gradient cooling [115]. This is realized within an optical molasses, where the MOT beams are set to far-red detuning and the MOT magnetic field is simply switched off. The efficient cooling depends on the power balance of the 3D-MOT beams and additionally on the magnetic background field, which is compensated with three pairs of rectangular compensation coils framing the entire vacuum table from all three orthogonal spatial directions. The optical molasses is applied for 6 ms with an optimal frequency detuning of $-17\,\Gamma$. The temperature of the atomic cloud is characterized by taking fluorescence images for variable times of free fall [116]. After releasing the atoms from the optical molasses, the cloud will expand isotropically with a mean velocity, which is given by the Maxwell Boltzmann distribution. The spatial distribution can be approximated by a Gaussian profile and the temperature during the free expansion time t is related to its width

$$\sigma(t) = \sqrt{\sigma_0 + t^2 \frac{k_B T}{m}}, \tag{3.4}$$

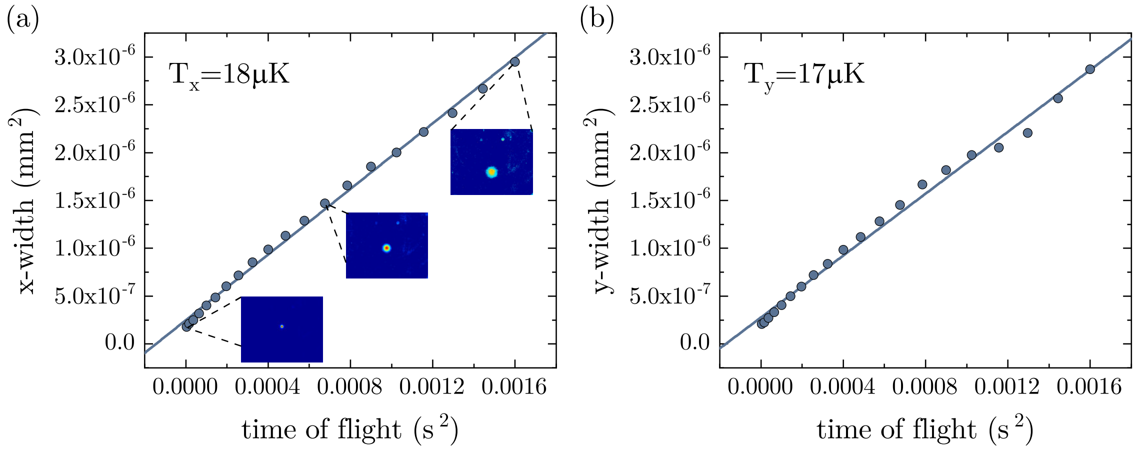

Figure 3.9: Optical molasses temperatures. The temperature of the atomic cloud is measured for the (a) horizontal and (b) vertical direction by means of fluorescence detection. The width of the Gaussian distributions are fitted for 2−40 ms of free expansion times. The insets show example false color images of the atomic clouds for 2 ms, 26 ms and 40 ms free fall times.

where σ_0 is the initial width, k_B is the Boltzmann constant, m is the mass of the rubidium atom and T is the temperature. The time of flight measurements are shown in Fig. 3.9 (a,b) for two orthogonal camera directions. A linear fit of the squared widths as a function of the squared times yields for both directions isotropic temperatures of $T_x = 18\mu\text{K}$ and $T_y = 17\mu\text{K}$. These temperatures are sufficient for loading the atoms into the quadrupole trap.

Optical pumping

The linear magnetic potential of the quadrupole trap depends on the magnetic sublevels m_F. After sub-doppler cooling, the atoms are still distributed over all magnetic sublevels $m_F = -2,...,+2$ of the $F = 2$ manifold, which is a result of the inherent polarization components of the cooling beams. Since all of the states are equally populated, the loading efficiency into the QPT would be on average 2/5. As a consequence, the atoms are prepared in the magnetically most sensitive $|F = 2, m_F = +2\rangle$ state by employing an optical pumping pulse. The principle of the optical pumping scheme is visualized in Fig. 3.10. A homogeneous magnetic field splits the energy levels by means of the linear Zeeman effect. The initially distributed atoms in the $|F = 2, m_F\rangle$ states, except for the target or dark state $|F = 2,2\rangle$, are addressed by the same σ_+ polarized beam, which excites them to the $|F' = 2, m_F\rangle$ states, while changing their magnetic quantum number by $\Delta m_F = +1$. Spontaneous emission leads to a decay back into the ground state. Hereby, the magnetic quantum number can change by $\Delta m_F = -1,0,+1$. However, once the atoms fall back into the dark state after a sufficient number of cycles, they will remain in that state and the transfer is completed. Thus, the atoms are in a low-field seeking state and will be trapped in the minimum of the magnetic field.

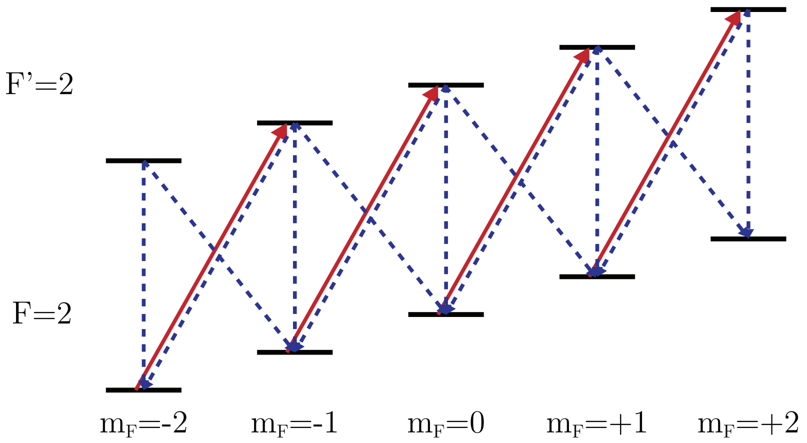

Figure 3.10: Optical pumping scheme. A σ_+-polarized beam (red arrows) transfers the atoms to the dark state $|F = 2, m_F = 2\rangle$ after a sufficient amount of cycles. The decay from the excited states to the ground states are indicated by the blue dashed arrows.

3.2.3 Loading into the quadrupole trap

The loading of the QPT is initiated by switching off the shutters for the cooling light of the optical molasses. Simultaneously, the homogeneous magnetic field coil current is switched on. For an optimal transfer into the QPT, a stable magnetic field reference is needed. The magnetic field can be stabilized by a fluxgate sensor (Fluxgate Bartington), attached to the quadrupole copper mounts in conjunction with a home-build PID controller. However, in the case of the optical pumping the stabilization circuit is set to open-loop control (i.e. current stabilization mode), where the PID applies the read-in setpoint to the output current. The reason for this is that the homogeneous field is still turned on during the QPT ramp up. The high magnetic field of the QPT immediately saturates the sensor once the QPT is turned on, which makes the magnetic field stabilization useless. However, the optical pumping transition is not too sensitive with respect to magnetic field fluctuations. Thus, the current setpoint is chosen, such that the magnetic field at the sensor position corresponds to a calculated magnetic field of $\sim$3.5 G. In this way, the quantization axis is fixed along the x-direction, which is perpendicular to the principle quadrupole trap axis. After a holding time of 200 μs, an optical pumping pulse is switched on for 240 μs. The optical pumping beam with 13 mm diameter and 250 μW power enters the science chamber along the x-axis from the rear one-inch viewport of the glass cell and carries a counterclockwise circular polarization. The propagation direction is opposite to the homogeneous magnetic field axis, such that only σ_+-transitions are driven. The optical pumping frequency is blue-detuned by 3.4 Γ with respect to the $|^5S_{1/2}, F = 2\rangle \rightarrow |^5P_{3/2}, F' = 2\rangle$ transition. During the pulse, the repumping light of the 3D-MOT is turned on, such that the atoms are pumped out of the $|F = 1, m_F\rangle$ manifold and kept in the cycling transition. After a second short holding time of 20 μs, the quadrupole trap is switched on and the magnetic field gradient is linearly ramped up from 58 G/cm to 169 G/cm in 50 ms. This corresponds to a ramp of the coil current from 32 A to 94 A. The QPT coil current is controlled and stabilized by a home-built PID controller, which controls the output of the power supply. A current transducer is used as the measurement signal. Compared to the possible maximum rating of the corresponding 150 kW power supply (see Section 2.3), the moderate current values are prescribed by the operation temperature of the coils. The maximum QPT coil current was chosen in order not to overheat the coil wire insulation layers and thereby prevent a shortcut inside the coil layers.

A crucial requirement for the efficient loading of the QPT is to match the position of magneto-optical and quadrupole traps in order to avoid heating [117, 118]. The positions of the individual traps were estimated by Gaussian fits of the corresponding fluorescence images and are shown in Fig. 3.11 (a,b) for two separate camera directions. Due to the inclined positioning of the cameras, the vertical directions are coupled with the corresponding orthogonal horizontal component. The results represent a quantitative measurement of the assembled coil system tolerances. The QPT and MOT centers are about 100 μm apart from each other, which indicates a good overlap. The residual displacement of the center positions between the optical molasses and the quadrupole trap inevitably leads to an increase of the atomic cloud temperature. The more extended the cloud size is, the larger

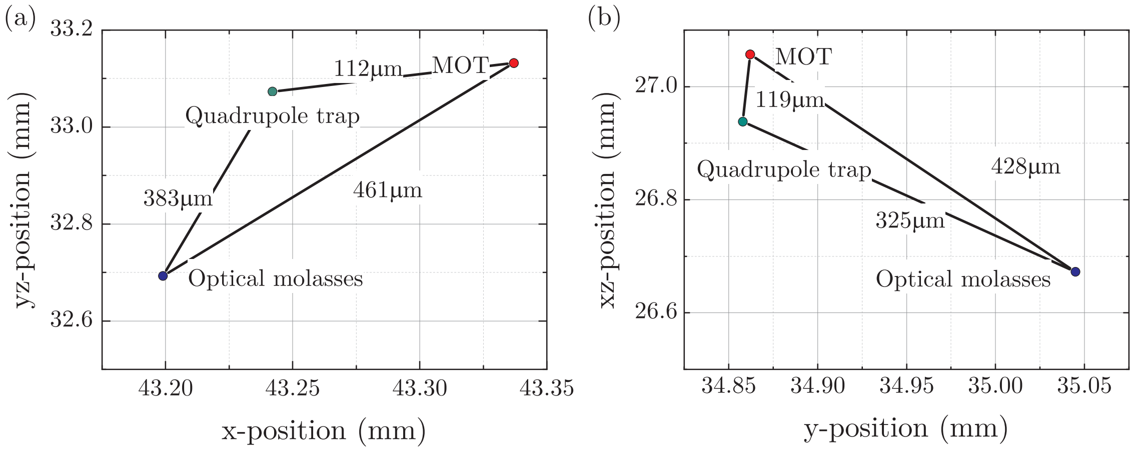

Figure 3.11: MOT, optical molasses and QPT positions. The center positions of the atomic density profiles within the MOT, optical molasses and QPT are measured from two orthogonal directions (a) the x-direction and (b) the y-direction.

is the gained potential energy by the atoms due to the Zeeman shift. The center offset causes then an acceleration towards the minimum of the magnetic quadrupole field, which results in thermal energy.

A temperature measurement after loading into the QPT at a magnetic field gradient of 58 G/cm is shown in Fig. 3.12 (a,b). The temperatures increase to $T_x = 106\,\mu$K and $T_y = 145\,\mu$K. The difference reflects the larger confinement in y-direction. A different approach to optimize the overlap between the QPT and the MOT would be the application of a compressed MOT (cMOT) by adiabatically ramping up the MOT magnetic field gradient and thereby making the atomic cloud smaller and denser.

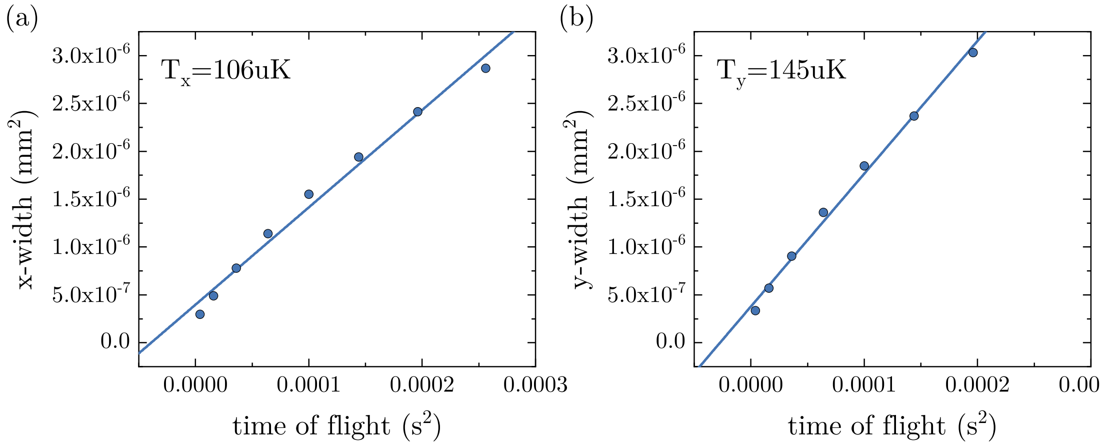

Figure 3.12: QPT temperature. The temperature of the atomic cloud is measured for the (a) x- and (b) y-direction by means of fluorescence detection. The width of the Gaussian distributions are fitted for 2−14 ms of free expansion times.

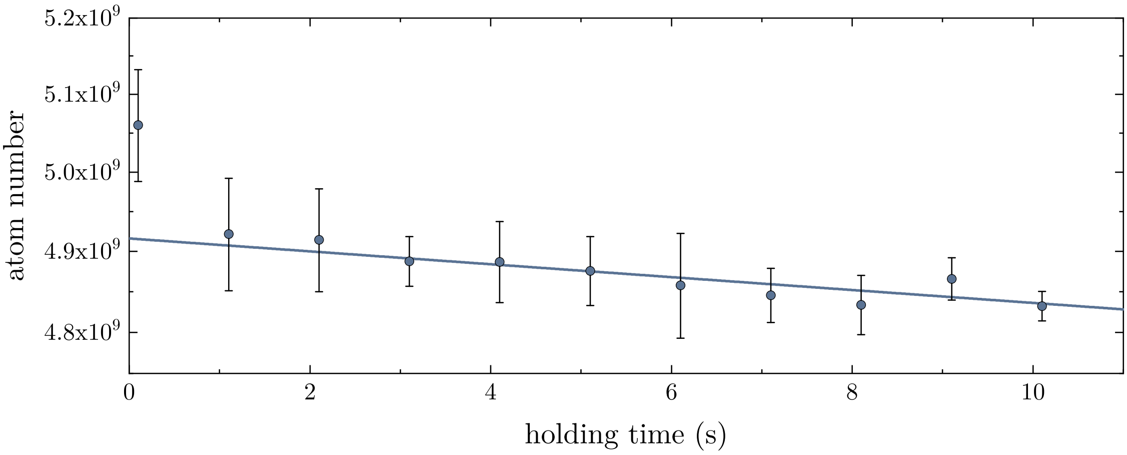

Figure 3.13: QPT lifetime. The number of atoms is measured as a function of the holding time inside the QPT. The initial drop is caused by the atom loss during the transfer process.

The overall loading efficiency is about 90% with typically 5×10^9 trapped atoms. The lifetime of the QPT was investigated by taking fluorescence images for different holding times up to 10 s and is shown in Fig. 3.13. After an initial drop of 3%, the atom number decays almost linearly with increasing holding time. An exponential decay fit gives a $1/e$ lifetime of $\tau = 10\,\text{min}$. A more precise measurement of the lifetime is limited by the coil temperatures. However, the estimated lifetime is sufficiently long for the subsequent evaporative cooling process.

3.2.4 Radio-frequency evaporation in the quadrupole trap

After the loading into the QPT, the subsequent step is to further increase the phase space density, such that the atoms can optimally be transferred into the dipole trap. To this end the atoms are cooled by using forced radio-frequency evaporation [119, 120]. The basic idea is to expell atoms with more than the average energy of the cloud from the QPT and allow the ensemble to thermalize towards lower temperatures through elastic collisions. The principle scheme is illustrated in Fig. 3.14. The atoms are prepared in the low-field seeking $|F = 2, m_F = 2\rangle$ substate and are spatially distributed over the trapping potential. Atoms with higher energy tend to move further away from the trap center and are therefore removed preferentially. The removal of atoms is established by subjecting them to a spatially uniform radio-frequency magnetic field. Hereby, atoms that satisfy the resonance condition will absorb an RF photon and make a transition by changing their angular momentum by $\Delta m_F = -1$. Since the energy level separation between the m_F sublevels is equal to first order, the transition is part of a multi-photon process. After the absorption of four RF photons, the spin will eventually flip and leave the atom in a high-field seeking state $|F = 2, m_F = -2\rangle$. Thus, as a consequence, the atoms are accelerated away and removed from the trap. After removing the excess energy, which is carried away by

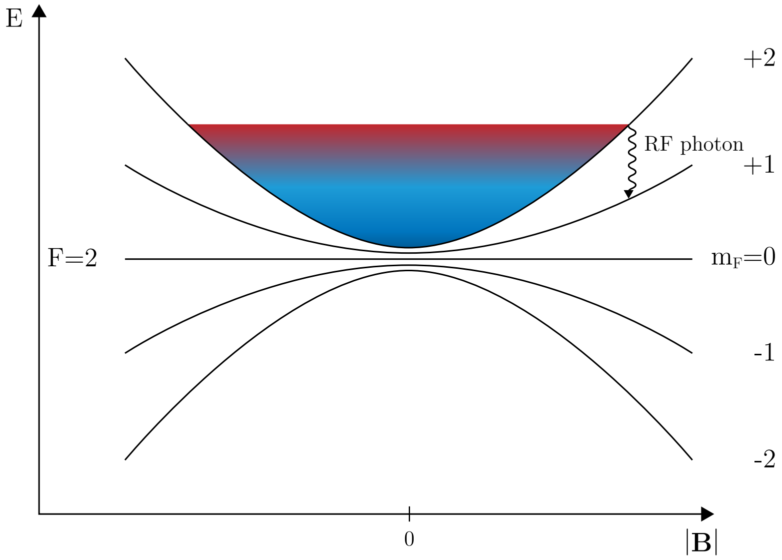

Figure 3.14: Forced RF evaporation scheme. The atoms are trapped in the high-field seeking $|F = 2, m_F = 2\rangle$ state. The dressed Zeeman energy levels form an avoided crossing in the vicinity of the trap center. The radio-frequency photons couple the different m_F sublevels.

the highest energetic atoms, a new thermal equilibrium will be established that is again characterized by a Maxwell-Boltzmann distribution. By sweeping down the radio frequency, the evaporation is forced to continue, while successively the temperature decreases and the density increases.

The radio frequencies for evaporation are generated by a direct digital synthesizer (DDS), which supplies frequencies of up to 200 MHz. The internal electric circuitry causes a generation of several higher harmonics, which are attenuated by employing a low pass filter (MiniCircuits, SLP-90+ DC-81 MHz) that is directly connected to the output of the DDS. The sweeping of the RF signal is controlled by the synthesizer's voltage controlled oscillator mode. The output power of the synthesizer is at maximum ~13 dBm. For sufficient power the output is fed into a power amplifier with a variable gain of up to 15 W. The coupling of the radio-frequency signal to the atoms is realized by a double loop antenna, which is wound horizontally around the science chamber (see Section 2.3).[1]

The evaporation in the QPT is initiated shortly after (10 μs) the magnetic field gradient is ramped up to its maximum value of 169 G/cm. The radio frequency is ramped down from 28 MHz to 3.5 MHz within a total time of 1.6 s. The ramp is divided into three linear steps and optimized for maximum atom number in the cODT. A summary of the evaporation ramps is given in Table 3.1.

---

[1] The single loops are separated by ~27 mm and are placed as close as possible to the atoms, due to the obvious impedance mismatch, which is caused by the copper wire length and the large frequency range.

Table 3.1: QPT evaporation ramp parameters. The ramps start with the end frequency of the corresponding previous ramp. The splitting of the $|F=2,m_F\rangle$ states translates to magnetic fields via $\Delta E/(hB) = 0.7\,\mathrm{MHz/G}$.

ramp no.	duration (ms)	start freq. (MHz)	stop freq. (MHz)	start magn. field (G)	stop magn. field (G)
1	600	28	16	40	22.9
2	800	16	6	22.9	8.6
3	200	6	3.5	8.6	5

3.2.5 Optical dipole trapping

In contrast to magnetic trapping, optical dipole traps offer the additional benefit of having control over the internal atomic states. The main working principle of the optical dipole trap relies on the interaction of the induced atomic dipole moment $\boldsymbol{p}$ with a focused, far off-resonant intense laser beam. The oscillating electric field $\boldsymbol{E}$ leads to an intensity-dependent AC-Stark shift [121, 122]. The corresponding dipole trap potential is thus proportional to the spatially varying light intensity

$$U_{dip}(x,y,z) = -\frac{1}{2}\langle \boldsymbol{pE}\rangle = -\frac{1}{2\varepsilon_0 c}\mathcal{R}(\alpha) I(x,y,z), \tag{3.5}$$

where ε_0 is the electric permittivity, c is the speed of light in vacuum, α is the complex polarizability[1] of the atom and $I(x,y,z)$ is the intensity of the laser beam. The spatial intensity distribution of an elliptic Gaussian beam with a total power P propagating in the z-direction is described by

$$I(x,y,z) = \frac{2P}{\pi\omega_x^2(z)\omega_y^2(z)} \exp\left(-\frac{2x^2}{\omega_x^2(z)}\right) \exp\left(-\frac{2y^2}{\omega_y^2(z)}\right), \tag{3.6}$$

where

$$\omega_i(z) = \omega_{0,i}\sqrt{1+\left(\frac{z}{z_{R,i}}\right)^2} \qquad i \in x,y \tag{3.7}$$

are the transverse beam radii and $z_{R,i} = \omega_{0,i}^2\pi/\lambda$ are the Rayleigh lengths. The Gaussian intensity profile at the focus position ($z = 0$) can be approximated by using a Taylor expansion, which leads to a harmonic potential

$$U_{dip}(x,y,z) \approx U_0 \left(1 - \left(\frac{x}{\omega_{0,x}}\right)^2 - \left(\frac{y}{\omega_{0,y}}\right)^2 - \left(\frac{z}{z_R}\right)^2\right), \tag{3.8}$$

---

[1] The complex polarizability depends on the internal atomic state and the frequency of the driving electromagnetic field.

where

$$U_0 = -\frac{\mathcal{R}(\alpha)P}{\varepsilon_0 c \pi \omega_{0,x} \omega_{0,y}} \tag{3.9}$$

is the depth of the optical dipole potential. For $\mathcal{R}(\alpha) > 0$, atoms experience a force that attracts them to the center of the trap, where the intensity is the largest. Comparing Eq. 3.8 to the model of a classical three-dimensional harmonic oscillator with mass m

$$U_{HO} = \sum_i \frac{1}{2} m \omega_i^2 x_i^2 \qquad i \in x,y,z \ , \tag{3.10}$$

the corresponding trapping frequencies can be approximated by

$$\begin{aligned} \omega_i &= \sqrt{-\frac{2U_0}{m\omega_{0,i}^2}} \qquad i \in x,y \\ \omega_z &= \sqrt{-\frac{2U_0}{m z_R^2}} . \end{aligned} \tag{3.11}$$

While the trap depth scales linearly with the optical power, the trapping frequencies are proportional to the square root of the power. The trap depth and trapping frequencies are mutually dependent and have a significant influence on the evaporation efficiency.

Optical dipole trap setup

In contrast to the ECDL system, the laser for the dipole trapping and the corresponding optics, together as a whole, are entirely built on the vacuum table (Fig. 3.15). The reason for this is that in addition to frequency and intensity stability, the spatial stability of the beams must also be guaranteed, since the BEC is very sensitive to shifts in the trapping beam positions. Thus, the setup is intended to keep the optical paths as short as possible. The optical paths could be even made shorter with optical fibers, but this is technically limited by the high power dipole laser. The height of all optical components ensures that the beams are aligned to the center of the science chamber and lie in the same horizontal plane. The laser emission starts with a beam in the TEM_{00} mode and a $225\,\mu$m waist located 2.5 cm inside the laser head. The beam quality is affected by the injection current of the laser diodes and deteriorates for very low current values. Therefore the laser is operated at full power. The total power for the operation and alignment of the dipole trap can be adjusted by two successive polarizing beam splitters in conjunction with $\lambda/2$-wave plates. This is particularly important for low power alignment purposes, because decreasing all the power with only one of the beam splitters leaves a residual polarization component behind that exhibits a low quality spatial mode profile. The remaining reflected power is directed to water cooled anodized beam dumps. A cone inside the hollow cylinders diffracts the beam and distributes the power over the internal surface, where it is dissipated. After the total power adjustment, the beam traverses an optical isolator and is collimated by two lenses to a beam waist of 2.3 mm. After that, the beam is split up into two paths, where

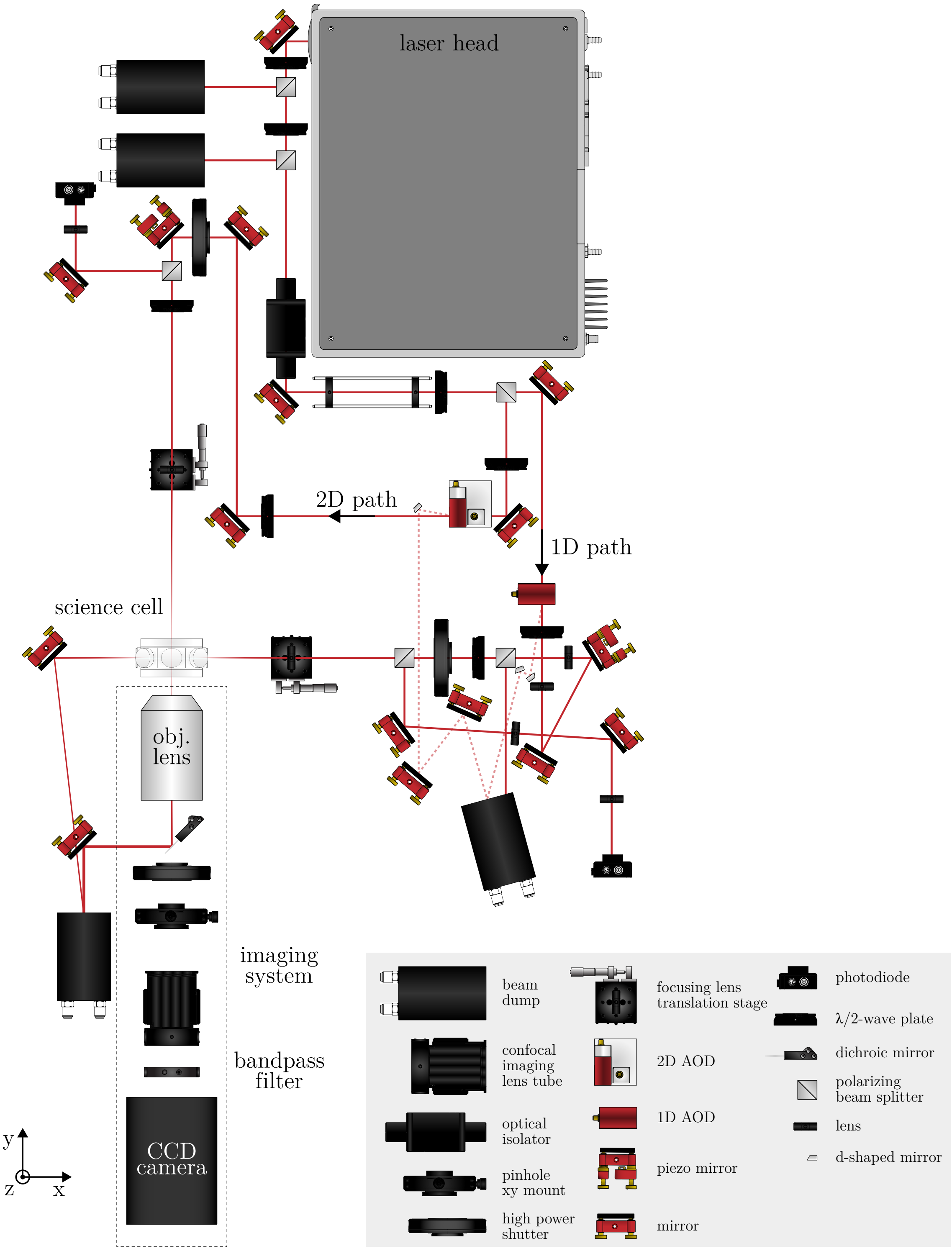
laser head
2D path
1D path
science cell
obj. lens
imaging system
bandpass filter
CCD camera
y
z
x
beam dump
focusing lens translation stage
photodiode
λ/2-wave plate
confocal imaging lens tube
2D AOD
dichroic mirror
polarizing beam splitter
optical isolator
1D AOD
lens
d-shaped mirror
pinhole xy mount
piezo mirror
high power shutter
mirror

Figure 3.15: Optical dipole trap setup. Layout of the setup for the crossed optical dipole trap. The initial laser beam is split up into two paths, which pass through a 1D and 2D AOD, respectively. After splitting, both beams are focused down into the center of the science chamber and cross each other at 90°.

the transmitted and reflected beams pass through a one-dimensional (AA Opto-Electronic, DTSX-400) and a two-dimensional (AA Opto-Electronic, DTSXY-400) acousto-optical deflector (AOD), respectively. Both paths are referred to as the x and y beam paths. The AODs consist of TeO_2 crystals, with their optical axis aligned, such that the first order output beams are parallel to the input beams. Two $\lambda/2$-wave plates in front of the AODs adjust the polarizations of the beams in order to maximize the efficiencies in the first-order beams. In total, three direct digital synthesis (DDS) devices with a center frequency of 75MHz in combination with 2 W power amplifiers are used to drive the AODs. The bandwidth of the AODs is 30 MHz, which corresponds to a full deflection angle of 2.8°. The main feature of the AODs is to spatially and temporally deflect the beams by frequency modulation of the corresponding radio-frequency input signals. In this way, painted (i.e. time-averaged) potentials at the position of the atoms can be created. However, at the current stage of the experiment, the AODs are driven with static frequencies for creating a static cODT. Besides deflection of the beams, the AODs are also used to stabilize the power of the two beams. A small fraction of the power is sent to a photodiode by a $\lambda/2$-wave plate and a polarizing beam splitter. The photodiode voltage is fed into a PID controller as an input signal, where the output signal regulates the radio-frequency power for the AODs via a (MiniCircuits, ZX73-2500-S+) voltage-controlled attenuator (VCA). After passing through the AODs, the beams are first expanded by two lenses and then focused down by another lens to the center of the science chamber, where the beam waists are approximately $35\,\mu$m and $70\,\mu$m respectively. The last directing mirrors are mounted on piezo-electric mirror mounts, in order to have precise control over the beam positions. After passing through the science chamber, the high-power beams are directed by dichroic mirrors to an additional beam dump.

Loading into the crossed-beam optical dipole trap

The tight confinement of the quadrupole trap helps to efficiently load the atomic ensemble into the small crossed optical dipole trap. The transfer of the atomic cloud is established by an adiabatic transformation of the linear quadrupole potential, which is illustrated in Fig. 3.16 (b,c). The two crossed optical dipole beams are focused to few tens of microns below the center of the magnetic quadrupole trap, thereby forming a combined hybrid potential [63]. This kind of potential is also known as a "dimple" trap, which has been theoretically characterized [123, 85] and also demonstrated for different trapping geometries [124–126]. The phase space density increases by the adiabatic transformation of the trapping potential, in contrast to an adiabatic compression of an unchanged trapping configuration [120]. By ramping down the quadrupole trap, atoms start accumulating in the dipole potential by falling down due to gravity. The gravitation effectively reduces the trap depth of the dipole trap, but it can be compensated by a magnetic field gradient of 15 G/cm. The corresponding ramps, which are used in the experimental sequence are shown in Fig. 3.17. The loading into the cODT begins with linearly ramping up the power of the dipole beams to their maximum values of 6.5 W and 0.6 W within 200 ms. The transfer is completed by subsequently ramping down the quadrupole magnetic field gradient from 169 G/cm to zero in another additional 200 ms. During the transfer a small homogeneous

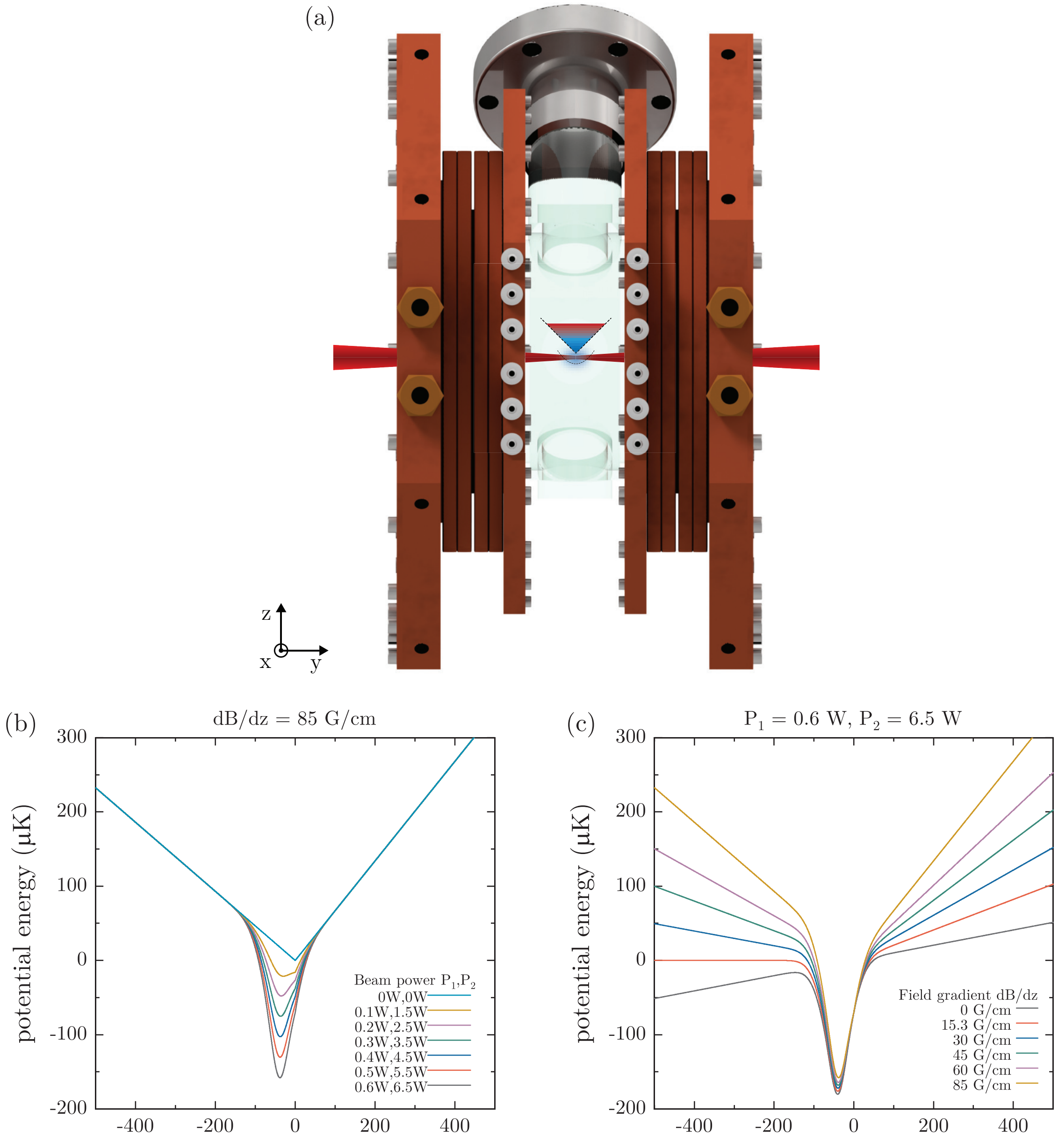

Figure 3.16: cODT loading. (a) The front-view schematic representation of the loading setup shows the cODT, which is focused few microns below the center of the magnetic quadrupole trap. The 1D beam pointing perpendicular to the yz-plane is not illustrated. The linear quadrupole potential is adiabatically transformed into the harmonic optical dipole potential by (b) first ramping up the optical dipole power and (c) subsequent ramp down of the magnetic field gradient. The gravitational potential is compensated for a magnetic field gradient of 15.3 G/cm. The gravitational potential points along the negative z-axis.

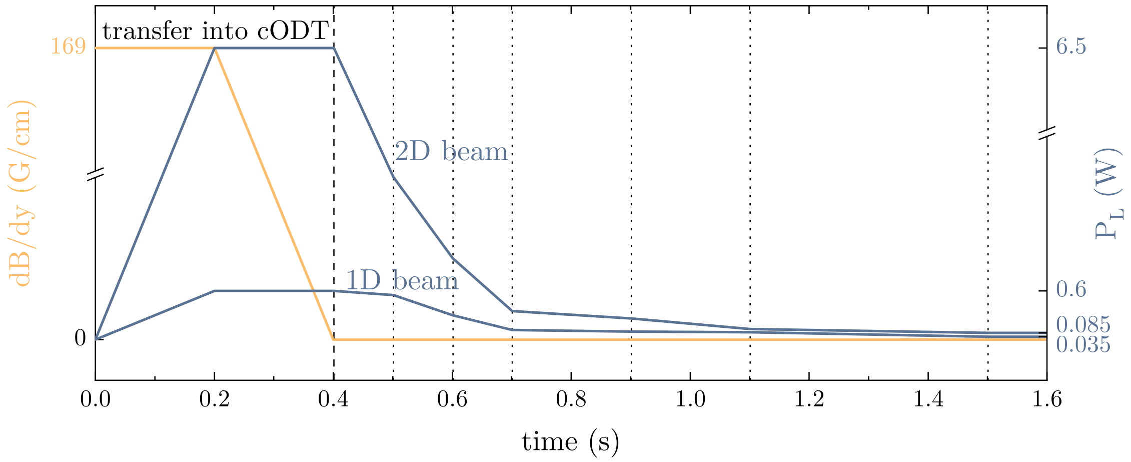

Figure 3.17: Ramp profiles during the transfer and evaporation in the cODT. The transfer into the cODT is established within 400 ms by first ramping up the optical power of the two beams and subsequently ramping down the magnetic field gradient from 169 G/cm to zero. The evaporation within the cODT is divided into six steps and takes in total 1.2 s.

magnetic field is applied, which serves as a quantization axis for the spins, otherwise they would be distributed in all states. However, the bias field also leads to a shift of the QPT minimum shifts when the QPT coils are switched off.

Evaporation in the crossed-beam optical dipole trap

The evaporation in the harmonic potential of an optical dipole potential is schematically shown in Fig. 3.18. After the loading of the cODT, the evaporation is initiated by gradually decreasing the optical power of the two corresponding laser beams. The evaporation sequence is divided into six linear ramps and has a total duration of 1.2 s. The corresponding

Table 3.2: cODT evaporation ramp parameters. The ramps start with the end frequency of the corresponding previous ramp.

ramp no.	duration (ms)	(1D) start power (W)	(1D) stop power (W)	(2D) start power (W)	(2D) stop power (W)
1	100	0.6	0.55	6.5	2
2	100	0.55	0.3	2	1
3	100	0.3	0.12	1	0.35
4	200	0.12	0.1	0.35	0.26
5	200	0.1	0.09	0.26	0.13
6	400	0.09	0.035	0.13	0.085

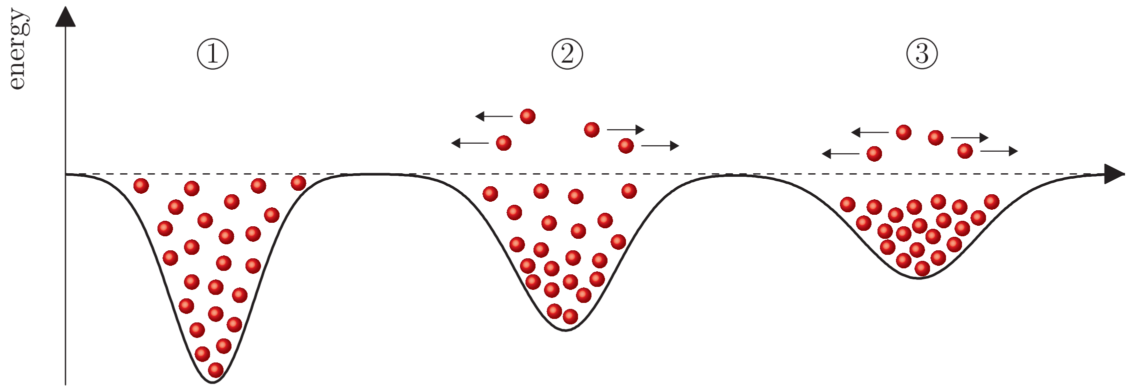

Figure 3.18: Evaporation in a harmonic optical dipole potential. The schematic diagram shows the evaporative cooling process inside a harmonic dipole potential, where high energetic atoms are deliberately ejected from the trap by successively lowering the optical power, resulting in a shallow trap depth and lower trap frequencies (1-3).

powers and timings for each evaporation step are summarized in Table 3.2. The final powers of the 1D and 2D beams are 35 mW and 85 mW, respectively. After the last ramp, the atoms are held for an additional 100 ms in the trap, such that the evaporation dynamics settle down until the atoms thermalize and are fully condensed.

3.2.6 Evaporation efficiency

A crucial figure of merit for the efficiency of the employed evaporation schemes described in the previous sections, is characterized by the gain in phase space density after each corresponding evaporation step. The phase space density is generally given by

$$\mathcal{D} = \lambda_{dB}^3 n_0 \quad \text{with} \quad \lambda_{dB} = \sqrt{\frac{2\pi\hbar^2}{M k_B T}}, \tag{3.12}$$

where λ_{dB} is the de Broglie wavelength, n_0 is the peak density, $\hbar$ is the Planck constant and M is the mass of the rubidium atom. For the quadrupole trap, the atomic peak density n_0 can be calculated by means of the measured total atom number N, temperature T and the magnetic field gradient dB/dx as [127]

$$n_0 = \frac{N}{32\pi}\left(\frac{\mu_B dB/dx}{k_B T}\right)^3. \tag{3.13}$$

For the crossed optical dipole trap the phase space density is given as

$$\mathcal{D} = N\left(\frac{\hbar\bar{\omega}}{k_B T}\right), \tag{3.14}$$

where $\bar{\omega}$ is the mean angular trapping frequency. In order to estimate the phase space density, the trapping frequencies ν_x, ν_y and ν_z need to be determined. By abruptly changing

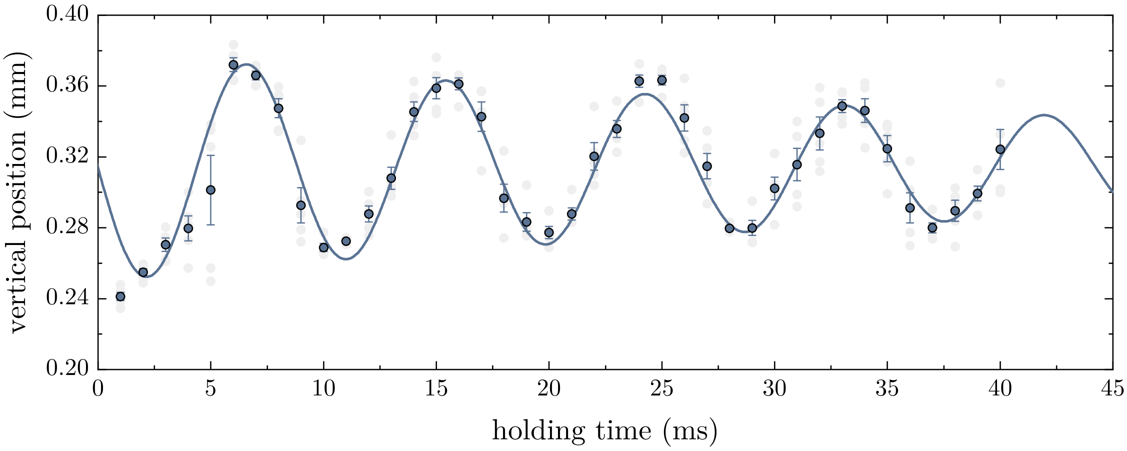

Figure 3.19: Vertical trapping frequency of the cODT. The oscillation of the center of mass position after a constant free fall time and recapture is shown as a function of the holding time. The damped sinusoidal fit gives a mean vertical trapping frequency of $\omega_z = 2\pi \times 114\,\mathrm{Hz}$.

the optical potential the atomic cloud can be excited, which causes an oscillatory motion of its center of mass position. Alternatively, all three trapping frequencies $\boldsymbol{\omega} = 2\pi \times \left[\nu_x,\nu_y,\nu_z\right]$ can be calculated by solving a three-dimensional Eigenvalue equation

$$\nabla\nabla^T U(\boldsymbol{r},\omega_{0,x},\omega_{0,y},P_x,P_y) - \boldsymbol{\omega}^2\mathbb{1} = 0 \tag{3.15}$$

for the harmonic potential U as a function of the beam waists $\omega_{0,x},\omega_{0,y}$ and corresponding beam powers P_x,P_y generated by the two Gaussian beams including the gravitational potential. Here, only the vertical trap frequency is measured as a reference and as a validity check for the estimated beam waists. The vertical trap frequency is measured by turning off the cODT for $500\,\mu$s and subsequently recapturing the free falling atoms again. The atomic cloud's center position is detected after a variable holding time from 1 ms to 40 ms, which is shown in Fig. 3.19. The sinusoidal fit to the measured data points yields a vertical trapping frequency of $\omega_z = 2\pi \times 114\,\mathrm{Hz}$, which fits very well to the calculated value of $\omega_z = 2\pi \times 118\,\mathrm{Hz}$ for the estimated beam waists of $\omega_{0,x} = 35\,\mu$m, $\omega_{0,y} = 70\,\mu$m and corresponding beam powers of $P_x = 0.085\,\mathrm{W}$, $P_y = 0.035\,\mathrm{W}$.

The phase space trajectory for the full evaporation ramp is plotted in Fig. 3.20. The gain in phase space density is given by

$$\eta = -\frac{d\log\mathcal{D}}{d\log N}, \tag{3.16}$$

which is $\eta = 1.74(9)$ for the current evaporation trajectory. For a good evaporation efficiency it is typical that the phase space density increases by about three orders of magnitude, while atoms are lost by one order of magnitude. Improving for a higher efficiency is certainly possible by adjusting the speed or the profiles of the corresponding evaporation ramps, but

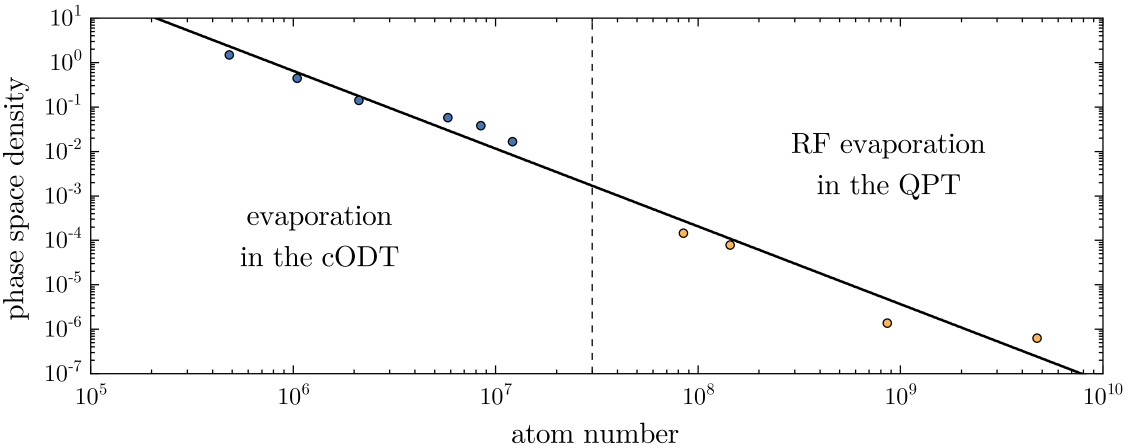

Figure 3.20: Phase space density. The colored data points show the phase space densities in the QPT (orange) and cODT (blue) as a function of the atom number. The first data point reflects the phase space density after loading into the QPT. The following data points represent the phase space densities at the end of the subsequent RF and power ramps. The last data point corresponds to the BEC threshold. The phase space density was calculated by evaluating the corresponding density profiles of fluorescence images for different free fall times. Each data point was taken after a thermalization time of 100 ms. The slope of the fitted solid line gives an overall evaporation efficiency of $\eta = 1.74(9)$.

at the same time, comes with the expense of a prolonged cycle time. Instead, here the evaporation scheme is intended to be optimized on the overall speed performance of the apparatus, while delivering a reasonable number of condensed atoms in the BEC.

3.2.7 BEC characterization

The BEC phase transition can be observed by investigating the spatial mode profile of the atomic cloud along the evaporation path given in Table 3.2. The characteristic feature of the BEC phase transition is the formation of a bimodal distribution of the atomic density profile at the critical temperature T_C. The condensate fraction follows a Thomas-Fermi distribution and overlaps with the thermal background distribution, which is typically characterized by a Gaussian mode profile. To study the transition, the last evaporation ramp in Table 3.2 is subdivided into five parts, where the time is tuned from 0 ms to 400 ms in steps of 100 ms. The corresponding final 1D and 2D beam powers are listed in Table 3.3. The temporal evolution of the atomic cloud size and shape is recorded with fluorescence images that are taken after each consecutive evaporation step near the condensation threshold and is illustrated in Fig. 3.21 (a). The images are taken for different times of flight in order to let the cloud expand and to be able to discriminate the condensate fraction from the thermal background atoms. With each evaporation step, the size of the atomic cloud gradually decreases. At the end of the evaporation, the size of the cloud shrinks to ~100 μm after 15 ms of free expansion time. Furthermore, there is a reduction of the

Table 3.3: cODT evaporation parameters of the last evaporation step.

ramp no.	duration (ms)	(1D) start power (W)	(1D) stop power (W)	(2D) start power (W)	(2D) stop power (W)
6.0	0	0.09	0.09	0.13	0.13
6.1	100	0.09	0.076	0.13	0.119
6.2	200	0.09	0.063	0.13	0.108
6.3	300	0.09	0.049	0.13	0.096
6.4	400	0.09	0.035	0.13	0.085

thermal background accompanied with a change in the aspect ratio compared to the in-trap profile. The horizontal width of the atomic cloud is narrower than in the vertical direction, since the horizontal 1D beam has a tighter focus than the 2D beam, which is pointing out of the image plane. The last image after 15 ms time of flight also shows a tilt of $\sim 5°$ of the principle axis of the atomic cloud with respect to the horizontal and vertical imaging axes. This might be caused by a slight misalignment of the 1D beam. A more quantitative analysis is given by the one-dimensional integrated line profiles given in Fig. 3.21 (b). The horizontal line profiles are extracted from the pixel sum of the corresponding images for 5 ms, 10 ms and 15 ms time of flight. With the successive expansion of the atomic cloud size, there is a dispersion of the line profiles and an overall reduction of the peak atom number density. The evaporation steps lead to a successively narrower width of the line profiles. The onset of two different spatial distributions can be discriminated best after 10 ms or 15 ms free fall times. The narrow line profile is more pronounced in the horizontal direction, which is indicating a tighter confinement and larger trap depth in this direction. The transverse profiles can be evaluated by exploiting a bimodal Thomas-Fermi Gauss model. For this, the horizontal line profiles with 15 ms time of flight are fitted with the one-dimensional density function

$$\begin{aligned} n_{1D}(x) = n_{0,TF} &\left[\frac{1}{2} \times \left(1 - \left(\frac{x - x_{0,TF}}{\sigma_{TF}}\right)^2\right) \times \left(\mathrm{sign}\left[1 - \left(\frac{x - x_{0,TF}}{\sigma_{TF}}\right)^2\right] + 1\right)\right]^2 \\ &+ n_{0,G} \exp\left(-\frac{(x - x_{0,G})^2}{2\sigma_G^2}\right) + n_0, \end{aligned} \tag{3.17}$$

where n_0 is the background level offset, $n_{0,TF}$,$n_{0,G}$ are the amplitudes, σ_{TF},σ_G are the widths and $x_{0,TF}$,$x_{0,G}$ are horizontal offsets of the corresponding Thomas-Fermi and Gauss distributions. The fitted results of the line profiles are plotted in Fig. 3.22 (a-e). After 200 ms of evaporation, the onset of a BEC phase transition can be witnessed. With increasing evaporation time, the spectral weight shifts from a Gaussian to an emerging parabolic density profile and hints at the macroscopic occupation of the ground state. After the final evaporation step, a BEC with $\sim 10^5$ atoms with a minimal thermal fraction is left. However, in this simple fitting procedure the temperature for the last step is

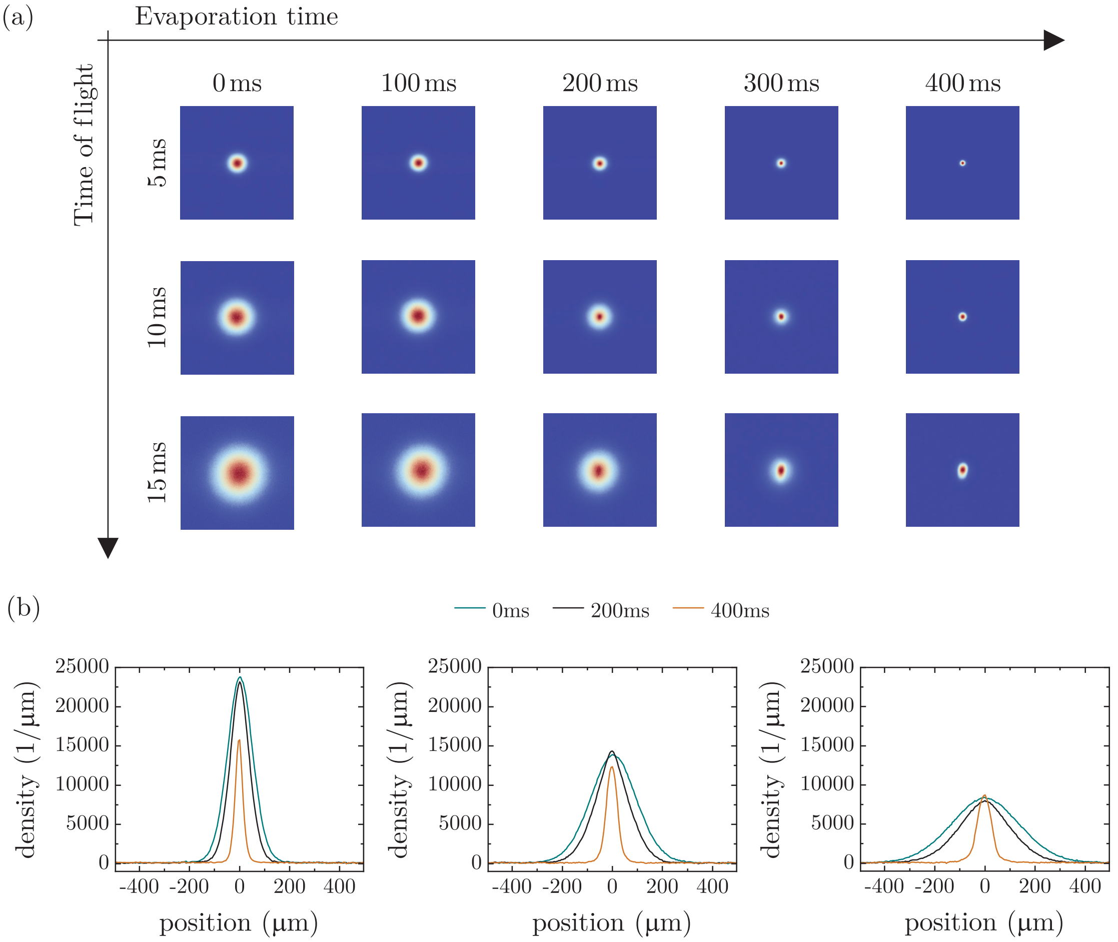

Figure 3.21: Sequential time evolution of the atomic cloud size and shape. (a) A series of fluorescence images are recorded for the different evaporation steps and times of flight. The image sizes are 100×100 pixels, where the image scaling is $4.96\,\mu$m/pixel. The atomic cloud is broadening during free fall, as a consequence of the initial velocity distribution. This broadening significantly reduces with increasing evaporation time. (b) The one-dimensional line profiles for 5 ms, 10 ms and 15 ms time of flight are extracted by integrating the corresponding images along each pixel column. The horizontal line profiles visualize the temporal evolution of the atomic cloud size and shape, gradually turning from a Gaussian to a Thomas-Fermi distribution. The change in the density profile can be discriminated best for a free expansion time of 15 ms due to the limited resolution.

underestimated, since the thermal contribution was assumed to be Gaussian in the center of the atomic cloud. It is important to note that due to the repulsive interactions [128] of the condensed atoms in the center of the cloud, the distribution can significantly deviate from a Gaussian distribution and one has to resort to more elaborate fitting algorithms [129, 130]. The evolution of the temperature and atom number during the phase transition can be seen in Fig. 3.23 (b), as a result of the cloud size measurements in Fig. 3.23 (a)

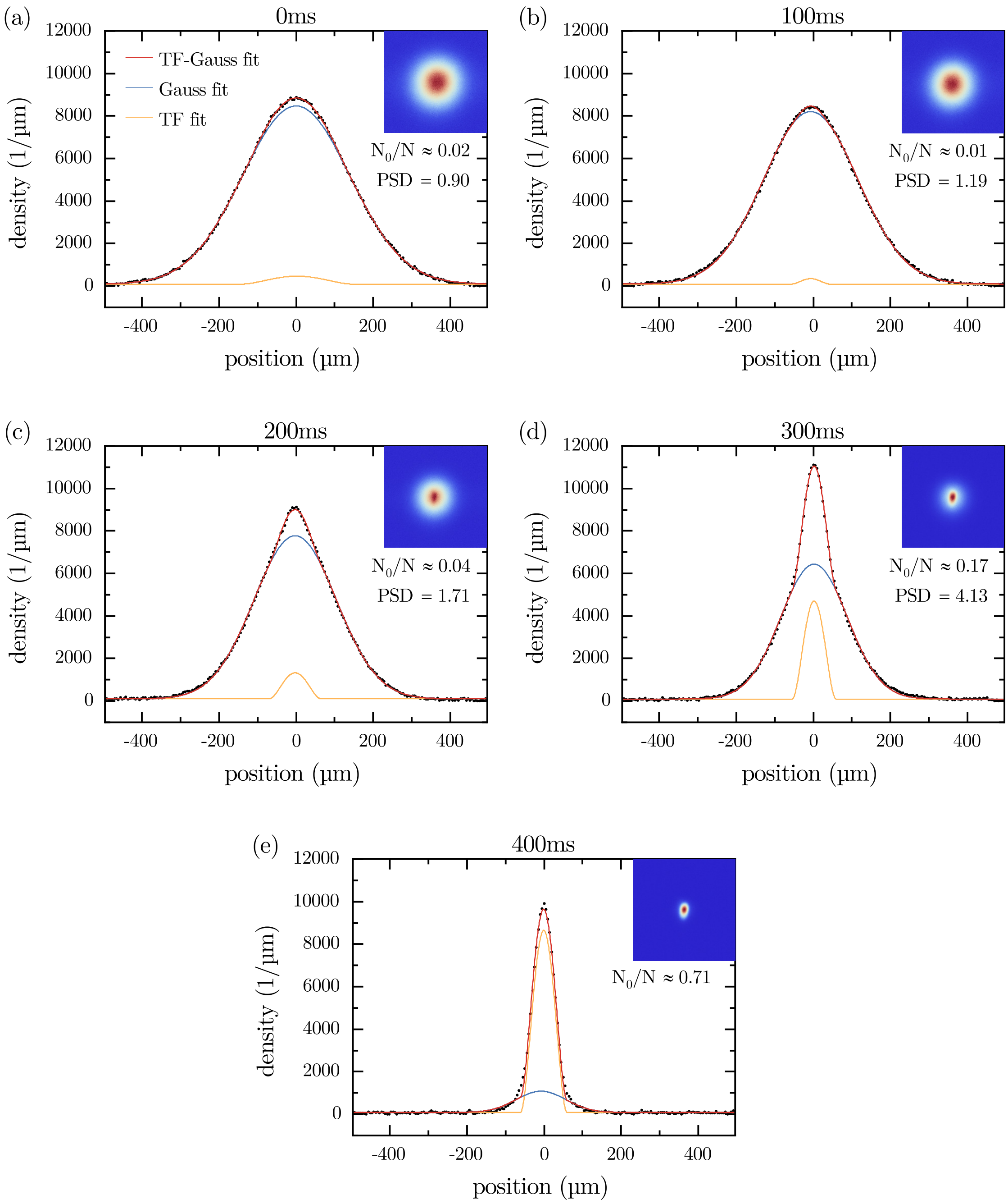

Figure 3.22: Bimodal fits. (a-e) The horizontal line profiles with 15 ms time of flight are plotted for different evaporation steps. The profiles are fitted with a Thomas-Fermi Gauss model according to Eq. 3.17. The solid lines in blue and orange represent the Gaussian and Thomas-Fermi contributions, whereas the solid red line corresponds to the composite fit. The insets show the respective fluorescence images.

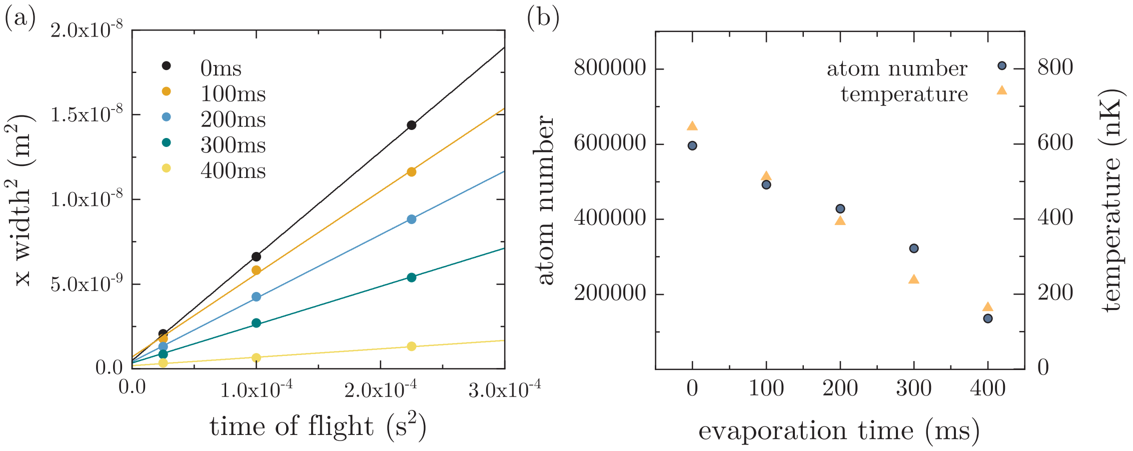

Figure 3.23: Total atom number and temperature measurement. (a) The squared cloud widths are plotted against squared times of flight. The widths are extracted by Thomas-Fermi Gauss fits. (b) Total atom number and temperature after different evaporation steps.

and the integrated atom numbers of the horizontal line profiles in Fig. 3.22 (a-e). The atom number as well as the temperature decrease linearly with the evaporation time.

In addition to the bimodal fits, the formation of a BEC is visualized by means of the fraction of condensed atoms N_0/N at different temperatures, which are extracted from the thermal background. Fig. 3.24 (a) shows the atom number in the BEC as a function of the temperature corresponding to different evaporation steps. The data points are normalized with respect to the calculated critical temperature

$$T_C = \frac{\hbar\bar{\omega}}{k_B}\left(\frac{N}{\zeta(3)}\right) = 243\,\mathrm{nK}. \tag{3.18}$$

The solid black line represents the expected behaviour of the order parameter for the calculated critical temperature in the thermodynamic limit

$$\frac{N_0}{N} = 1 - \left(\frac{T}{T_C}\right)^3. \tag{3.19}$$

Fig. 3.24 (b) shows the threshold for the BEC phase transition in terms of the phase space density. The classical limit for an ideal Bose gas is crossed between the third and fourth evaporation step, as indicated by the order parameter plot. Above the threshold, the bimodal fits fail to give reasonable results for the phase space density.

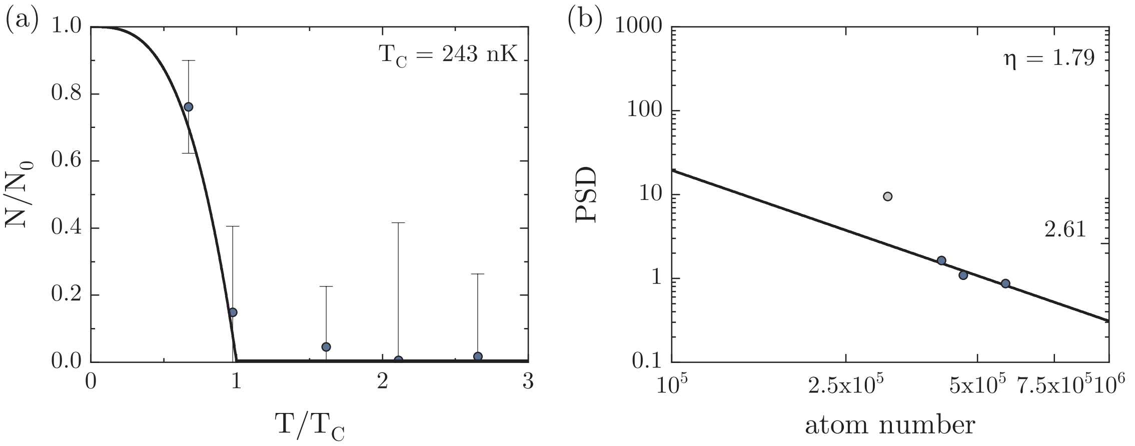

Figure 3.24: BEC fraction and PSD. (a) The fraction of the condensed atoms is plotted as a function of the normalized temperature T_C. (b) The classical phase space density is shown in the vicinity of the phase transition. The evaporation efficiency is determined by a linear fit of the first three data points (blue).

CHAPTER 4

Preparation of number-stabilized atomic ensembles

This chapter describes the deterministic preparation of atoms inside a MOT by means of a feedback control system. In most ultracold atom experiments, the preparation of mesoscopic atom numbers is guided by processes that are inherently of probabilistic nature. The final prepared atom number typically depends on a number of stochastic loading or loss rates that occur over the course of the experiment. These are typically caused by the (re-)loading and holding times of atoms in trapping potentials, due to limited lifetimes or by evaporative cooling processes as a result of elastic and inelastic collisions with finite probabilities. As a consequence, the atom number is determined only as a mean value with a corresponding standard deviation. Drifts and variations in the prepared atom number can be transmitted through the subsequent experimental sequence and manifest themselves in the corresponding measurement results as statistical noise. Therefore, the motivation is to reduce the impact of initial number fluctuations onto the preparation fidelity. This is demonstrated by stabilizing the initial atom number in a MOT using a feedback loop. The stabilization scheme involves a detection system, which is capable of distinguishing the signal of atomic ensembles with different numbers.

This chapter is divided into two sections. The first section deals with the single-particle detection system that has been implemented and optimized by the work of the PhD thesis from Ref. [88]. The results of that PhD thesis are used to explain its working principle and properties. The second section, as a main result of my thesis, demonstrates the successful stabilization of 7 atoms with the underlying detection system. The last part presents a next-generation detection setup based on optical fibers, which is built to improve the single-atom-resolution limit.

4.1 Fluorescence detection of individual atoms in a MOT

The detection of ultracold atomic ensembles by fluorescence imaging is typically accomplished by illuminating a free-falling atom cloud with quasi-resonant light. The atoms will absorb the incident photons and re-emit them isotropically. A fraction of this fluorescence signal is usually detected on a photodiode or CCD camera detector. The amount of collected photons of the fluorescence signal depends on the intensity and frequency detuning of the laser light, the covered solid angle of the detection system and the quantum efficiency of the camera. In order to infer the number of atoms for the fluorescence fluorescence signal, the signal of an individual atom needs to be precisely determined. Thus, the accurate detection of the atom number is equivalent to an accurate counting of the scattered photons. Once the photon counts of a single atom are calibrated, the number of atoms of the cloud can be estimated by dividing the collected total number of photon counts by the counts corresponding to the signal of the single atom. However, for a freely falling atom cloud the illumination time is generally limited to only a few tens of microseconds, because of the acceleration and dilution induced by the strong light pressure. Much longer interrogation times can be achieved by imaging atoms inside a trap, which can be realized, for example, by far red-detuned optical lattices, dipole traps or MOTs. MOTs turn out to be particularly suitable environments, since they can provide long lifetimes of up to hundreds of seconds and simultaneously cool the atoms during the detection time. As a consequence, the corresponding signal-to-noise ratio can be greatly enhanced. In the following sections, the detection system that enables the counting of single atoms is described.

4.1.1 Fluorescence image acquisition

In order to characterize the detection system, a series of fluorescence images of a MOT that contains a small amount of trapped ^{87}Rb atoms are recorded. The small sized MOT is produced by the detection configuration previously described in Section 3.1.3. The images are taken during the holding time of the atoms within the MOT by continuously exposing the CCD camera to the scattered fluorescence light of the atomic cloud. The amount of the collected light corresponds to a fraction ($\approx 5\%$) of the full solid angle, which is covered by the objective lens system described in Section 2.6. The detected photons impinging on the CCD camera chip are then converted into digital photoelectron counts. After the readout of the sensor array with a resolution of 1024×1024 pixels, a false-color image is produced and processed by the evaluation software. Fig. 4.1 shows an example for the acquisition of the fluorescence signal of a single atom, which is evaluated within a region of interest. Two images are taken in order to extract the atomic fluorescence signal. The actual atom image is corrected by subtracting a background picture, which only contains stray light originating from other ambient sources.

4.1.2 Atom number estimation

To determine the number of atoms within the MOT, apart from a background offset, the fluorescence signal of a single atom is the defining factor that scales the number of atoms with respect to the detected camera counts. The fluorescence signal of a single atom, which is excited by a quasi-resonant, low-intensity laser light is described by the scattering rate formula

$$R_{sc}(\mathit{\Delta},S_0) = \frac{\mathit{\Gamma}}{2} \frac{S_0}{1 + S_0 + 4(\mathit{\Delta}/\mathit{\Gamma})^2}, \tag{4.1}$$

where $S_0 = I/I_S$ is the saturation parameter given by the ratio of the laser intensity I and the saturation intensity I_S. The MOT is operated with a detuning of $\mathit{\Delta} = 2\pi \times 6\,\mathrm{MHz}$ and a

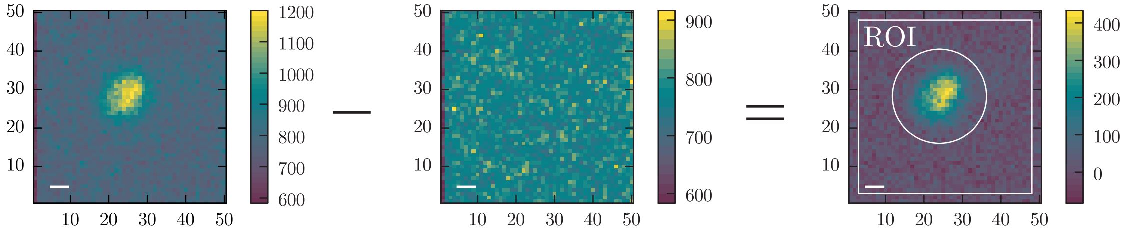

Figure 4.1: Fluorescence image acquisition. The size of the recorded images is 50×50 pixels, where each pixel is binned by 2×2. The color bars show the respective digital counts in the image. The white scale bar measures the length of 5 pixels (i.e. 10 physical pixels on the CCD camera chip), which corresponds to $49.6\,\mu$m in the object plane. Left: Example of a fluorescence image of an atom trapped in the MOT. Center: A background image is recorded prior to the atom image, in order to extract only the photoelectron counts originating from the atom signal. Right: The resulting background subtracted image of the atom is evaluated within a region of interest, which excludes edge artifacts due to shifting and readout of pixels.

saturation parameter of $S_0 = 6.65$. Since only a fraction of the isotropically scattered light is collected by the maximum numerical aperture (see Section 2.6), the signal is weighted by the detection efficiency

$$\eta = \frac{\varOmega \times QE \times T}{g} = 4.33\% \tag{4.2}$$

of the imaging system, which also includes other technical parameters, such as the overall transmission coefficient T of the detecting lens and glass cell surfaces, the quantum efficiency QE of the camera and the photoelectron conversion gain factor g. The expected counts per atom per second is therefore given as

$$r_{cts} = \eta \times R_{sc}(\varDelta, S_0) \approx 474\,\text{kcts/(s atom)} \tag{4.3}$$

For a finite detection time of $t_{det} = 90\,$ms the expected scale factor reads

$$n_{cts} = r_{cts} \times t_{det} \approx 43\,\text{kcts/atom}. \tag{4.4}$$

Dividing the total integrated count signal of the pixels in the region of interest by the scale factor allows to estimate the detected atom number.

4.1.3 Characterization and calibration of the detection system

The resolution of the detection system is characterized by its capability to detect the atom number with a small number noise. In order to calibrate the atom number scaling, sufficient statistics on the detected count levels need to be gathered. For this reason, a time trace measurement of a series of fluorescence images is recorded and shown in Fig. 4.2. The procedure for image acquisition is similar to that shown in Fig. 4.1. First, a background image is recorded to reduce any stray light contributions to the atomic signal. Therefore,

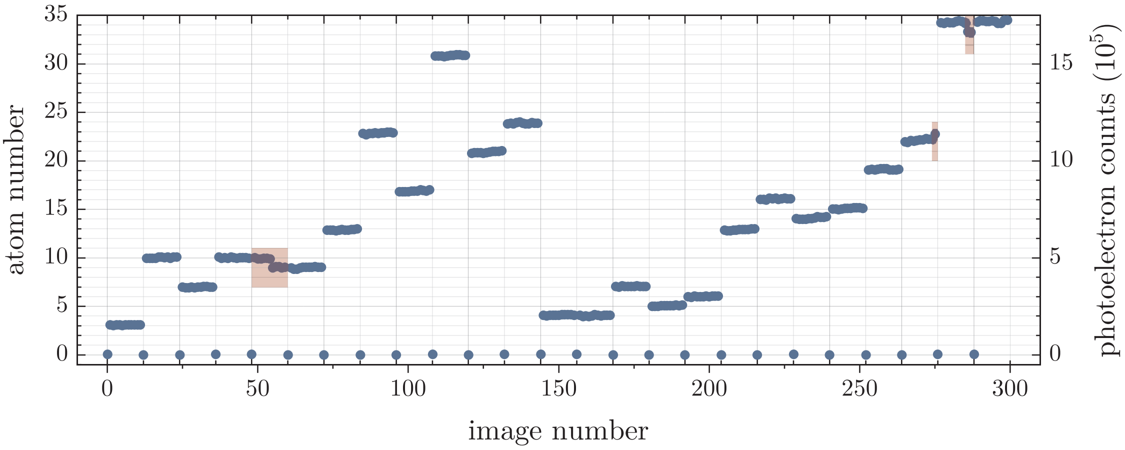

Figure 4.2: Time trace of detected atom numbers. A series of 300 out of more than 5200 total images depict the fluorescence levels in terms of atom numbers (left) and photoelectron counts (right). The time trace measurement consists of 25 repetitions marked by the vertical gridlines. The horizontal gridlines represent the corresponding integer atom numbers. Each repetition consists of an initial background image followed by 11 images that contain the fluorescence signal of the atoms. The shaded areas indicate example loss and loading events that occured between two subsequent images. Adapted and reevaluated from Ref. [88].

during the background acquisition, solely the scattered light from the MOT beams is imaged. Following this, the large volume 3D-MOT is loaded from the 2D$^+$-MOT for 15 ms. The large MOT beams are then turned off for 10 ms, after which the detection MOT recaptures a small fraction of the atoms. An additional holding time of 500 ms inside the detection MOT gets rid of remaining, untrapped atoms that can escape from the detection region. The fluorescence image of the atomic cloud is then recorded for 90 ms. After this time, the image is read out for 220 ms, while the atoms are still trapped in the detection MOT. The last two steps are repeated until a total set of 11 images is captured. The time traces show distinct jumps in steps of integer atom numbers. In some rare cases, there occurs a loss or a single atom loading event during the holding time in the MOT. The frequency of the detected atom numbers can be plotted on a histogram, which is shown in Fig. 4.3. The histogram of the atom number counts is based on more than 5200 recorded images and shows well-resolved peaks up to 30 atoms. A cumulative Gauss fit of the first 20 peaks reveals the center positions of the individual distributions. The center positions scale linearly with the detected photoelectron counts of the camera (Fig. 4.3 inset). The scale factor, which calibrates the detected photoelectron counts with respect to the atom number, is determined by the slope of the linear fit and amounts to 50 kcts/atom.

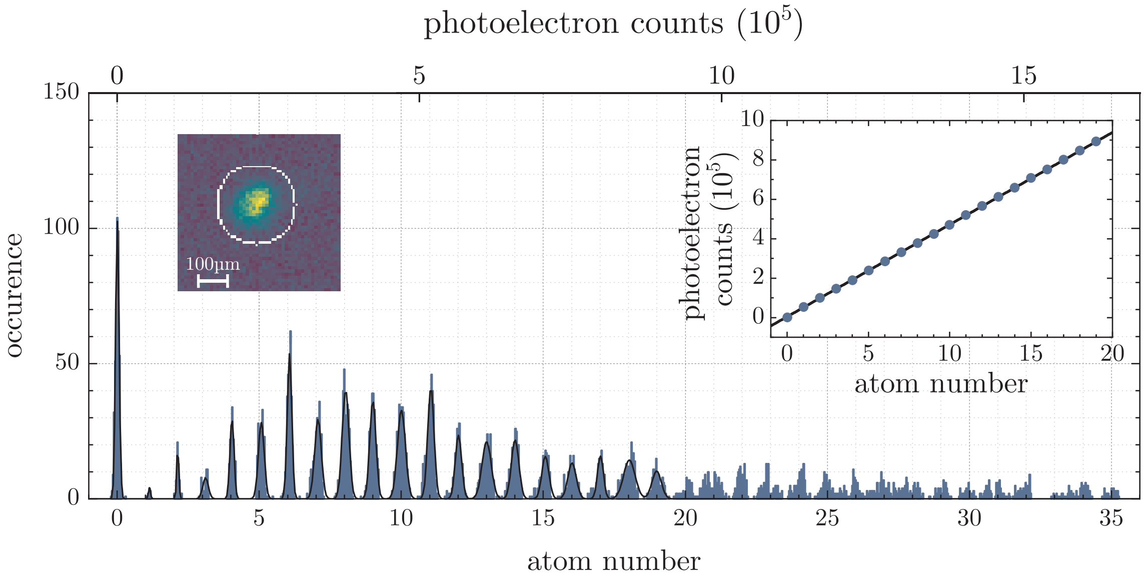

Figure 4.3: Number-resolved single-atom detection. The histogram shows the number of occurrences of the measured atom numbers associated with the recorded 5280 fluorescence images. The histogram data are fitted by a sum of Gaussian distributions. Inset left: Fluorescence image of a single atom. Inset right: The center positions of the Gaussian peaks in terms of photoelectron counts is plotted against the expected atom number showing a linear dependence. From this a scaling factor of 50 kcts/atom can be extracted. Adapted and reevaluated from Ref. [88].

4.1.4 Noise limitations

The counting of individual atoms is in general subject to various sources of noise, which set an upper limit for the maximally resolvable atom number as shown in Fig. 4.3. A measure for the detection noise is provided by the widths and corresponding variances of the individual atom number distributions of the histogram. The single-atom resolution is retained, if the variance of the corresponding distribution is small compared to 1, such that a clear distinction between adjacent atom numbers can be made. In order to have a better understanding of the behavior of detection noise with respect to the resolution, the effects of the individual noise sources on the histogram can be quantified. An apparent contribution comes from the background noise, which stems from the ambient light hitting the CCD camera, the occurence of dark counts, the stray light from the MOT beams and additional offset counts of individual pixels, which add up to the total count signal. Since the background noise is independent of the atom signal, a minimal width is imposed on all other following peaks. The signal and the noise of the background is usually dominated by the signal and noise of the illuminating beams. The noise of the background can therefore be used to estimate the relative noise of the detecting light in terms of the saturation parameter as

$$\sigma_{S_0}^2 = S_0^2 \frac{\sigma_{bg}^2}{\langle N_{bg}^2 \rangle}. \tag{4.5}$$

A second noise source is represented by the photoelectron shot noise

$$\sigma_{psn}^2 = \frac{N}{\eta t_{det} R_{sc}}, \tag{4.6}$$

which results from the finite number of scattered photons. This affects the width of the peak distributions to increase with the square root of the atom number and inherently sets an upper limit to the maximum resolvable atom number. Fluctuations in the scattering rate due to intensity or frequency noise of the cooling beams result in the change of the scaling factor

$$\sigma_{srn}^2 = \frac{\alpha^2}{t_{det}} N^2, \tag{4.7}$$

where

$$\alpha = \sqrt{\tau_{det} \left(\left(\frac{\sigma_\Delta}{R_{sc}} \partial_\Delta R_{sc} \right)^2 + \left(\frac{\sigma_{s_0}}{R_{sc}} \partial_{S_0} R_{sc} \right)^2 \right)} \tag{4.8}$$

defines the frequency and intensity stability parameter. The width scales linearly with the atom number and effectively results in the peaks being washed out. Averaging over longer interrogation times reduces the scattering noise as long as the fluctuations are fast compared to the interrogation time. However, due to a limited MOT lifetime, atom loss is expected to dominate eventually, which is modeled as

$$\sigma_{loss}^2 = \frac{N t_{det}}{2 t_{life}}, \tag{4.9}$$

where t_{life} describes lifetime of the MOT [131, 132]. The resolution in Fig. 4.3 is mainly limited by long term drifts in the intensity and frequency of the cooling MOT beams, which affects the scattering rate and as a consequence the scaling factor. In contrast, short-term fluctuations have been analyzed by employing a two-point variance noise model[1] of consecutively detected atom numbers

$$\sigma_N^2 = \frac{\langle (N_{j+1} - N_j)^2 \rangle}{2} \tag{4.10}$$

that contains the mentioned noise terms

$$\sigma_N^2 = \sigma_{bg}^2 + \sigma_{psn}^2 + \sigma_{srn}^2 + \sigma_{loss}^2 \tag{4.11}$$

An extrapolation of the fitted noise model suggests an upper limit of 390(20) atoms, after which they can no longer be distinguished anymore.

---

[1] The detailed analysis of the noise model can be found in the PhD thesis [88].

4.2 Atom number stabilization in a MOT

The underlying detection system with the capability of single-atom resolution can be used as a tool to prepare atomic ensembles with a defined number. This concept is demonstrated with a MOT, but it can be easily transferred to any other trap. By successive removal of atoms from the MOT a desired target atom number is reached. To this end, a real-time feedback loop is utilized, in which the atom number measurement is interleaved with a dedicated loss process.[1]

4.2.1 Stabilization sequence

The corresponding experimental sequence for the stabilization of 7 atoms is illustrated in Fig. 4.4 (a). The protocol starts with the recording of an initial background image, which is exposed for 90 ms and subtracted later on from the atom images. Next, the detection MOT is loaded from the large volume MOT. The loading time of the large volume MOT is reduced to 20 ms and a subsequent free fall time of 10 ms is employed, before atoms are recaptured and held for 500 ms in the detection MOT. In this way, the loading of an average initial atom number of 15 with a standard deviation of $\sqrt{15} \simeq 4$ atoms is ensured, which is below the single-atom-resolution limit. Following this, a 3 ms loss process is used, which is realized by turning off the repumping light. This increases the probability of atoms being excluded from the cycling transition and makes them transparent to the cooling light, which results in a probabilistic removal from the MOT. An additional 5 ms holding time ensures that the lost atoms have left the detection region. After that, the image acquisition is accomplished with a 90 ms exposure and a 180 ms readout time. At this point, the atom image is evaluated by the CCD camera software on-the-fly. The software checks, if the current, estimated atom number is below the threshold value of 7.5 atoms. The loss process is repeated until the condition is satisfied. Once the measured atom number falls below the threshold, the camera sends a TTL trigger to the FPGA that controls the experiment and stops the loss process. After that, the atoms are imaged four additional times in order to check and verify the stabilized atom number. 16 example time traces out of recorded ones show the successful stabilization for the target number of 7 atoms in Fig. 4.4 (b). Over the course of a stabilization run, the number of atoms in the MOT is successively reduced with a certain probability in steps of integers. The histogram in Fig. 4.5 shows the increasing number of occurences towards the target atom number. It shows that, in most of the cases, the stabilization stops at the desired atom number of 7.

---

[1] This section is published in parts in Ref. [133].

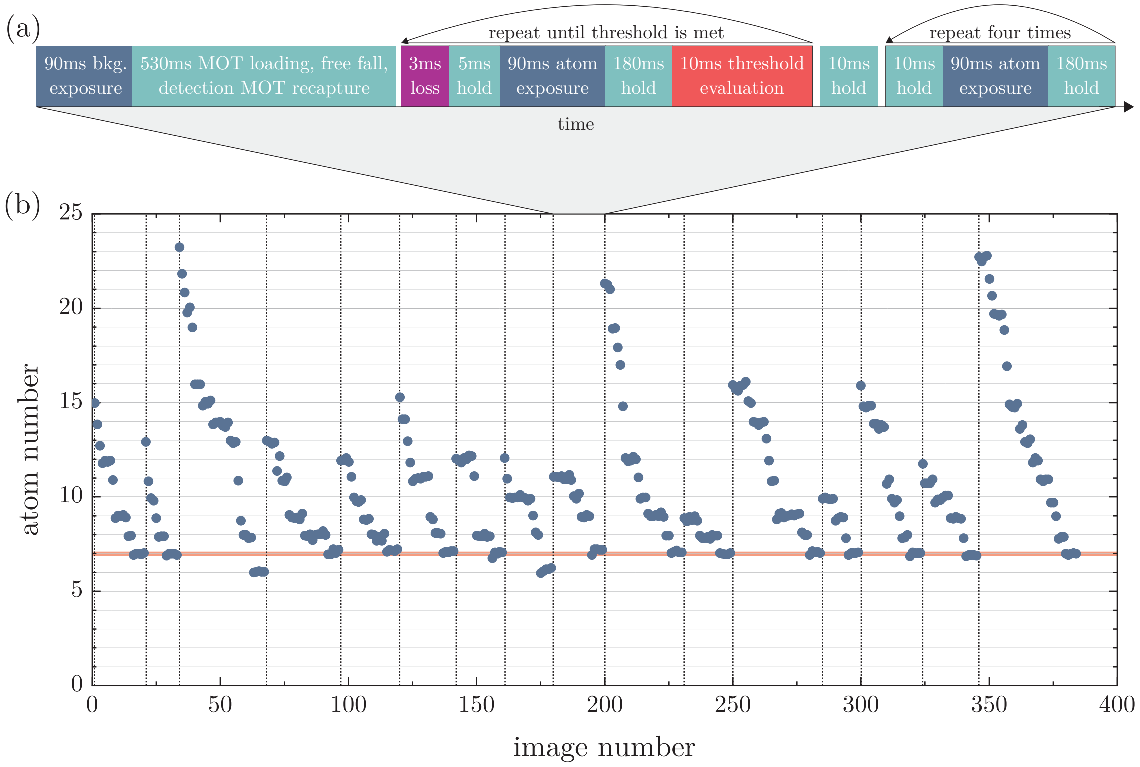

Figure 4.4: Atom number stabilization. (a) Experimental sequence for the atom number stabilization measurement. (b) A number of 16 consecutive time traces that illustrate the successful stabilization of the final atom number, starting with varying initial atom numbers. A new measurement (vertical gray lines) starts, once the target atom number of 7 (red horizontal line) is hit or undercut for five successive images.

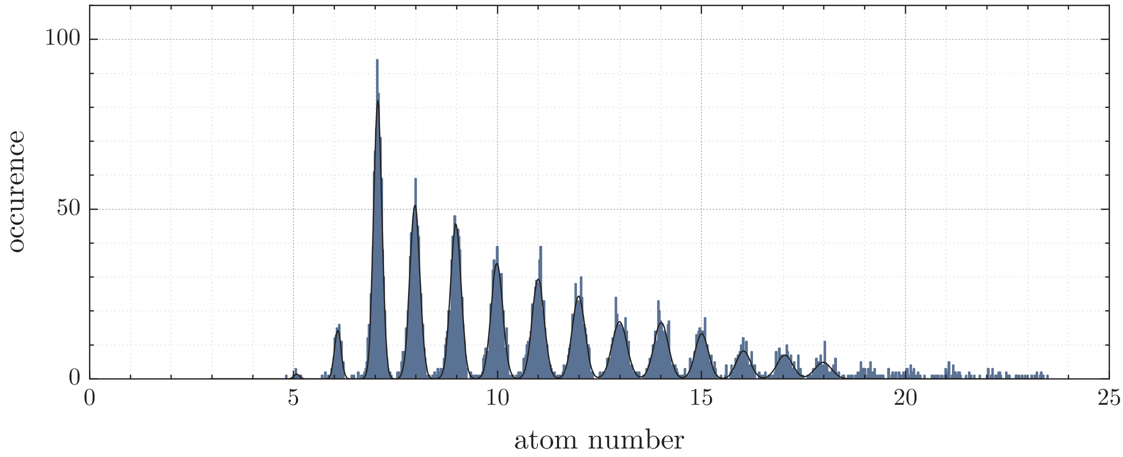

Figure 4.5: Histogram of the detected signal for the total data set of the stabilization run. The histogram is evaluated for a total of 4804 images.

4.2.2 Loss characterization and preparation fidelity

For each loss step, the removal of atoms is associated with a certain probability that determines the precise preparation of the atom number. Due to their indistinguishability, all atoms share an equal and independent survival propability p_s to remain in the MOT. Therefore, each loss step can be treated as a series of Bernoulli trials, which leads to a binomial distribution in the atom number. The histograms in Fig. 4.6 (a-k) show the transition statistics from an initial atom number N_i to a final atom number N_f and illustrate the survival probability after a single loss step. A binomial distribution

$$B(p_s,N_i,N_f) = \binom{N_i}{N_f} p_s^{N_f} (1-p_s)^{N_i-N_f} \tag{4.12}$$

is used to collectively fit all histograms with initial atom numbers ranging from $N_i = 18$ to 8. The fit result reveals a common survival probability of $p_s \approx 96.66\%$, which characterizes the loss step. The accidental removal of two atoms over the course of the last loss step is limiting the fidelity of the target atom number preparation. For the given loss step, the expected fidelity to prepare 7 atoms can be calculated by a truncated binomial distribution centered at 8 atoms, which is 88 %. From this model, a suppression of the number fluctuations by 17.3 dB below shot noise would be expected. Because of the high survival probability, single-step losses from higher atom numbers have a lower probability and contribute less to the obtained results. The final stabilization result is shown in Fig. 4.6 (l). Out of 155 cases, the target atom number 7 is obtained 142 times, which corresponds to a state preparation fidelity of 92 %. In 13 cases, a too small result was obtained (6 atoms: 12 cases, 5 atoms: 1 case). The measured suppression corresponds to 18 dB below shot noise.

The target atom number is reached by an average number of 21 induced loss steps, with an overall loss cycle time of 288 ms. This corresponds to a total preparation time of 6 s. About 63 % of the preparation time is accounted by the readout of the fluorescence image. The preparation speed can in principle be enhanced by operating the camera in a different readout mode. The main fundamental limitation is given by the 90 ms exposure time, which ensures an accurate detection of the atom number. Furthermore, the preparation speed can be improved by dynamically adjusting the loss probability depending on the current atom number in the trap. The preparation fidelity can also be further improved by decreasing the loss probability for a single step as well as increasing the number of steps needed to reach the target atom number.

The control scheme to stabilize the atom number in the MOT can be regarded as a proportional controller, which in some rare cases undershoots the target atom number. A reloading mechanism from the 2D-MOT can be employed to improve the success rate of the stabilization procedure.

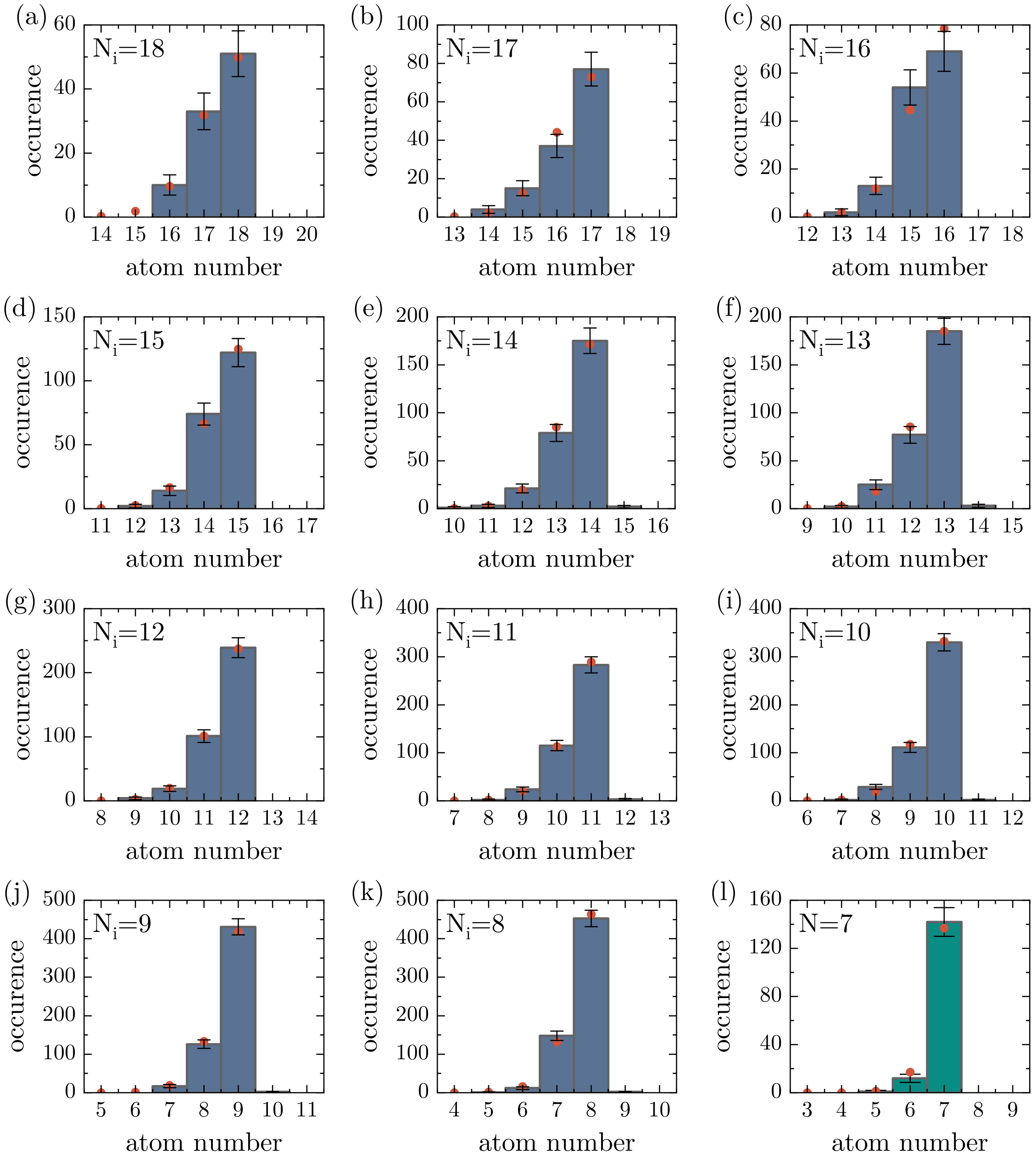

Figure 4.6: Loss characterization and stabilization result. (a-k) Example atom number distributions after a single loss step for different initial atom numbers $N_i = 18$ to 8. Error bars indicate the statistical uncertainties of the detected counts. A collective fit of all histograms (red points) reveals the survival probability for a single atom to remain in the trap. (l) The histogram shows the atom number distribution together with the statistical error for the threshold image, after which the loss process is interrupted. The target atom number of 7 is successfully stabilized with a fidelity of 92%. A truncated binomial distribution with the derived survival probability centered at 8 atoms is fitted to the data (red points).

Even in the presence of long-term drifts the number stabilization procedure may allow number-resolved detection. The controlled and well characterized loss mechanism of the feedback-loop can be used to recalibrate the detection system. This can be realized by performing a number measurement, which is followed by several, interleaved loss and detection steps. Optimally, the obtained series of the individual atom number measurements will span the full range between the initial atom number measurement and zero. The drifted scaling factor can then be corrected by means of the individual atom number measurements, as each must correspond to an integer atom number.

CHAPTER 5

Fiber-based detection MOT system

The detection system described in the previous sections has shown remarkable results for counting and stabilizing small numbers of atoms. The result was however limited to ∼30 atoms by fluctuations and drifts of the number calibration. Although the previous results were obtained with an active intensity and frequency stabilization, a slowly varying scaling factor still hinted for long-term drifts in the intensities and frequencies of the MOT beams, as discussed in Section 4.1.4. The origin of this fluorescence noise can be an interplay between various technical problems that cannot be quantified easily. In a first step, potential issues leading to this fluorescence noise can be identified by a qualitative analysis of the optical setup of the previous detection MOT as shown in Fig. 3.3.

The first issue of the detection MOT setup employing free-space optics can be related to the very long optical path lengths. After passing the 50:50 beam splitter, the MOT beams are subsequently split into three pairs of counter-propagating beams. The distances of the MOT beams from the 50:50 beam splitter to the center of the science cell are different and range approximately between 0.9 m and 1.8 m. In addition, the beams are focused to a waist of 0.75 mm, which corresponds to a Rayleigh length of $z_R = 2.3\,\mathrm{m}$. Therefore, at the center position of the MOT, the beam waists will differ and affect the peak intensity that is seen by the atoms. Furthermore, the long optical paths in conjunction with the small beam sizes deteriorate the pointing stability of the beams, especially during small temperature changes. A second issue is the occurrence of interference effects at the MOT position, since all beams have the same frequency. In addition, splitting the MOT cooling light by a PBS into counter-propagating beam pairs and recombining them again on the same PBS can be regarded as a closed-loop optical interferometer, due to possible reflections. Moreover, the beam pairs are formed by exiting different ports of the PBS with a non-perfect extinction ratio, which may lead to a lower degree of polarization of one beam with respect to the other.

The single-particle detection has achieved remarkable results, but is very sensitive to misalignments, which makes it less reliable. The motivation is to refine and replace it by a new dedicated setup based on optical fibers. In the following sections, the design and setup of the second-generation detection MOT is presented, which aims to improve spatial and temporal instabilities.

5.1 Optical setup of the fiber-based detection MOT

The optical setup for the detection MOT is split into two parts, one on the optics table and one on the vacuum table, as shown in Fig. 5.1 and Fig. 5.3. The cooling and repump light for the detection MOT beams are prepared on the optics table and guided via optical fibers to the vacuum table. This fiber-based design intends to keep a compact setup on both tables in order to avoid spatial instabilities due to extended optical path lengths.

Optics table

The cooling light for the MOT beams is provided by coupling a fraction of the light from the 3D-MOT path via a polarization-maintaining fiber, as shown in Fig. 2.7. It is first cleaned in polarization by means of a PBS and guided through a succession of six $\lambda/2$-wave plate and PBS pairs, which split the light into six identical beam paths with equal optical powers. The power of the transmitted beam is reduced in a cascaded way until it hits a beam block after the last PBS. Each reflected beam then passes through an AOM (Gooch & Housego, AOMO 3080-125), which deflects it into the positive first diffraction order and shifts its frequency by 80 MHz. In this additional frequency shift to the cooling light detuning is compensated by another shifting AOM with 80 MHz center frequency in front of the detection setup, which diffracts the beam into the negative first diffraction order. In this way, the single-pass AOMs allow to control the intensity and frequency of each MOT beam independently. The beams are again coupled into polarization-maintaining fibers by means of two coupling mirrors and a $\lambda/2$-wave plate. Optical isolators prevent cross correlations between the intensity stabilizations of the beams through potential back reflections or

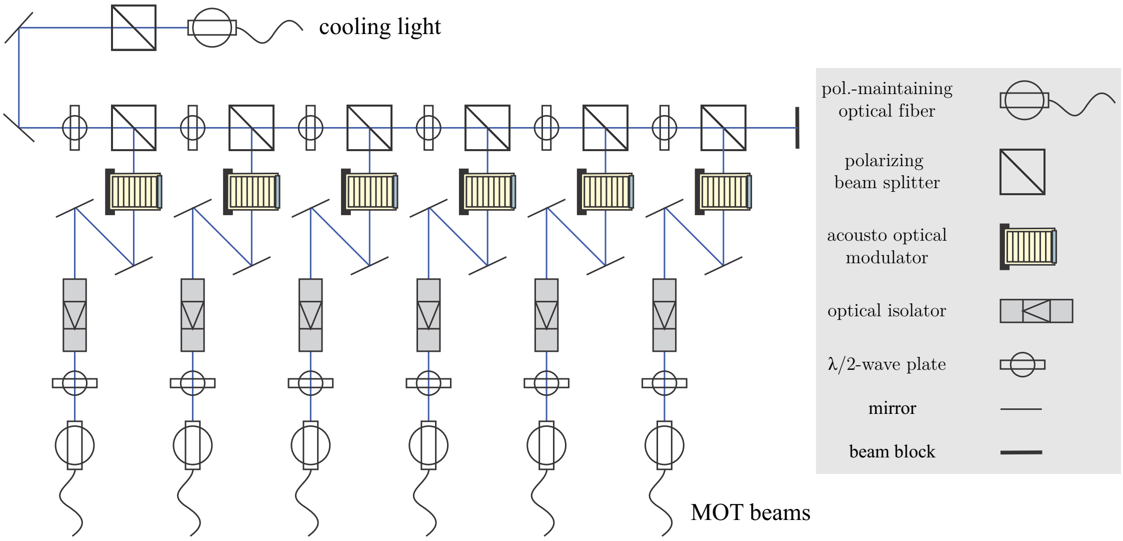

Figure 5.1: Detection MOT setup on the optics table. The cooling light for the detection MOT operation is derived from the 3D-MOT cooling path and distributed over six polarization-maintaining fibers, which provide the light for the detection MOT beams.

back-coupling of overlapped, counter-propagating beams. The six fiber-coupled MOT beams as well as the repump beam (Fig. 2.7) are finally transferred on the vacuum table.

Fiber collimators

The detection MOT beams are guided to the atoms by dedicated outcoupling units, which are shown in Fig. 5.2 (a,b). The outcouplers come in two versions for the four horizontal and two vertical MOT beams, which solely differ in the construction geometry in order to fit closely to the science cell. The special features of the units are their compact design and the custom made aluminum holders, which allow to collimate, stabilize and align the MOT beams. A fixed-focus triplet collimator (Thorlabs, TC18APC-780) outcouples the light from the fiber and collimates the beam to a $1/e^2$ diameter of $3\,\mathrm{mm}$. The collimator is rotated, such that the slow propagation axis of the PM fiber is aligned with respect to the optical axis of the first cleaning PBS. This allows a maximum power and a fixed polarization in the transmitted path. A $\lambda/2$-wave plate in combination with a PBS is used to reflect a fraction of the light onto a silicon photodiode (Thorlabs, FDS1010), which serves as a sensor signal for the intensity stabilization. After that, two alignment mirrors are used to adjust the output beam position. The circular polarization for the MOT operation is adjusted by a $\lambda/4$-wave plate. In contrast to the horizontal MOT beams, the vertical beams cannot enter the glass cell directly, due to the limited space above and below the 3D-MOT coils. Instead, the outcoupled vertical beams are guided via a mirror and a fixed $\lambda/4$-wave plate of the two-inch optics of the 3D-MOT. Therefore, the last $\lambda/4$-wave plates of the vertical outcouplers are replaced by $\lambda/2$-wave plates in order to adjust the circular polarizations. The horizontal and vertical MOT beams are left- and right-handed circularly polarized, respectively. Each beam has an output power of $140\,\mu\mathrm{W}$ which corresponds to a total saturation parameter of $I/I_s = 6.5$.

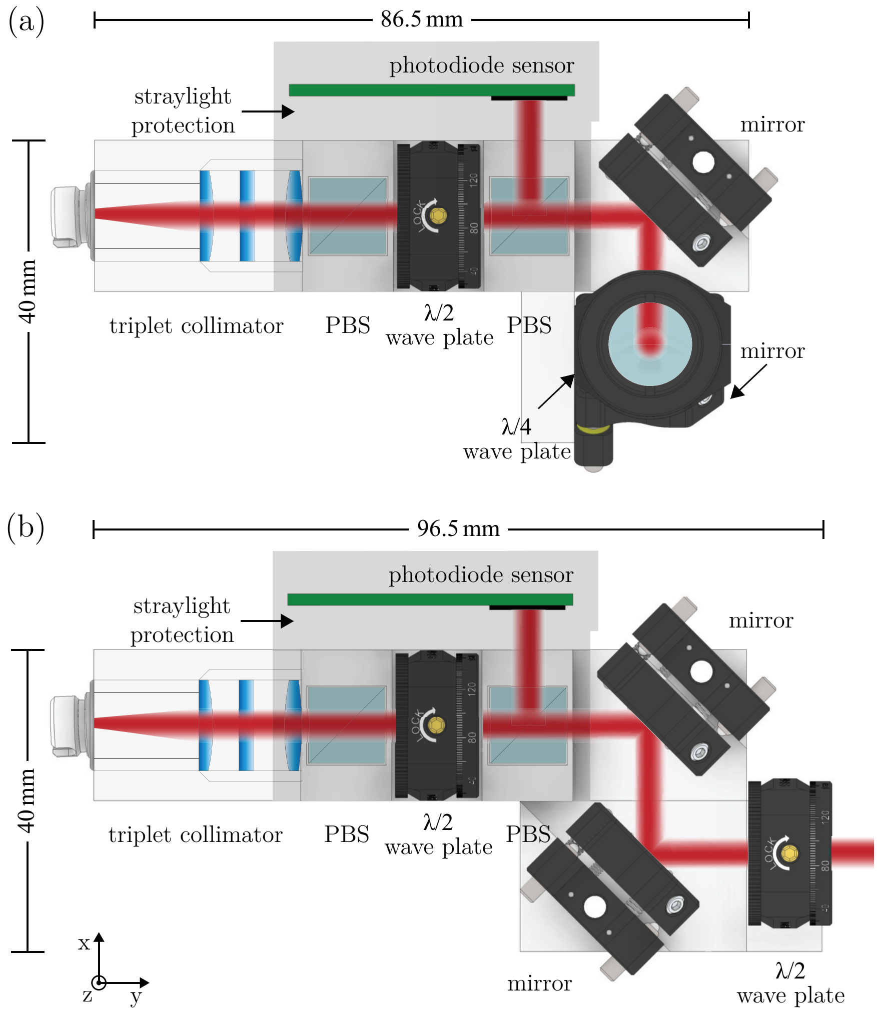
(a)
86.5 mm
photodiode sensor
straylight protection
mirror
40 mm
triplet collimator
PBS
λ/2 wave plate
PBS
mirror
λ/4 wave plate
(b)
96.5 mm
photodiode sensor
straylight protection
mirror
40 mm
triplet collimator
PBS
λ/2 wave plate
PBS
x
z
y
mirror
λ/2 wave plate

Figure 5.2: Detection MOT beam outcouplers. The 1:1 scaled technical drawings show a top view of the two outcoupler types for the (a) four horizontal and (b) two vertical MOT beams. The outcouplers come in mirrored pairs with respect to the yz-plane, in order to fit into the coil and optics setup close to the science cell. The half-inch free-space optics are mounted on custom-made aluminum holders, which are designed to align the optical axis of each component. The triplet collimator is placed inside the cylindrical rear hole of the aluminum holder and wrapped in a retaining ring, which is used to fix the collimator in position with a side screw pressing against it. The 10 mm × 10 mm polarizing beam splitters are glued with a two-component adhesive onto the aluminum holder. To each holder, a PCB with a 10 mm × 10 mm active area photodiode sensor including an amplifier stage is mounted. 3D-printed polypropylene protection covers shield the photodiodes from ambient straylight sources.

Vacuum table

The horizontal beam outcouplers are arranged in a periscope-like setup and placed symmetrically around the science cell. The beams are tilted with respect to the main optical axis along the y-direction and enter the science cell at an angle of 35°. This configuration avoids the blocking of the 15 mm big horizontal 3D-MOT beams, which are essential for the inital atom loading. However, by narrowing down the angle between the main optical axis and the MOT beams, especially coming from the side of the objective lens, can have two-fold disadvantages for the detection performance. The first issue is the potential increase of the amount of straylight originating from the MOT beams, which are reflected by the science cell surface. The smaller angle of incidence brings the reflections of the MOT beams closer to the main optical detection axis. Unwanted detection of straylight can be avoided by blocking the reflections in the detection system by exploiting their definite direction. A second difficulty arises by interference effects, which can lead to instabilities in the MOT position, due to varying intensity landscapes. The capability of tuning each MOT beam independently in frequency helps to avoid standing-waves by introducing small frequency shifts of a few kHz for each individual beam.

The outcouplers for the bottom and top MOT beams are mounted on the main vacuum table and a third optical breadboard above the science cell. Both beams do not enter the

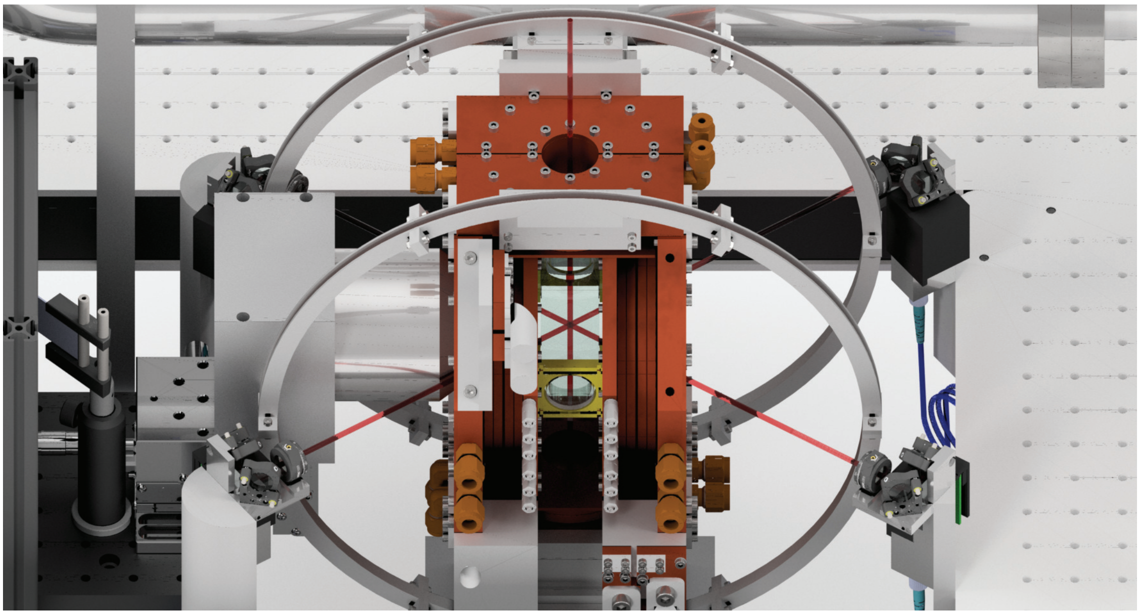

Figure 5.3: Detection MOT setup on the vacuum table. The six detection MOT beams are arranged in a group of four horizontal and two (not shown) vertical beams. Each horizontal beam enters the science cell at an angle of 35° with respect to the optical axis in the y-direction. The repump beam (not shown) is pointing up diagonally (out of the image plane) through the center of the science cell at an angle of 45° with respect to the vertical z-direction.

science cell perfectly vertical due to the 3D-MOT optics in between. The average distances of the horizontal and vertical outcouplers to the center of the science cell are 250 mm and 600 mm, respectively. In contrast to the previous detection MOT setup, this arrangement of the outcouplers shortens the optical path lengths of the MOT beams significantly and allows to minimze pointing instabilities.

5.2 Intensity stabilization

A crucial requirement for the single-atom-resolved detection in the MOT is a constant fluorescence- and background signal. However, the output intensity of a MOT cooling beam is generally subject to noise, which can enter through various sources along its way from the optics to the vacuum table. Slow drifts in the intensity are usually attributed to changes in the temperature of the employed components. One example is the non-perfect coupling of the cooling light's polarization with respect to the slow propagation axis of a PM fiber. Temperature variations can change the birefringence of the fiber and lead to polarization fluctuations. These are in turn translated into intensity fluctuations after passing through a cleaning PBS. A second example is the diffraction efficiency of an AOM (i.e. the number of scattered photons) into the first-order beam, which is affected by temperature variations of the crystal. On the other hand, fast intensity fluctuations can occur by coupling to electronic noise, such as laser driver current or tapered amplifier noise. These circumstances make an instensity stabilization for the underlying detection system an essential necessity.

5.2.1 Feedback control system

A six-way negative-feedback control system is employed for the six detection MOT beams in order to provide an adjustable beam intensity with suppressed short- and long term fluctuations. The block diagram of the intensity stabilization scheme for a single beam path is illustrated in Fig. 5.4. Its design is based on the control theory of Linear Time-Invariant (LTI) systems [134]. The feedback loop employs a PID controller that applies corrections x to the noise affected intensity by means of a voltage-controlled attenuator (VCA) (Mini-Circuits, ZX73-2500+) and RF amplifier (AA opto-electronic, AMPB-B-34-20.425), which are used to adjust the input RF power w of the AOM and consequently the efficiency of the first-order diffracted beam as shown in Fig. 5.1. The controlled intensity output $i = i_{fr} + i_{corr}$ is a sum of the free-running (uncontrolled) intensity $i_{fr} = i + i_d$ including disturbances i_d and the applied corrections i_{corr} which ideally cancel these noise contributions.[1] In order to apply the right corrections, the intensity is detected on a photodiode sensor. The scaled sensor signal y, which consists of the ideal signal and the sensor noise n_s, is added to the reference setpoint u, which is given by the analog card

---

[1] In general, the intensity output of the free-running AOM cannot be measured independently of the disturbance.

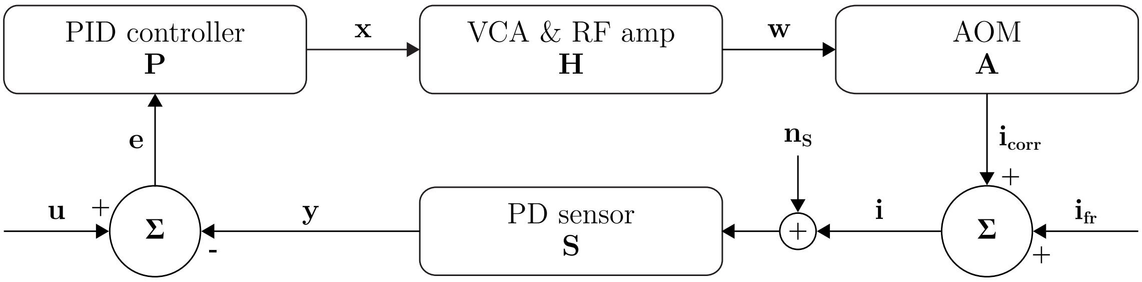

Figure 5.4: Intensity stabilization block diagram. The scheme of the feedback loop is described by single-input-single-output devices and corresponding signals, which are illustrated by blocks and arrows, respectively. The PID controller, VCA & RF amp, AOM and photodiode sensor are represented by their respective transfer functions $P(s)$, $H(s)$, $A(s)$ and $S(s)$. The signals are understood as follows: setpoint u, error e, PID output x, amplified RF output w, controlled output intensity $i = i_{fr} + i_{corr}$, photodiode output y and sensor noise n_s.

of the experiment control system. The resulting error signal e closes the loop by being applied to the PID controller.

5.2.2 Radio-frequency setup

The aim of the underlying intensity stabilization is to gain linear control over the output intensity, which should be tunable for a large range of input voltages of the VCA. However, the employed VCAs and AOMs show a nonlinear behavior of the AOM RF power and diffraction efficiency for different control voltages, as shown in Fig. 5.5 (a-c). The working point is chosen at an RF power of 0.4 W and a control voltage of 6 V, where the diffraction efficiency is at 50 % and both the VCA and the AOM show an approximately linear behavior. The offset also depends on the initial RF power. The full RF setup for each stabilization path is illustrated in Fig. 5.6. The RF signals are generated by six independent DDSs, whose frequencies and output powers are configured only once via the experiment control computer. Each DDS generates an output frequency close to 80 MHz at −2 dBm. The RF signals are first passed through bandpass filters (Mini-Circuits, ZX75BP-B70-S+) in order to avoid the amplification of higher harmonics. After that, the VCAs attenuate the signals by −8 dB for a control voltage of 6 V. The power amplifiers raise the signal levels again up to 26 dBm.

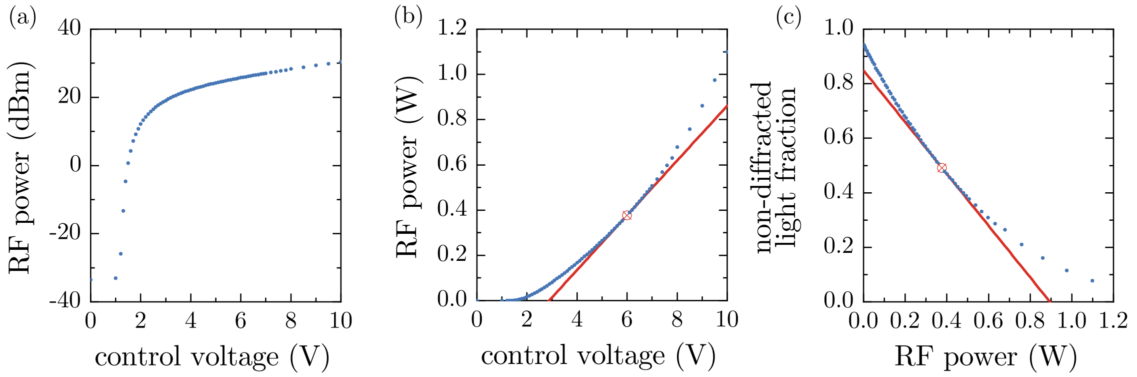

Figure 5.5: VCA and AOM nonlinearity. Logarithmic (a) and linear (b) input radio-frequency power of the AOM as a function of the VCA control voltage. (c) Percentage of light diffracted into the first-order beam as a function of the AOM RF power. The red encircled cross marks the working point at 6 V, which is used as an output offset for the PID. At this point, the diffraction efficiency of the AOM is at 50 %. The linear fit shows the approximate regime for a linear response.

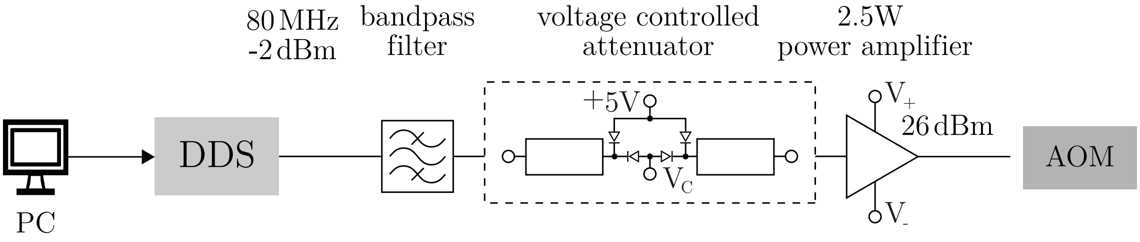

Figure 5.6: VCA array setup. A single representative out of the array of six identical VCA setups is shown. The RF signal is generated by a DDS, which is connected to the experiment control system. The filter has a passband of 52 – 88 MHz. The VCA is supplied with 5 V and accepts a control voltage V_c of 0 – 17 V. The 2.5 W power amplifier has a specified gain of $\geq$ 36 dB.

5.2.3 Photodiode sensors

The employed photodiode sensors for monitoring the MOT beam intensities are implemented on dedicated printed circuit boards (PCBs) with an integrated transimpedance amplifier circuit, which is shown in Fig. A.4. The photodiodes are supplied by a DC voltage of 5 V and have a maximum output of 3.5 V.

5.2.4 Noise suppression

The effects of the intensity stabilization can be identified by expressing the controlled intensity output from the scheme in Fig. 5.4 as

$$i = \frac{1}{1+L} i_{fr} + \frac{1}{S} \frac{L}{1+L} u - \frac{L}{1+L} n_s, \tag{5.1}$$

where $L = SPHA$ is the open-loop transfer function. For a high open-loop gain $|L(j\omega)|$ the controlled intensity output reduces to

$$i = \frac{i_{fr}}{L} + \frac{u}{S} - n_s. \tag{5.2}$$

This equation signifies that the closed-loop causes the controlled intensity output i to track the reference setpoint u, which is scaled by the gain of the sensor S, including sensor noise n_s. In addition, the free-running intensity i_{fr} is suppressed by the magnitude of the open-loop transfer function $|L|$. In order to assess the performance of the underlying closed-loop feedback control system, the frequency response of the open-loop system L and the maximum noise suppression factor $1/(1+L)$ can be analyzed, which are shown in Fig. 5.7 (a,b) and Fig. 5.8 (a,b) for each stabilization path. The Bode diagrams of the open-loop transfer function can be used to identify stability margins for the magnitude and phase. The control system is unstable, if the phase exceeds $-180°$ for frequencies with a magnitude larger than 0 dB. The phase and gain margins are 63° and -20 dB, respectively. A phase margin of 60° is recommended for a stable tracking of the reference. This has a lower priority for the pursued fluorescence detection with low intensity noise. For a better noise suppression, this margin can be decreased even further to 30°. However, changing the setpoint u will have an impact on the open-loop transfer function, due to the nonlinearity of the feedback components. Therefore, the current settings for the PID parameters guarantee a stable operation of the intensity stabilization. The open-loop representation reflects the calculated maximum noise suppression, which reaches a value of 0 dB at a frequency of 100 kHz. The suppression of noise decreases continuously within the unity-gain bandwidth. Low frequencies at 30 Hz are suppressed by a factor of 100, whereas frequencies above 300 Hz are suppressed by less than a factor of 10. Neglecting sensor noise, these values provide a first estimate for the expected intensity noise suppression. A rigorous characterization of the long-term stability of the intensity still needs to be done, which can be achieved by measuring the intensity with an out-of-loop photodiode and evaluating the rms noise. Possible limitations in the noise suppression can be expected by the sensor noise, especially for lower frequencies. However, increasing the open-loop gain will not only help to decrease the noise contribution of the free-running intensity, but will also suppress the sensor noise of the sensor output signal by $|L|$. In addition, the VCAs are currently the limiting factor with respect to speed, which have a rise and fall time of 14 μs and 25 μs, respectively. These can be replaced by linearized VCAs or mixers.

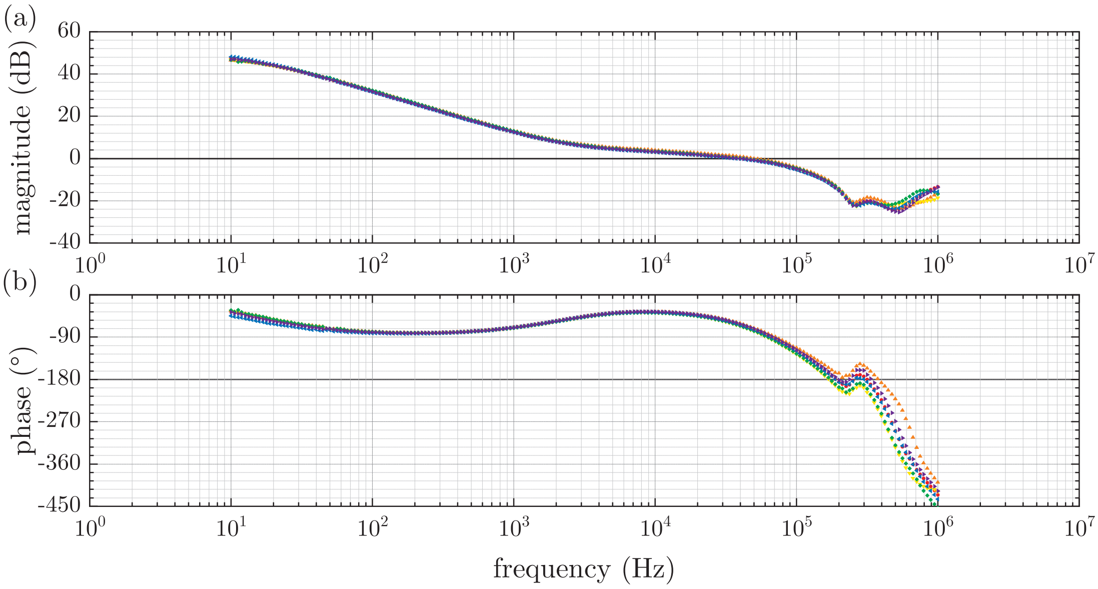

Figure 5.7: Bode diagram of the open-loop transfer function. The frequency responses for (a) the magnitude and (b) phase of the open-loop system for each intensity stabilization path are recorded from 10 Hz to 1 MHz. The magnitude is related to the amplitude level in V with a scaling of 20 dB/decade.

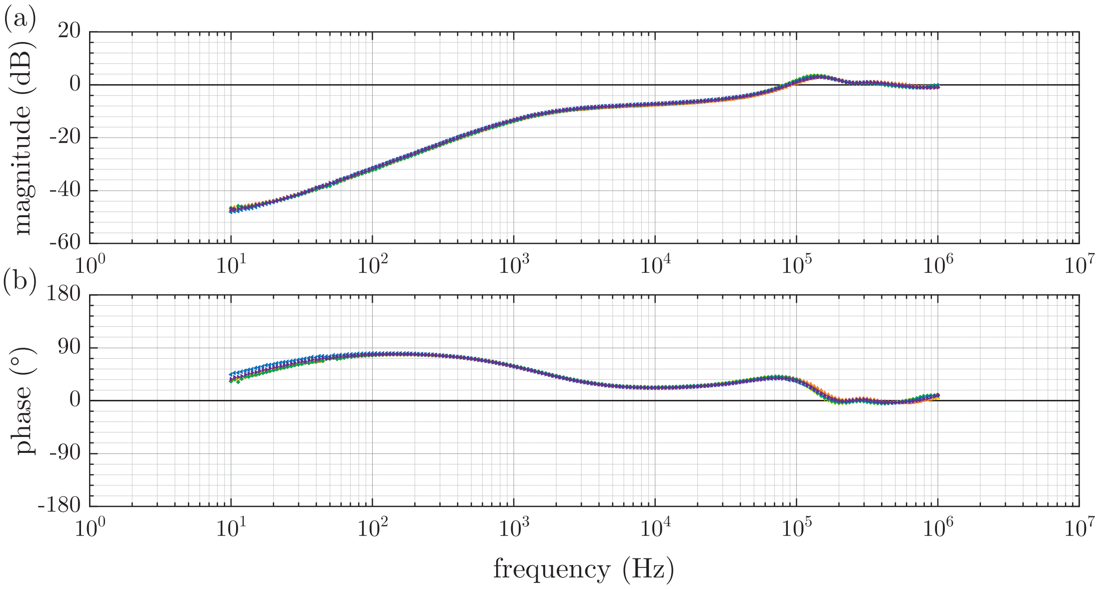

Figure 5.8: Bode diagrams of the maximum noise suppression. The frequency responses for (a) the magnitude and (b) phase of the noise suppression for each intensity stabilization path are recorded from 10 Hz to 1 MHz. The magnitude is related to the amplitude level in V with a scaling of 20 dB/decade.

5.3 Frequency stabilization

Noise contributions of the MOT cooling light frequency can be directly reflected in the fluorescence signal, since the scattering rate depends nonlinearly on the laser frequency detuning with respect to the cycling transition.[1] The linewidths of the underlying ECDLs can have various frequency noise contributions that are associated with environmental and fundamental noise [135]. Typical environmental noise sources are 50 Hz noise that couples through the power line or acoustically coupled noise at frequencies that are in mechanical resonance with the laser components. Moreover, the fundamental frequency-noise spectrum of the laser diode is usually characterized by two components: white noise at high frequencies and pink noise ($1/f$ noise) at low frequencies [136]. The latter is the dominant and more relevant noise source for the MOT detection application with a detection time of about 100 ms.

A common way to acively stabilize the laser frequency is to utilize feedback control on a Doppler-free saturation absorption spectroscopy setup. In order to properly lock the laser frequency a suitable error signal from the sub-Doppler spectrum needs to be obtained. One method, which was used before the implementation of the new detection MOT system, is frequency modulation spectroscopy (FMS). For this, the frequency of the laser[2] is modulated [138], which generates an error signal that is proportional to the first derivative of the hyperfine absorption spectrum. In this way, the generated dispersive error signal allows the feedback control to not only lock the laser but also track the direction of frequency deviation. However, there are two main disadvantages. The error signal is embedded on top of the doppler broadened absorption spectrum and closely separated neighboring hyperfine transitions can overlap and degrade the locking of the laser. In addition, the locking depends on the zero crossing of the error signal, which due to the broad doppler profile relies on a proper background subtraction and makes it therefore susceptible to background noise. The formerly used frequency modulation spectroscopy had a modulation frequency of 50 kHz that limited the bandwidth of the frequency stabilization.

5.3.1 Modulation transfer spectroscopy

The frequency stabilization setup is taken a step further and replaced by a pump-probe technique using modulation transfer spectroscopy (MTS). It produces sub-Doppler lineshapes as a sensor signal for frequency stabilization. In contrast to FMS, the MTS error signal readily provides a zero background level, which automatically leads to a more robust locking scheme. The error signal is generated by a frequency modulation of the pump beam, which is then transferred to the probe beam. This modulation transfer involves a four-wave mixing (FWM) process [139, 140], which is a consequence of the third order susceptibility $\chi^{(3)}$ of the nonlinear atomic medium. The nonlinear interaction can be described by a parametric process, where two frequency components of the pump beam combine with the counter-propagating probe beam to produce a fourth (phase-conjugate) wave, which is a sideband of the probe beam. FWM is strongest and only takes place for closed transitions of the ^{87}Rb hyperfine spectrum, if the sub-Doppler resonance conditions (Appendix A.2) are satisfied [93]. A consequence of the occurence of the modulation transfer within the natural linewidth of the sub-Doppler resonance is a flat and zero background of the error signal, while the zero crossing is always centered to the resonance. This makes the MTS signal almost independent of changes in the absorption due to intensity or polarization, which is the main feature of the MTS.

---

[1] In general, the sensitivity of the scattering rate to the laser frequency noise can be lowered by shifting the detuning closer to or far away from resonance. However, a very large or small detuning would lead to a very low scattering rate and an unstable MOT due to a high photon pressure, respectively.

[2] Alternatively, the reference frequency, e.g. atomic resonance transition, can be modulated [137].

The following sections describe the frequency stabilization scheme using the MTS as a sensor for the feedback control system.

5.3.2 Feedback control system

Similar to the intensity stabilization, an active feedback loop is employed for the laser frequency, as shown in Fig. 5.9. The error signal e is generated by the MTS setup, which is compared to the reference setpoint of $u = 0\,\mathrm{V}$. The frequency is locked with respect to the zero crossing of the MTS signal. The PID controller applies two corrections x_f, x_h by means of a piezo and current driver, respectively. The piezo and current paths compensate for the slow and fast fluctuations of the laser frequency. The effect of the applied corrections of the piezo and current paths is assumed to be not interfering with each other, such that both contributions to the frequency regulation are added. The controlled frequency output $\omega = \omega_{fr} + \omega_{corr}$ can be represented by the free-running output ω_{fr} of the laser and the applied correction frequency ω_{corr}.

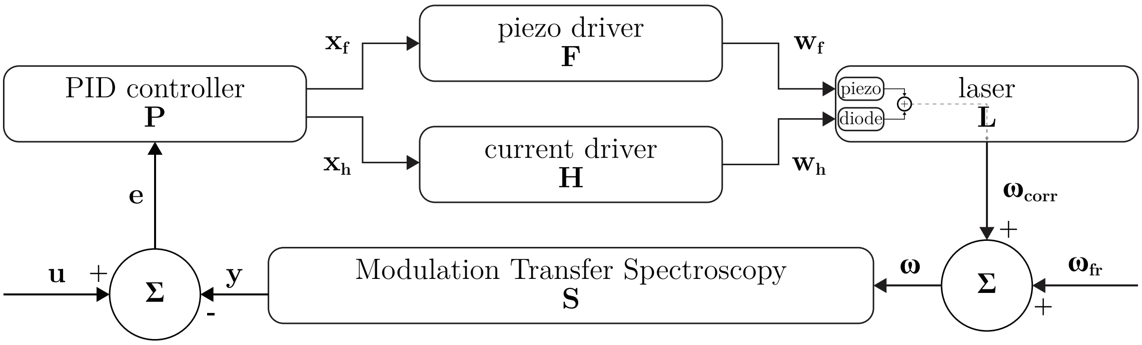

Figure 5.9: Frequency stabilization block diagram. The frequency stabilization control loop employs a MTS sensor S in order to generate the error signal $e = u - y$ for laser locking. The diagram is almost equivalent to the intensity stabilization scheme in Fig. 5.4. The components are represented by their respective transfer functions P,F,H,L and S. The PID controller P applies two correction signals x_f, x_h to the laser plant via a piezo F and current driver H. Slow and fast fluctuations are compensated by the two piezo mirrors and the laser diode, respectively.

5.3.3 Optical setup of the modulation transfer spectroscopy

MTS is an advanced pump-probe technique, which relies on Doppler-free saturation absorption spectroscopy. The corresponding optical setup for stabilizing the frequency of the ECDL that provides the cooling light for the MOT is shown in Fig. 5.10. The ECDL has a base wavelength of 780 nm ($\omega \approx 2\pi \times 384\,\mathrm{THz}$) and can be tuned to the ^{87}Rb D$_2$ line transition by varying the current and voltage of the laser and piezo driver, respectively. An optical isolator in front of the laser protects the laser diode from damage due to potential back reflections. The resulting $20 - 30\,\mathrm{mW}$ output power is split by a succession of two PBS and $\lambda/2$-wave plates into two frequency stabilization paths. The second PBS sends a fraction of the cooling laser power to the microwave interferometer in order to phase-lock the repump laser to the cooling laser. The transmitted part of the PBS guides the cooling light into the MTS setup.

The beam is split into two paths with orthogonal linear polarizations, which are designated as pump and probe beam path. The transmitted pump beam is sent through an AOM in double-pass configuration, which shifts its frequency ω by $2\delta = 2 \times 200\,\mathrm{MHz}$ and imprints two sidebands at $\omega + 2\delta \pm \Omega$. The retro-reflected first-order pump beam is then collinearly superimposed with the unmodulated probe beam within a 60° C heated vapor cell[1], which contains a natural mixture of ^{85}Rb and ^{87}Rb. Before entering the vapor cell, both beams are enlarged by two corresponding beam expanders (Thorlabs, GBE05-B), which increase the beam waists by a factor of 5 to ensure an overlap that is insensitive to small beam displacements and a total optical power below the saturation intensity. Due to the frequency shift of the pump beam, only those atoms are addressed by the beams, whose Doppler shifted velocities correspond to a detuning of 200 MHz below the closed hyperfine transition $|F = 2\rangle \rightarrow |F' = 3\rangle$. Nonlinear interactions between a pump carrier $\omega + 2\delta$, pump sideband $\omega + 2\delta \pm \Omega$ and a probe photon ω result in the generation of a fourth photon $\omega \pm \Omega$ whose momentum is parallel to the probe beam. After passing through the second beam expander, the beat signal between the modulated $\omega \pm \Omega$ and unmodulated probe beam ω is detected on a wideband-amplified photodiode (Thorlabs PDA10A-EC).

---

[1] The temperature of the spectroscopy cell is controlled by means of a heating foil. Styrofoam with appropriate holes for the cell entrances is used to provide heat isolation and maintain a constant temperature inside the cell. In addition the cell is surrounded by a mu-metal shielding to minimize magnetic field fluctuations.

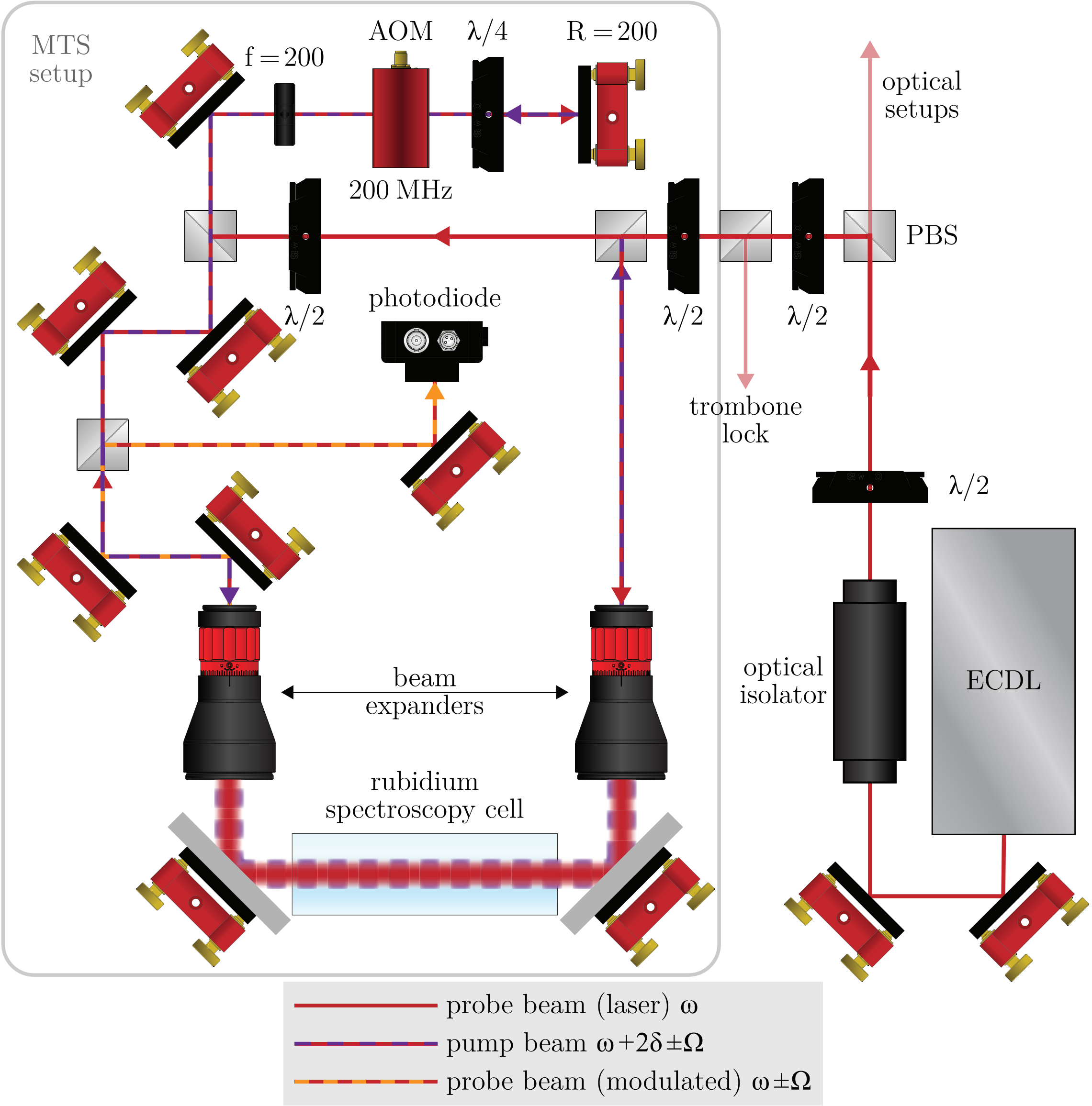
MTS
setup
f = 200
AOM
λ/4
R = 200
200 MHz
optical
setups
PBS
λ/2
λ/2
λ/2
photodiode
trombone
lock
λ/2
beam
expanders
optical
isolator
ECDL
rubidium
spectroscopy cell
probe beam (laser) ω
pump beam ω+2δ±Ω
probe beam (modulated) ω±Ω

Figure 5.10: MTS setup. The beam exiting the cooling light ECDL is split into two paths, which are designated as pump (purple-red dashed line) and probe (red line) beam path. The transmitted pump beam is sent through an AOM in double-pass configuration. The reflected probe beam is overlapped with the counter-propagating pump beam at the spectroscopy cell, after which it is detected on a photodiode.

5.3.4 Modulation transfer spectroscopy sensor signal

The employed radio-frequency signals for the generation of the FWM and the MTS signal are shown in Fig. 5.11. The AOM's driving frequency is generated by an RF signal generator f_1 (Marconi Instruments, 2024) and a two-channel arbitrary waveform generator f_2 (Keysight Technologies, 33522B). The center frequency of f_1 is at 173 Mhz with an amplitude of $-13\,\mathrm{dBm}$. The first channel of f_2 has a center frequency of 27 MHz and an amplitude of $-3\,\mathrm{dBm}$, which is frequency modulated by $\Omega = 2\pi \times 3\,\mathrm{MHz}$ with a maximum frequency deviation of $|\Delta f| = 3\,\mathrm{MHz}$. Both signals are combined by a mixer (Mini-Circuits, ZAD-1-1+), after which the sum frequency is filtered out by a high-pass filter (Mini-Circuits SHP-200+) and finally amplified by a 33 dB gain amplifier (AA opto-electronic, AMPA-B-30). The resulting RF signal drives the AOM with a center frequency of $\delta = 200\,\mathrm{MHz}$ and two first-order sidebands at $\delta \pm \Omega$. Thus, the AOM shifts the carrier frequency of the pump beam to $\omega + 2\delta$ and imprints additional sidebands at $\omega + 2\delta \pm \Omega$.[1] The frequency modulation is transferred via FWM to the probe beam. This leads to new sidebands $\omega \pm \Omega$ of the probe beam, which beat with its carrier frequency ω.

The recorded beat signal encodes the phase-sensitive information about the absorption and dispersion of the probe beam, which depends on the modulation frequency Ω and its higher harmonics Ω^n. The beat signal is described by a set of absorption and dispersion lineshapes, which to first order can be written as [141]

$$
\begin{aligned}
I_\Omega(\omega) = {} & \frac{C}{\sqrt{\Gamma^2 + \Omega^2}} J_0(M) J_1(M) \\
& \times \left[(L_{-1} - L_{-\frac{1}{2}} + L_{\frac{1}{2}} - L_{+1}) \cos(\Omega t + \varphi) \right. \\
& \left. + (D_1 - D_{\frac{1}{2}} - D_{-\frac{1}{2}} + D_{-1}) \sin(\Omega t + \varphi) \right]
\end{aligned}
\tag{5.3}
$$

with

$$
L_n = \frac{\Gamma}{\Gamma^2 + (\omega - (\omega_0 - \delta - n\Omega))^2} \tag{5.4}
$$

$$
D_n = \frac{\Gamma(\omega - (\omega_0 - \delta - n\Omega))}{\Gamma^2 + (\omega - (\omega_0 - \delta - n\Omega))^2}, \tag{5.5}
$$

where C is the constant describing the nonlinear properties of the medium, $J_0(M)$ and $J_1(M)$ are the zeroth- and first-order Bessel functions with modulation index $M = \frac{\Delta\omega}{\Omega}$, ω_0 is the atomic resonance frequency, L_n and D_n are the respective in-phase and quadrature components of the signal. The FWM resonance conditions ($n = \pm 1, \pm \frac{1}{2}$) make the beat signal dependent of the laser frequency ω, which changes the relative phase between the in-phase and quadrature components of the beat signal. In order to apply suitable corrections to the feedback loop, the heterodyne detection of the frequency modulated beat signal needs to be converted into an amplitude modulation. For this, the beat signal is

---

[1] The amplitudes of the sidebands depend on the input carrier-to-sideband amplitude ratio.

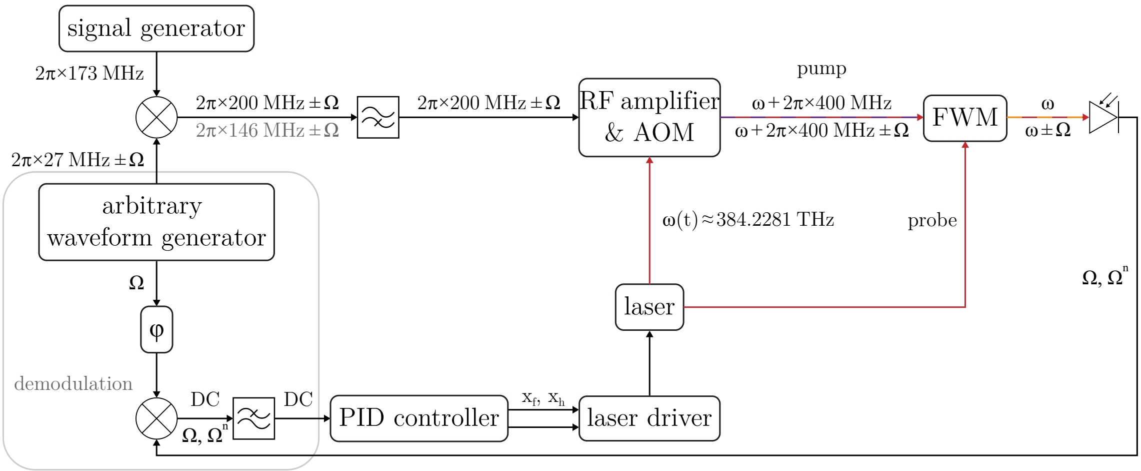

Figure 5.11: MTS sensor signal processing. This diagram shows the proccessing of the signals involved in the MTS sensor. The sidebands of the pump beam are created by mixing the 173 MHz RF output of the signal generator with the 3 MHz frequency modulated RF output at 27 MHz of the arbitrary waveform generator. A high-pass filter selects the sum frequency of 200 MHz to efficiently drive the RF amplifier and AOM. FWM then transfers the frequency modulation Ω to the probe beam. The beat signal of the probe beam ω with the modulated sidebands $\omega \pm \Omega$ are detected by a photodiode, which contains the modulation frequency Ω and higher order harmonics Ω^n. The phase-sensitive absorption and dispersion encoded in the frequency modulation is converted into an amplitude modulation by mixing the photodiode signal with the phase adjustable modulation frequency Ω from the second output of the waveform generator and only filtering out the DC component by means of a 1.9 MHz low-pass filter. The resulting DC signal is used as an error signal and applied to the PID controller.

demodulated by mixing it (Mini-Circuits, ZAD-6+)) with the same modulation frequency Ω, provided by the second output channel of the arbitrary waveform generator. Since the internal frequency generation is provided by DDSs, both output channels are phase stable to each other. The phase of the second output channel can be adjusted and allows to modify the detected lineshape of the beat signal. A low-pass filter (Minicurcuits BLP-1.9+) is used to suppress higher harmonics. The resulting DC signal serves as an error signal for the PID controller, which subsequently applies corrections to the laser via its piezo and current diver.

The dispersive spectroscopy signal is derived by scanning the laser frequency with respect to the center FWM resonance line $\omega_0 - \delta$, which is shown in Fig. 5.12 (a). The relative phase of the demodulation signal is set to 70° and optimized for a maximum MTS signal, which has a peak-to-peak value of 220 mV. In order to evaluate the short term stability of the frequency lock, the error signal was logged for 15 minutes and the frequency deviation $\Delta = \omega - (\omega_0 - \delta)$ is plotted in a histogram as shown in Fig. 5.12 (b). The histogram is characterized by a normal distribution with a standard deviation of $\sigma_f = 22.57$ kHz. This

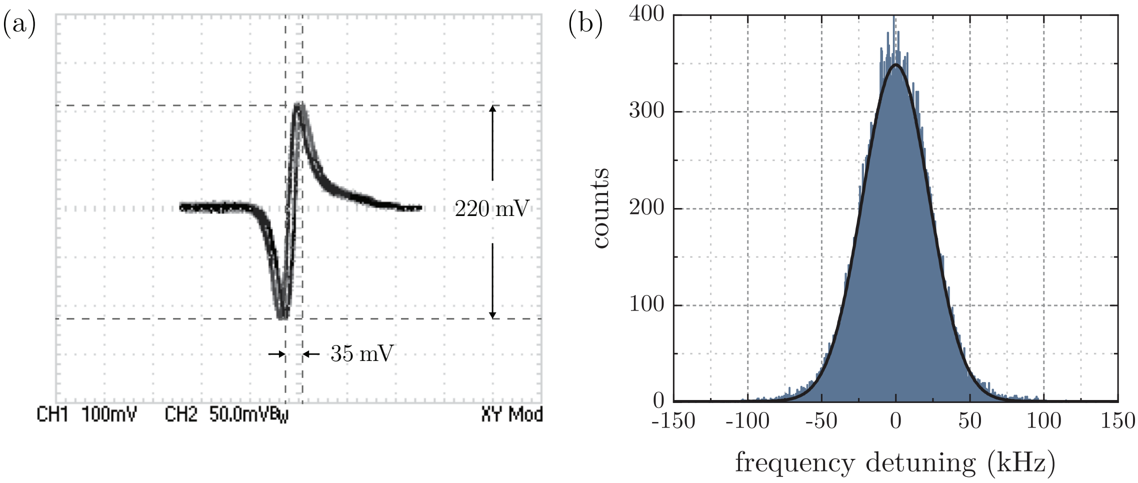

Figure 5.12: MTS error signal & frequency stability. (a) MTS error signal on the oscilloscope as a function of the scanning piezo voltage. (b) The in-loop error signal of the stabilized laser was recorded for 15 minutes and plotted as a histogram, where the horizontal axis corresponds to the frequency detuning and the vertical axis to the detected counts. Each data point is averaged over 20 ms. The scaling of the error signal as a function of frequency is estimated by the distance between its minimum and maximum, which corresponds to the full width at half maximum (FWHM) of the natural linewidth Γ.

represents an upper limit, since the data points for the frequency recording were averaged over 20 ms compared to the MOT detection time of 65 ms. This frequency noise represents only a lower boundary, since it does not reflect the noise contributions of the feedback control loop.

The impact of the frequency noise on the detected atom numbers is directly proportional to the relative change in the scattering rate. A simple estimation for the corresponding scattering rate noise can be made by applying error propagation to Eq. 4.1 with respect to the detuning frequency

$$\frac{\sigma_{R_{sc}}}{R_{sc}} = \frac{\sqrt{\left(\frac{\partial R_{sc}}{\partial \Delta}\sigma_\Delta\right)^2}}{R_{sc}}. \tag{5.6}$$

The frequency detuning dependency of the relative scattering noise for an absolute laser frequency noise of $\sigma_\Delta = 2\pi \times 22.57\,\text{kHz}$ and a saturation intensity of $I/I_s = 6$ is depicted in Fig. 5.13. The expected relative change in the scattering rate due to laser frequency noise is at maximum 0.28%. The corresponding noise of the detected atom numbers can be estimated by

$$\sigma_N = \frac{\sigma_{R_{sc}}}{R_{sc}} N. \tag{5.7}$$

The maximum scattering rate noise sets an upper limit of 357 atoms for the single-atom resolution, which per definition is reached for $\sigma_N = 1$. To increase the detection limit to 1000 atoms a frequency detuning below 1.5 MHz or a frequency noise of at least 10 kHz would be necessary.

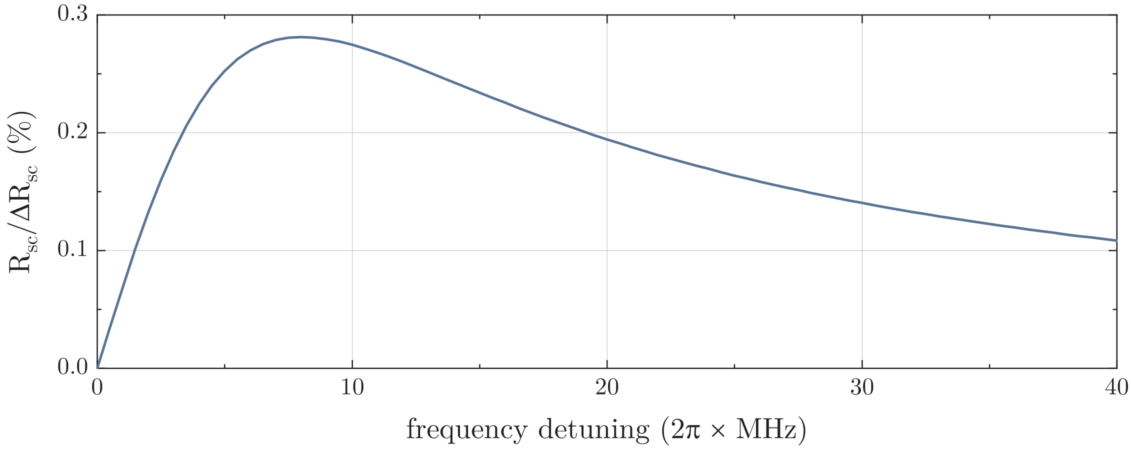

Figure 5.13: Relative scattering noise. The relative scattering noise as a function of frequency detuning is calculated for a laser frequency noise of 22.57 kHz and a saturation intensity of 6 MHz. The relative scattering noise increases linearly and summits at 0.28% for a detuning of 8 MHz.

5.4 Preliminary single-atom counting data

After having the components set in place, the next step will be to find suitable parameter settings for the new detection system, which can be best assessed by conducting single-atom counting experiments similar to the previous one described in section 4.1.3. In the following, two preliminary measurements will be described, which can be regarded as benchmark tests of the new detection system.

A first trial measurement for single-atom-resolution is conducted by choosing detection parameters close to the previous settings, which correspond to a saturation parameter of $I/I_S = 6$, a frequency detuning of $\Delta = 2\pi \times 10\,\mathrm{MHz}$ and a detection time of $t_{det} = 65\,\mathrm{ms}$. The reduction of the detection time has a technical reason that is associated with the fast paced BEC experiments. The repeated high-flux loading of the science chamber can lead to a non-negligible background pressure that depends on the duration as well as cycle time of the experiments. As a consequence, this leads to a residual background loading rate, which can deteriorate the single-atom-resolution. Therefore, prior to the single-atom counting measurement, a compromise was found between a reasonable signal strength allowing to detect single atoms with a negligible background loading rate.[1] The respective detection settings provide an estimate of the expected photoelectron counts per atom to be $n_{cts}^{exp} = 16.43\,\mathrm{kcts/atom}$. However, the calibration of the detection system revealed that this

---

[1] Additionally, in order to consistently reduce the background pressure inside the science cell, light-induced atomic desorption (LIAD) LEDs are set up around the science cell. These are only turned on overnight to support the pumping of the vacuum chambers.

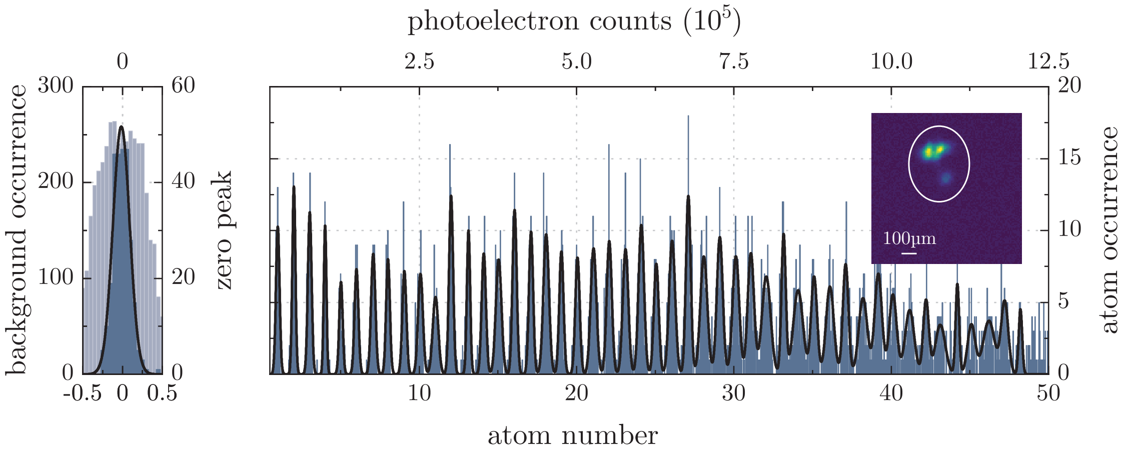

Figure 5.14: Single-atom counting data with the second-generation detection setup. The two histograms are plotted for a total of 8600 consecutively recorded single fluorescence images of the background and the MOT. Each MOT image is corrected by a corresponding background image. The two histograms show the occurrences of the recorded background (left) and atom signals (right) as a function of atom number (bottom) and photoelectron counts (top). The histogram of the pure background images (light blue) is superimposed by the background subtracted zero peak (dark blue), where occasionally no atoms were detected. The atom counts are fitted by a cumulative Gauss fit over 48 distinct peaks, which represents the resolution limit. The inset shows a typical fluorescence image of the atomic signal, which is evaluated inside a mask of size $\pi \times 25 \times 20$ pixels.

number is underestimated by a factor of 1.52.[1] After a recalibration, the corrected mean photoelectron count per atom corresponds to $n_{cts} = 25.06\,\mathrm{kcts/atom}$ (Fig. A.3), which is approximately a factor of two smaller than before, as described in Section 4.1.3. The reduction of the signal strength is reasonable and explained by the reduced detection time and the different detuning frequency. The histograms in Fig. 5.14 show the recalibrated results of the single-atom counting measurement. Fitting multiple Gauss functions to the atom number distributions shows distinct and equally spaced peaks centered around integer numbers up to 48 atoms. Above 20 atoms the distributions already start to overlap, indicating an increase in the detection noise.

The characterization of the background is a first step to quantify the lower boundary of the noise contributions to the atomic signal, as discussed in Section 4.1.4. This is done by evaluating timetrace background images as shown in Fig. 5.15 (a,b). The level of the background signal is at a mean number of 50.39(37) atoms, which is a consequence of the small angle between the MOT beams and the main detection axis as previously illustrated

---

[1] The deviation of the expected photoelectron count number per atom can be presumably related to false assumptions made about the detection efficiency that are caused by the change of its focus alignment or unconsidered additional optics in the detection path, such as bandwidth filters that were installed over the course of the experiments.

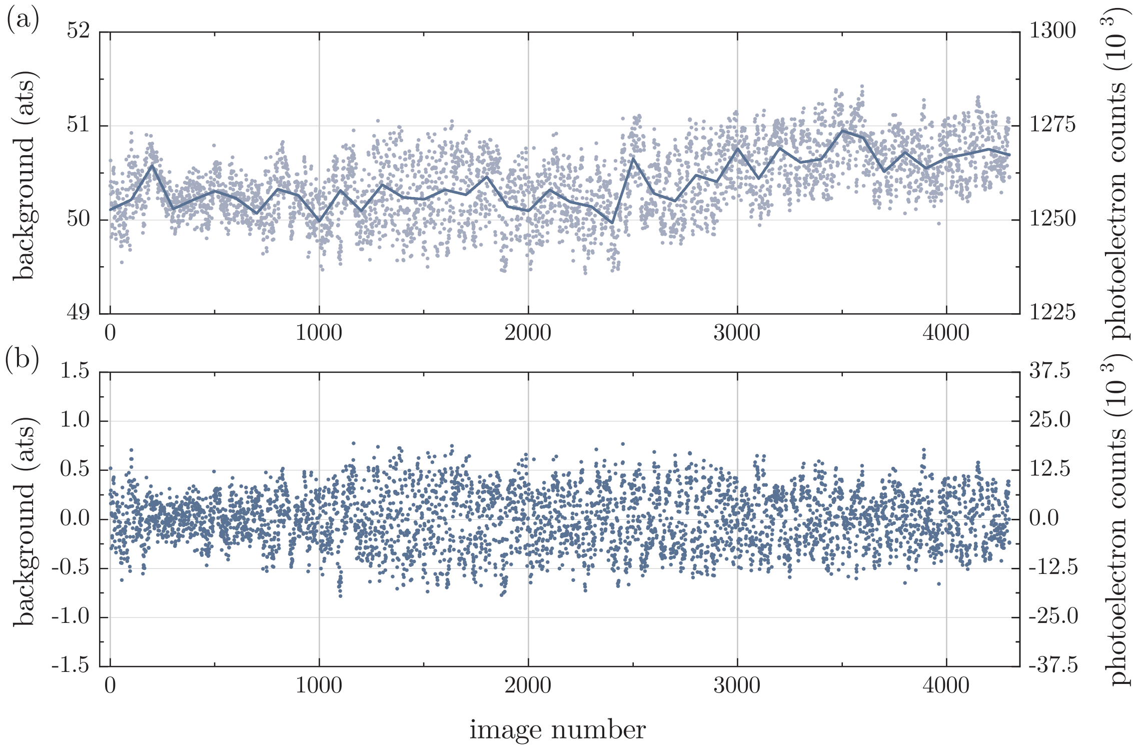

Figure 5.15: Background signal characterization for large atom number statistics. (a) Timetrace of the background signal (data points) as a function of atom number (left) and photoelectron counts (right) acquired during the single-atom counting measurement. The background signal was corrected by the readout offset of 37.92 atoms for a mask size of $\pi \times 25 \times 20$ pixels introduced by the camera. It shows a maximum drift equivalent to 0.58 atoms over the course of the measurement. The drift is corrected by linear interpolation with a step size of 100 data points (blue solid line). (b) The corrected background exhibits residual fluctuations corresponding to a standard deviation of $\sigma_{bg} = 0.28$ atoms.

in Fig. 5.3. The new configuration of the MOT beams contributes to the scattered straylight originating from various reflective parts of the experimental apparatus, particularly from the surfaces and viewports of the science cell chamber. Throughout the experimental run, the background signal shows two types of noise contributions: a slow, total drift that corresponds to a mean number of 0.58 atoms and a noise signal with a peak-to-peak amplitude of about 1.99 atoms. Correcting the absolute background level for the mean offset and the drift, leaves a residual background fluctuation of 0.28 atoms. However, the single-atom distributions exhibit much narrower peak-widths than expected by the shot noise of the background offset, which would correspond to $\sigma_N = \sqrt{50.39/n_{cts}} \approx 0.04$ atoms. Instead, this noise source can be attributed to the intensity of the MOT beams slowly varying over time, which is potentially caused by the intensity stabilization not working properly. The histogram of the residual background fluctuations and the zero peak illustrate how a proper background subtraction suppresses the fluctuations. The fast succession of

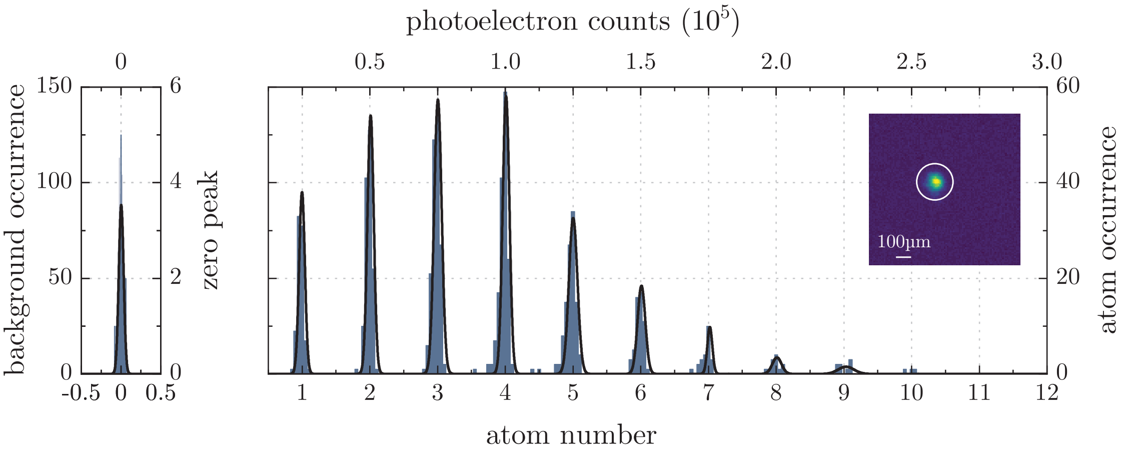

Figure 5.16: Single-atom counting data with the second-generation detection setup and improved position stability. The two histograms are plotted for a total of 1500 consecutively recorded single fluorescence images of the background and the detection MOT. The short loading time of the MOT limits the detection to a maximum of 10 atoms. The inset shows the fluorescence image of the isotropically shaped MOT, evaluated inside a mask of size $\pi \times 12 \times 12$ pixels.

background and atom image acquisition every 4 seconds makes the fluorescence signal less sensitive to sample slower background drifts. This is guaranteed by the total intensity of the MOT beams, which is a multiple of the saturation intensity. Therefore, the width of the zero peak $\sigma_0 = 0.10$ reflects the noise of the background offset at timescales shorter than a minute.

The inset in the histogram shows a typical image of the atomic cloud during the measurement sequence. The MOT has a particular anisotropic shape changing from shot-to-shot and sometimes splitting into two stable positions with a small tail at the bottom. The instability is presumably caused by power imbalances, either due to a non-perfect alignment or standing waves of the counter-propagating MOT beams. In order to counteract interference effects and stabilize the MOT shape and position the center frequencies of the six individual AOMs are randomly shifted in the range of ±20 kHz with a minimum distance of 3 kHz between the frequencies. This was investigated by a second single-atom counting measurement with the same detection settings and a better alignment of the MOT beams. The MOT was loaded only for 1 ms, which restricts the counting statistics to the detection of only small atom numbers. The corresponding results are summarized in the histograms shown in Fig. 5.16. The random detuning of each MOT beam has a great impact with respect to the stability and shape of the atomic cloud, which is reflected in its spherical and compact form, as shown in the inset. This also allows to reduce the mask size to $\pi \times 12^2$ pixels and consequently the background offset to a mean number of 14.13(5) atoms. Correcting for the offset and drift leaves a residual background noise of 0.02 atoms, as shown in Fig. 5.17 (a,b). The expected shot noise for the offset corresponds to $\sigma_N = \sqrt{14.13/n_{cts}} \approx 0.02$ atoms confirming the residual background noise. A comparison with the zero peak width $\sigma_0 = 0.03$

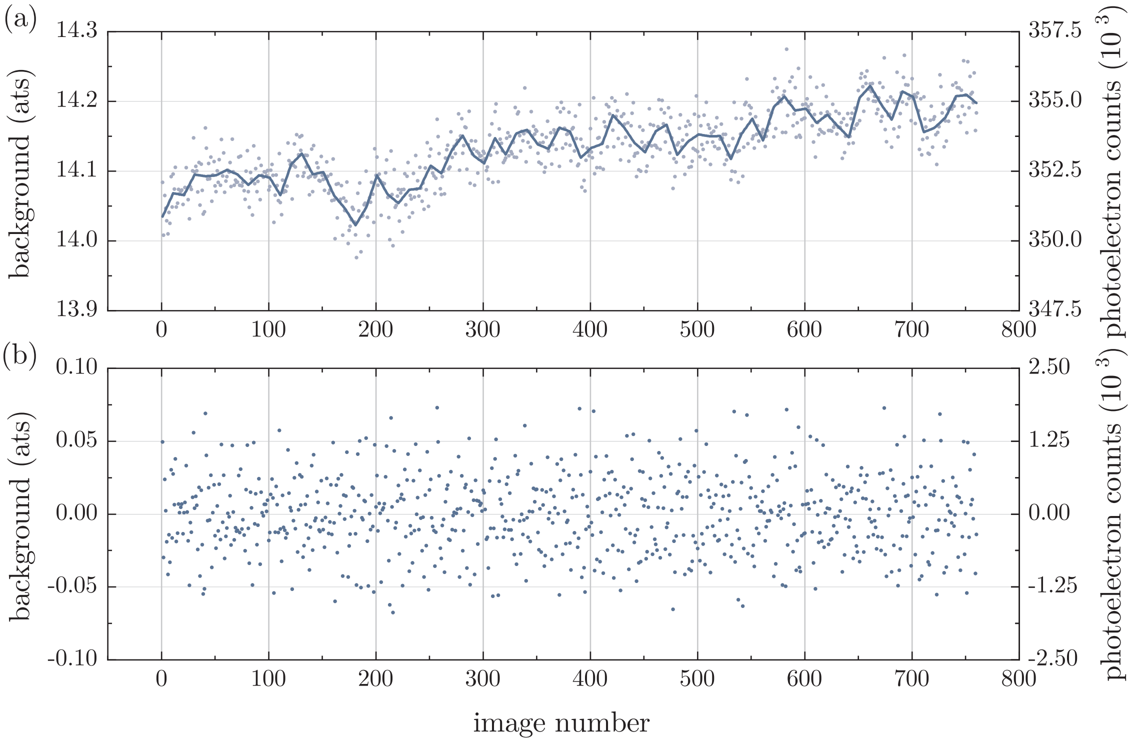

Figure 5.17: Background signal characterization for small atom number statistics. (a) Timetrace of the absolute background signal (data points) as a function of atom number (left) and photoelectron counts (right) acquired during the single-atom counting measurement. The background offset was corrected by the readout offset of 10.94 atoms for a mask size of $\pi \times 12^2$ pixels introduced by the camera. It shows a maximum drift equivalent to 0.16 atoms with a peak-to-peak noise of 0.29 atoms over the course of the measurement. The drift is corrected by linear interpolation with a step size of 10 data points (blue solid line). (b) The corrected background exhibits residual fluctuations corresponding to a standard deviation of $\sigma_{bg} = 0.03$ atoms.

assumes that a lower limit for the noise of the atomic signal is given by the shot noise of the background signal.

A comparison between all three measurements including the first-generation detection is shown in Fig. 5.18. The widths of the Gaussian peaks for atom numbers up to 10 show the successful performance of the second-generation detection setup. The narrow widths are a joint result of the stable MOT and the revisited intensity stabilization.

The performance of the detection system can be enhanced a step further by exploring for optimum values of the parameter space. Especially, the increase of the detection time will reduce photon shot noise and fluorescence noise contributions. Furthermore, setting the frequency detuning closer to resonance should make the fluorescence signal less sensitive to frequency noise. Additionally, both optimizations will automatically lead

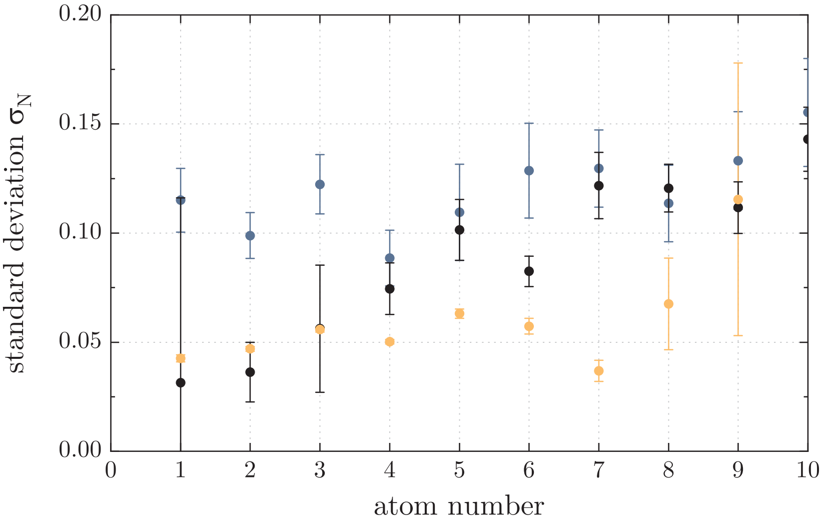

Figure 5.18: Standard deviation of the atom number distributions. The linear plot shows the fitted widths of the Gaussian distributions as a function of the atom number for all three single-atom measurements. The black circles correspond to the measurement with the first-generation detection system, while the blue and orange circles correspond the measurement with the second-generation detection system.

to a larger signal-to-noise ratio. In summary, the first demonstrations promise that the new detection setup will be a valuable tool for the preparation and detection of ultracold atomic ensembles.

CHAPTER 6

Outlook

The pathway to advanced technological applications in the realm of mesoscopic quantum systems requires improved stability, reproducability and reliability with respect to the control of the involved fragile quantum states. This thesis presented a versatile setup for a rapid production of BECs with large atom numbers and a first demonstration of the deterministic preparation of cold atomic ensembles in a MOT. These two main features of the underlying apparatus address the challenges with regard to future quantum-enhanced interferometric measurements: complexity and macroscopicity. In the pursuit of this goal, the next steps will be the generation and detection of multi-particle entangled quantum states, such as spin-squeezed states, Twin-Fock states and Schrödinger cat states. These states offer an unprecedented sensitivity for the estimation of the interferometric phase, as they shift the achievable sensitivity limit from the classical quantum projection limit to the more fundamental Heisenberg Limit [15]. In order to exploit the potential gain in sensitivity, technical noise sources have to be suppressed, such that they no longer predominate the intrinsic noise of the quantum states. The BEC production with a high repetition rate aims to reduce the cycling time and to avoid low sample rates. In this way, correction methods for potential drifts and fluctuations in the final detected atom numbers can be avoided.

6.1 Improving the BEC cycle time

The underlying apparatus accomplishes the production of BECs with 10^5 atoms every 5.6 s, which is a joint result of its two main features. A large initial number of atoms is effectively collected from a high-flux atom source in a double-MOT configuration. In addition, a hybrid evaporation scheme combines the strength of both a quadrupole and optical dipole trap, while avoiding their individual weaknesses. However, in contrast to other systems as shown in Fig. 1.1, there is still room for improvement with respect to the speed and final atom number. The major drawback of the experimental setup that limits the cycle time is the design of the quadrupole coils, which was intended to provide large optical access to the science chamber. As a consequence, constraints were put on the number of windings per coil that provide the quadrupole field. Moreover, a lower winding number is connected with faster switching times but in return with a larger power consumption. Although the wires are mounted on water-cooled copper mounts, the dissipated heat of 4 kW electrical power cannot be conducted efficiently enough to the cooling cycle. The water does not flow along the winding path and has no direct contact to the copper surface that surrounds the thick wires. Stacking the windings on top of each other makes it even more difficult to cool them and introduces a heat gradient between the layers. The temperatures of the coils depend on their duty cycle and on the maximum current supplied. Thus, the shorter the cycle time of the experiment is, the higher the coil temperatures are. The specifications of the coil wires' outer insulation layers set an upper limit on the maximum rated surface temperature and subsequently the cycle time. The steady state temperature of the coils is therefore limited to 200° C in order to guarantee the lifetime and a potential shortcut of the coil wires. The extra time needed to operate the coils below the damage threshold is added to the experimental sequence cycle time, as can be seen in Fig. A.1. Although the loading of the 3D-MOT takes up only 600 ms, an additional 1.5 s is added to the 3D-MOT loading chapter in order to compensate for the heating of the quadrupole coils. Another 400 ms are added at the end of the sequence in the de-initialization chapter. Apparently, a better cooling management would already lead to an improvement of the cylce time by almost 2 s for the same sequence. In the class of hybrid evaporation systems this would also break the record in terms of the cycle time.

An alternative approach to increase the speed of the BEC production would be to switch to an all optical evaporation scheme using a time-averaged (painted) optical dipole potential. This is realized by a center-position modulation (CPM) of the beams mediated by a 2D-AOD. The shortest cycle time of 1.6 s using painted potentials was reported for a ^{174}Yb BEC, as listed in Table 1.1. The technical hardware for the painting is already implemented and ready to use. This concept would bypass the quadrupole trap and could benefit from a compressed and temporal dark 3D-MOT phase to efficiently load the atoms into the crossed-beam optical dipole trap.

On the other hand, fine tuning of the experimental parameters can be employed by running an optimization algorithm on the experimental control system, which automatically tries to find a global optimum in the continuous and multi-dimensional parameter space of the BEC production process. During the writing of this thesis, a Limited Individual Lifetime Differential Evolution (LILDE) [142] algorithm has been implemented, which is an advancement of the Differential Evolution (DE) [143, 144] algorithm that improves the performance under noisy conditions. The DE algorithm represents a promising tool to further improve the performance of the experimental apparatus. The performance of the apparatus can be evaluated by the concept of the cost function, which compares and tries to minimize the error between the predicted and actual output of the model. In the Hybrid evaporation scheme, a suitable cost function for optimizing the flux in the 3D-MOT loading phase would incorporate, for example, the optical power and frequency as well as the magnetic field gradients of the $2D^+$- and 3D-MOT as inputs, while the output would be a maximum atom number in the 3D-MOT and minimum time. Similarly, the optimization of the quadrupole and optical dipole trap evaporation steps would include the magnetic field gradient, the microwave frequency and power as well as the optical laser power and timings. In the case of all optical evaporation, additional input parameters would be the CPM frequency. A possible cost function for the BEC generation could incorporate the ratio between the number of atoms N in a BEC and the cycle time t

$$f(N,t) = \begin{cases} \frac{N}{t} & N < 10^4 \\ \frac{10^4}{t} & N \geq 10^4 \end{cases},$$

which first tries to increase the ratio until reaching a reasonable number of 10^4 atoms[1], after which it starts to only optimize for the cycle time. However, this simple cost function does not discriminate between optimizing for a high bandwidth (fast cycle time) or a high interferometric sensitivity (large atom number). Therefore, the cost function needs to be adjusted for the specific application.

6.2 Improving the new detection system

The new detection system lies at the heart of number-stabilized preparation and accurate detection of ultracold atomic ensembles. Both tasks require a high single-atom resolution limit, ideally larger than the prepared or detected number of atoms. One of the main reasons for the revision of the detection system was motivated by its inconsistent operation and almost daily maintenance routine. The replacement of the free-space optics by optical fibers brought more spatial as well as temporal stability and made the detection system a reliable tool. However, the final characterization of the new detection system with respect to the resolution limit is still pending. A full calibration measurement will help to identify and characterize noise sources as described in Section 4.1.3. The results of the preliminary single-atom counting measurements assume a technical intensity noise that deteriorates the resolution with increasing background signal. However, a first optimization attempt yielded a reduced background offset noise that caused a significant reduction in the widths of the atom number distributions. This optimistic result is pointing towards a potentially higher detection limit. Furthermore, the high background offset levels could be decreased to a minimum by an improved blocking scheme for the straylight contributions of the MOT beams. For this, small circular beam blocks can be placed close to the k-space plane of the object to filter out any straylight originating with a definite direction. Alternatively, the electronics for the intensity stabilization should be checked to eliminate noise sources imprinted on the cooling light. Out-of-loop photodiodes for the collimator holders could be implemented to monitor the intensity for long-term drifts.

One of the main benefits of the detection system will be to harness the potential gain in sensitivity of Heisenberg-limited atom interferometry. The single-particle resolved counting of the atom numbers in the interferometer output will eliminate the technical detection noise. More importantly, the interferometric sequence generally requires the detection of two output modes. A major flaw of the detection setup is that it prevents the simultaneous state selective detection of the atoms in different hyperfine levels and sublevels, since the cooling and repumping beams will pump the atoms from $|F = 1, m_F\rangle$ to $|F = 2, m_F\rangle$

---

[1] The finite atom number may be limited due to density effects or technical detection noise.

and leave them distributed over all sublevels due to the circular polarization components immediately after only a few transition cycles. However, there are two options that can be considered for the state selective detection to be tested: the atoms can either be detected sequentially or by spatial separation of the different sublevels. The first option would require to push all other remaining atoms out of the dipole trap and repeatedly measure each component one after the other, which adds more time to the experimental cycle. The second approach is realized by an inhomogeneous magnetic field that is produced by a Stern-Gerlach coil. For this, the detection MOT would need to be replaced by a molasses instead, since the quadrupole field would reverse the separation of the components. As a fact, the distance of the separated components needs to be much smaller than the Gaussian beam diameters for approximately uniform illumination. At the current state, the presented detection setup does not yet involve the counting of atoms inside the MOT, while discriminating their internal state. Therefore, extending the detection to more than one output port would open even more possible applications. The goal is to first spatially separate and second simultaneously trap atomic ensembles with different internal states. Two methods have been demonstrated for the spatial splitting and a subsequent state-selective detection of atomic ensembles. The first method incorporates a blue-detuned laser beam (light-sheet), which is focused onto the center of a MOT, filled with ^{87}Rb atoms [145]. The blue-detuned laser introduces a repulsive force, which acts as a barrier between a double-well potential. However, the AC-Stark shift also disturbs the energy levels used to Doppler-cool the ensembles, thereby limiting the lifetime of the atoms. This is compensated by alternate switching of the blue-detuned laser light and MOT beams. In this configuration single atoms in different internal hyperfine states were counted up to 500. A second method employed spin resolved detection of sodium atoms from a BEC by a three-dimensional optical molasses with a duration of 5 ms and thereby bypassing the retrapping of the atoms [146]. The cloud containing the three spin components of the $F = 1$ hyperfine manifold is splitted by applying a Stern-Gerlach pulse, where the adjacent clouds are well separated by 1.3 mm. The demonstrated sensitivity $\Delta N = 1.6$ of the detection scheme comes close to the single-atom resoluion limit. However, this technique is limited to photon shot noise, due to very low interrogation times and consequently less signal.

Besides the detection of the interferometer output, the input states also need to be precisely determined. Typical input states, such as coherent spin states, spin-squeezed states or Twin-Fock states are characterized and identified by their respective number distributions. Here, the detection system will be used for a high-fidelity tomography of pursued entangled quantum states. One particular example is the Twin-Fock state with equal number occupations $|N/2\rangle_{+1}|N/2\rangle_{-1}$ in each of the modes ±1. Coupling the two with a $\pi/2$ coupling pulse leads to a peculiar probability distribution of the individual modes, where each one only contains an even number of atoms. The $\pi/2$ coupling pulse is the realization of a beam splitter for the inernal atomic spin states and can be therefore regarded as a generalized Hong-Ou-Mandel experiment for the underlying entangled atoms.

Bibliography

1. W. Heisenberg: ‘Die Entwicklung der Quantentheorie 1918-1928’. *Naturwissenschaften* (1929), vol. 17(26). doi: `10.1007/BF01505682`.
2. L. D. Broglie: ‘Waves and Quanta’. *Nature* (1923), vol. 112. doi: `10.1038/112540a0`.
3. A. Einstein: ‘Quantentheorie des idealen einatomigen Gases II’. *Sitzber. Kgl. Preuss. Akad. Wiss., Phys. Math. Kl. Bericht* (1925), vol. 3. doi: `10.1002/3527608958.ch28`.
4. A. G. J. MacFarlane, J. P. Dowling, and G. J. Milburn: ‘Quantum technology: the second quantum revolution’. *Philosophical Transactions of the Royal Society of London. Series A: Mathematical, Physical and Engineering Sciences* (2003), vol. 361(1809). doi: `10.1098/rsta.2003.1227`.
5. M. Kasevich and S. Chu: ‘Measurement of the Gravitational Acceleration of an Atom with a Light-Pulse Atom Interferometer’. *Applied Physics B Photophysics and Laser Chemistry* (1992), vol. 54(5). doi: `10.1007/BF00325375`.
6. Z.-K. Hu, B.-L. Sun, X.-C. Duan, M.-K. Zhou, L.-L. Chen, S. Zhan, Q.-Z. Zhang, and J. Luo: ‘Demonstration of an Ultrahigh-Sensitivity Atom-Interferometry Absolute Gravimeter’. *Physical Review A* (2013), vol. 88(4). doi: `10.1103/PhysRevA.88.043610`.
7. G. W. Biedermann, X. Wu, L. Deslauriers, S. Roy, C. Mahadeswaraswamy, and M. A. Kasevich: ‘Testing Gravity with Cold-Atom Interferometers’. *Physical Review A* (2015), vol. 91(3). doi: `10.1103/PhysRevA.91.033629`.
8. T. L. Gustavson, P. Bouyer, and M. A. Kasevich: ‘Precision Rotation Measurements with an Atom Interferometer Gyroscope’. *Physical Review Letters* (1997), vol. 78(11). doi: `10.1103/PhysRevLett.78.2046`.
9. A. Gauguet, B. Canuel, T. Lévèque, W. Chaibi, and A. Landragin: ‘Characterization and Limits of a Cold-Atom Sagnac Interferometer’. *Physical Review A* (2009), vol. 80(6). doi: `10.1103/PhysRevA.80.063604`.
10. J. K. Stockton, K. Takase, and M. A. Kasevich: ‘Absolute Geodetic Rotation Measurement Using Atom Interferometry’. *Physical Review Letters* (2011), vol. 107(13). doi: `10.1103/PhysRevLett.107.133001`.

11. G. Tackmann, P. Berg, C. Schubert, S. Abend, M. Gilowski, W. Ertmer, and E. M. Rasel: 'Self-Alignment of a Compact Large-Area Atomic Sagnac Interferometer'. *New Journal of Physics* (2012), vol. 14(1). doi: `10.1088/1367-2630/14/1/015002`.
12. I. K. Kominis, T. W. Kornack, J. C. Allred, and M. V. Romalis: 'A Subfemtotesla Multichannel Atomic Magnetometer'. *Nature* (2003), vol. 422(6932). doi: `10.1038/nature01484`.
13. B. J. Bloom, T. L. Nicholson, J. R. Williams, S. L. Campbell, M. Bishof, X. Zhang, W. Zhang, S. L. Bromley, and J. Ye: 'An Optical Lattice Clock with Accuracy and Stability at the 10-18 Level'. *Nature* (2014), vol. 506(7486). doi: `10.1038/nature12941`.
14. O. Hosten, N. J. Engelsen, R. Krishnakumar, and M. A. Kasevich: 'Measurement Noise 100 Times Lower than the Quantum-Projection Limit Using Entangled Atoms'. *Nature* (2016), vol. 529(7587). doi: `10.1038/nature16176`.
15. L. Pezzè, A. Smerzi, M. K. Oberthaler, R. Schmied, and P. Treutlein: 'Quantum metrology with nonclassical states of atomic ensembles'. *Rev. Mod. Phys.* (2018), vol. 90. doi: `10.1103/RevModPhys.90.035005`.
16. B. P. Abbott et al.: 'Observation of Gravitational Waves from a Binary Black Hole Merger'. *Phys. Rev. Lett.* (2016), vol. 116. doi: `10.1103/PhysRevLett.116.061102`.
17. J. Aasi et al.: 'Enhanced sensitivity of the LIGO gravitational wave detector by using squeezed states of light'. *Nature Photonics* (2013), vol. 7(8). doi: `10.1038/nphoton.2013.177`.
18. J. Lough et al.: 'First Demonstration of 6 dB Quantum Noise Reduction in a Kilometer Scale Gravitational Wave Observatory'. *Phys. Rev. Lett.* (2021), vol. 126. doi: `10.1103/PhysRevLett.126.041102`.
19. C. A. Sackett, D. Kielpinski, B. E. King, C. Langer, V. Meyer, C. J. Myatt, M. Rowe, Q. A. Turchette, W. M. Itano, D. J. Wineland, and C. Monroe: 'Experimental Entanglement of Four Particles'. *Nature* (2000), vol. 404(6775). doi: `10.1038/35005011`.
20. V. Meyer, M. A. Rowe, D. Kielpinski, C. A. Sackett, W. M. Itano, C. Monroe, and D. J. Wineland: 'Experimental Demonstration of Entanglement-Enhanced Rotation Angle Estimation Using Trapped Ions'. *Physical Review Letters* (2001), vol. 86(26). doi: `10.1103/PhysRevLett.86.5870`.
21. D. Leibfried, B. DeMarco, V. Meyer, D. Lucas, M. Barrett, J. Britton, W. M. Itano, B. Jelenković, C. Langer, T. Rosenband, and D. J. Wineland: 'Experimental Demonstration of a Robust, High-Fidelity Geometric Two Ion-Qubit Phase Gate'. *Nature* (2003), vol. 422(6930). doi: `10.1038/nature01492`.
22. D. Leibfried, M. Barrett, T. Schaetz, J. Britton, J. Chiaverini, W. M. Itano, J. D. Jost, C. Langer, and D. J. Wineland: 'Toward Heisenberg-Limited Spectroscopy with Multiparticle Entangled States'. *Science* (2004), vol. 304(5676). doi: `10.1126/science.1097576`.

23. D. Leibfried, E. Knill, S. Seidelin, J. Britton, R. B. Blakestad, J. Chiaverini, D. B. Hume, W. M. Itano, J. D. Jost, C. Langer, R. Ozeri, R. Reichle, and D. J. Wineland: ‘Creation of a Six-Atom ‘Schrödinger Cat’ State’. *Nature* (2005), vol. 438(7068). doi: `10.1038/nature04251`.

24. T. Monz, P. Schindler, J. T. Barreiro, M. Chwalla, D. Nigg, W. A. Coish, M. Harlander, W. Hänsel, M. Hennrich, and R. Blatt: ‘14-Qubit Entanglement: Creation and Coherence’. *Physical Review Letters* (2011), vol. 106(13). doi: `10.1103/PhysRevLett.106.130506`.

25. J. G. Bohnet, B. C. Sawyer, J. W. Britton, M. L. Wall, A. M. Rey, M. Foss-Feig, and J. J. Bollinger: ‘Quantum Spin Dynamics and Entanglement Generation with Hundreds of Trapped Ions’. *Science* (2016), vol. 352(6291). doi: `10.1126/science.aad9958`.

26. J. Appel, P. J. Windpassinger, D. Oblak, U. B. Hoff, N. Kj\a ergaard, and E. S. Polzik: ‘Mesoscopic Atomic Entanglement for Precision Measurements beyond the Standard Quantum Limit’. *Proceedings of the National Academy of Sciences* (2009), vol. 106(27). doi: `10.1073/pnas.0901550106`.

27. I. D. Leroux, M. H. Schleier-Smith, and V. Vuletić: ‘Implementation of Cavity Squeezing of a Collective Atomic Spin’. *Physical Review Letters* (2010), vol. 104(7). doi: `10.1103/PhysRevLett.104.073602`.

28. I. D. Leroux, M. H. Schleier-Smith, and V. Vuletić: ‘Orientation-Dependent Entanglement Lifetime in a Squeezed Atomic Clock’. *Physical Review Letters* (2010), vol. 104(25). doi: `10.1103/PhysRevLett.104.250801`.

29. A. Louchet-Chauvet, J. Appel, J. J. Renema, D. Oblak, N. Kjaergaard, and E. S. Polzik: ‘Entanglement-Assisted Atomic Clock beyond the Projection Noise Limit’. *New Journal of Physics* (2010), vol. 12(6). doi: `10.1088/1367-2630/12/6/065032`.

30. M. H. Schleier-Smith, I. D. Leroux, and V. Vuletić: ‘States of an Ensemble of Two-Level Atoms with Reduced Quantum Uncertainty’. *Physical Review Letters* (2010), vol. 104(7). doi: `10.1103/PhysRevLett.104.073604`.

31. Z. Chen, J. G. Bohnet, S. R. Sankar, J. Dai, and J. K. Thompson: ‘Conditional Spin Squeezing of a Large Ensemble via the Vacuum Rabi Splitting’. *Physical Review Letters* (2011), vol. 106(13). doi: `10.1103/PhysRevLett.106.133601`.

32. R. J. Sewell, M. Koschorreck, M. Napolitano, B. Dubost, N. Behbood, and M. W. Mitchell: ‘Magnetic Sensitivity Beyond the Projection Noise Limit by Spin Squeezing’. *Physical Review Letters* (2012), vol. 109(25). doi: `10.1103/PhysRevLett.109.253605`.

33. J. G. Bohnet, K. C. Cox, M. A. Norcia, J. M. Weiner, Z. Chen, and J. K. Thompson: ‘Reduced Spin Measurement Back-Action for a Phase Sensitivity Ten Times beyond the Standard Quantum Limit’. *Nature Photonics* (2014), vol. 8(9). doi: `10.1038/nphoton.2014.151`.

34. R. J. Sewell, M. Napolitano, N. Behbood, G. Colangelo, F. Martin Ciurana, and M. W. Mitchell: 'Ultrasensitive Atomic Spin Measurements with a Nonlinear Interferometer'. *Physical Review X* (2014), vol. 4(2). doi: `10.1103/PhysRevX.4.021045`.
35. G. Barontini, L. Hohmann, F. Haas, J. Estève, and J. Reichel: 'Deterministic Generation of Multiparticle Entanglement by Quantum Zeno Dynamics'. *Science* (2015), vol. 349(6254). doi: `10.1126/science.aaa0754`.
36. K. C. Cox, G. P. Greve, J. M. Weiner, and J. K. Thompson: 'Deterministic Squeezed States with Collective Measurements and Feedback'. *Physical Review Letters* (2016), vol. 116(9). doi: `10.1103/PhysRevLett.116.093602`.
37. J. Estève, C. Gross, A. Weller, S. Giovanazzi, and M. K. Oberthaler: 'Squeezing and Entanglement in a Bose–Einstein Condensate'. *Nature* (2008), vol. 455(7217). doi: `10.1038/nature07332`.
38. C. Gross, T. Zibold, E. Nicklas, J. Estève, and M. K. Oberthaler: 'Nonlinear Atom Interferometer Surpasses Classical Precision Limit'. *Nature* (2010), vol. 464(7292). doi: `10.1038/nature08919`.
39. M. F. Riedel, P. Böhi, Y. Li, T. W. Hänsch, A. Sinatra, and P. Treutlein: 'Atom-Chip-Based Generation of Entanglement for Quantum Metrology'. *Nature* (2010), vol. 464(7292). doi: `10.1038/nature08988`.
40. C. D. Hamley, C. S. Gerving, T. M. Hoang, E. M. Bookjans, and M. S. Chapman: 'Spin-Nematic Squeezed Vacuum in a Quantum Gas'. *Nature Physics* (2012), vol. 8(4). doi: `10.1038/nphys2245`.
41. T. Berrada, S. van Frank, R. Bücker, T. Schumm, J.-F. Schaff, and J. Schmiedmayer: 'Integrated Mach–Zehnder Interferometer for Bose–Einstein Condensates'. *Nature Communications* (2013), vol. 4. doi: `10.1038/ncomms3077`.
42. C. F. Ockeloen, R. Schmied, M. F. Riedel, and P. Treutlein: 'Quantum Metrology with a Scanning Probe Atom Interferometer'. *Phys. Rev. Lett.* (2013), vol. 111. doi: `10.1103/PhysRevLett.111.143001`.
43. H. Strobel, W. Muessel, D. Linnemann, T. Zibold, D. B. Hume, L. Pezzè, A. Smerzi, and M. K. Oberthaler: 'Fisher Information and Entanglement of Non-Gaussian Spin States'. *Science* (2014), vol. 345(6195). doi: `10.1126/science.1250147`.
44. W. Muessel, H. Strobel, D. Linnemann, T. Zibold, B. Juliá-Díaz, and M. K. Oberthaler: 'Twist-and-Turn Spin Squeezing in Bose-Einstein Condensates'. *Physical Review A* (2015), vol. 92(2). doi: `10.1103/PhysRevA.92.023603`.
45. I. Kruse, K. Lange, J. Peise, B. Lücke, L. Pezzè, J. Arlt, W. Ertmer, C. Lisdat, L. Santos, A. Smerzi, and C. Klempt: 'Improvement of an Atomic Clock using Squeezed Vacuum'. *Phys. Rev. Lett.* (2016), vol. 117. doi: `10.1103/PhysRevLett.117.143004`.

46. Y.-Q. Zou, L.-N. Wu, Q. Liu, X.-Y. Luo, S.-F. Guo, J.-H. Cao, M. K. Tey, and L. You: 'Beating the Classical Precision Limit with Spin-1 Dicke States of More than 10,000 Atoms'. *Proceedings of the National Academy of Sciences* (2018), vol. 115(25). doi: `10.1073/pnas.1715105115`.

47. B. Lücke, J. Peise, G. Vitagliano, J. Arlt, L. Santos, G. Tóth, and C. Klempt: 'Detecting Multiparticle Entanglement of Dicke States'. *Physical review letters* (2014), vol. 112(15). doi: `10.1103/PhysRevLett.112.155304`.

48. J. Peise, I. Kruse, K. Lange, B. Lücke, L. Pezzè, J. Arlt, W. Ertmer, K. Hammerer, L. Santos, A. Smerzi, and C. Klempt: 'Satisfying the Einstein–Podolsky–Rosen Criterion with Massive Particles'. *Nature Communications* (2015), vol. 6(1). doi: `10.1038/ncomms9984`.

49. W. Muessel, H. Strobel, D. Linnemann, D. B. Hume, and M. K. Oberthaler: 'Scalable Spin Squeezing for Quantum-Enhanced Magnetometry with Bose-Einstein Condensates'. *Phys. Rev. Lett.* (2014), vol. 113. doi: `10.1103/PhysRevLett.113.103004`.

50. C. Gross: 'Spin Squeezing, Entanglement and Quantum Metrology with Bose–Einstein Condensates'. *J. Phys. B: At., Mol. Opt. Phys.* (2012), vol. 45(10). doi: `10.1088/0953-4075/45/10/103001`.

51. B. Lücke, M. Scherer, J. Kruse, L. Pezzé, F. Deuretzbacher, P. Hyllus, O. Topic, J. Peise, W. Ertmer, J. Arlt, L. Santos, A. Smerzi, and C. Klempt: 'Twin Matter Waves for Interferometry Beyond the Classical Limit'. *Science* (2011), vol. 334(6057). doi: `10.1126/science.1208798`.

52. D. M. Stamper-Kurn and M. Ueda: 'Spinor Bose gases: Symmetries, magnetism, and quantum dynamics'. *Rev. Mod. Phys.* (2013), vol. 85. doi: `10.1103/RevModPhys.85.1191`.

53. M. Vengalattore, J. M. Higbie, S. R. Leslie, J. Guzman, L. E. Sadler, and D. M. Stamper-Kurn: 'High-Resolution Magnetometry with a Spinor Bose-Einstein Condensate'. *Phys. Rev. Lett.* (2007), vol. 98. doi: `10.1103/PhysRevLett.98.200801`.

54. K. Lange, J. Peise, B. Lücke, I. Kruse, G. Vitagliano, I. Apellaniz, M. Kleinmann, G. Tóth, and C. Klempt: 'Entanglement between two spatially separated atomic modes'. *Science* (2018), vol. 360(6387). doi: `10.1126/science.aao2035`.

55. M. Fadel, T. Zibold, B. Décamps, and P. Treutlein: 'Spatial entanglement patterns and Einstein-Podolsky-Rosen steering in Bose-Einstein condensates'. *Science* (2018), vol. 360(6387). doi: `10.1126/science.aao1850`.

56. P. Kunkel, M. Prüfer, H. Strobel, D. Linnemann, A. Frölian, T. Gasenzer, M. Gärttner, and M. K. Oberthaler: 'Spatially distributed multipartite entanglement enables EPR steering of atomic clouds'. *Science* (2018), vol. 360(6387). doi: `10.1126/science.aao2254`.

57. F. Anders et al.: ‘Momentum Entanglement for Atom Interferometry’. *Phys. Rev. Lett.* (2021), vol. 127. doi: `10.1103/PhysRevLett.127.140402`.
58. M. Horikoshi and K. Nakagawa: ‘Atom chip based fast production of Bose–Einstein condensate’. *Applied Physics B* (2006), vol. 82(3). doi: `10.1007/s00340-005-2083-z`.
59. D. M. Farkas, K. M. Hudek, E. A. Salim, S. R. Segal, M. B. Squires, and D. Z. Anderson: ‘A compact, transportable, microchip-based system for high repetition rate production of Bose–Einstein condensates’. *Applied Physics Letters* (2010), vol. 96(9). doi: `10.1063/1.3327812`.
60. D. M. Farkas, E. A. Salim, and J. Ramirez-Serrano: ‘Production of Rubidium Bose-Einstein Condensates at a 1 Hz Rate’. *arXiv:1403.4641 [physics.atom-ph]* (2014), vol. doi: `10.48550/arXiv.1403.4641`.
61. J. Rudolph, W. Herr, C. Grzeschik, T. Sternke, A. Grote, M. Popp, D. Becker, H. Müntinga, H. Ahlers, A. Peters, C. Lämmerzahl, K. Sengstock, N. Gaaloul, W. Ertmer, and E. M. Rasel: ‘A high-flux BEC source for mobile atom interferometers’. *New Journal of Physics* (2015), vol. 17(6). doi: `10.1088/1367-2630/17/6/065001`.
62. S. Abend, M. Gebbe, M. Gersemann, H. Ahlers, H. Müntinga, E. Giese, N. Gaaloul, C. Schubert, C. Lämmerzahl, W. Ertmer, W. P. Schleich, and E. M. Rasel: ‘Atom-Chip Fountain Gravimeter’. *Physical Review Letters* (2016), vol. 117(20). doi: `10.1103/PhysRevLett.117.203003`.
63. Y.-J. Lin, A. R. Perry, R. L. Compton, I. B. Spielman, and J. V. Porto: ‘Rapid production of ^{87}Rb Bose-Einstein condensates in a combined magnetic and optical potential’. *Phys. Rev. A* (2009), vol. 79. doi: `10.1103/PhysRevA.79.063631`.
64. M. Zaiser, J. Hartwig, D. Schlippert, U. Velte, N. Winter, V. Lebedev, W. Ertmer, and E. M. Rasel: ‘Simple method for generating Bose-Einstein condensates in a weak hybrid trap’. (2011), vol. 83. doi: `10.1103/PhysRevA.83.035601`.
65. Q. Bouton, R. Chang, A. L. Hoendervanger, F. Nogrette, A. Aspect, C. I. Westbrook, and D. Clément: ‘Fast production of Bose-Einstein condensates of metastable helium’. *Physical Review A* (2015), vol. 91(6). doi: `10.1103/PhysRevA.91.061402`.
66. M. D. Barrett, J. A. Sauer, and M. S. Chapman: ‘All-Optical Formation of an Atomic Bose-Einstein Condensate’. *Physical Review Letters* (2001), vol. 87(1). doi: `10.1103/PhysRevLett.87.010404`.
67. T. Kinoshita, T. Wenger, and D. S. Weiss: ‘All-optical Bose-Einstein condensation using a compressible crossed dipole trap’. *Physical Review A* (2005), vol. 71(1). doi: `10.1103/PhysRevA.71.011602`.

68. J.-F. Clément, J.-P. Brantut, M. Robert-de-Saint-Vincent, R. A. Nyman, A. Aspect, T. Bourdel, and P. Bouyer: 'All-optical runaway evaporation to Bose-Einstein condensation'. *Physical Review A* (2009), vol. 79(6). doi: `10.1103/PhysRevA.79.061406`.

69. M. Landini, S. Roy, G. Roati, A. Simoni, M. Inguscio, G. Modugno, and M. Fattori: 'Direct evaporative cooling of ^{39}K atoms to Bose-Einstein condensation'. *Physical Review A* (2012), vol. 86(3). doi: `10.1103/PhysRevA.86.033421`.

70. S. Stellmer, R. Grimm, and F. Schreck: 'Production of quantum-degenerate strontium gases'. *Physical Review A* (2013), vol. 87(1). doi: `10.1103/PhysRevA.87.013611`.

71. R. Roy, A. Green, R. Bowler, and S. Gupta: 'Rapid cooling to quantum degeneracy in dynamically shaped atom traps'. *Physical Review A* (2016), vol. 93(4). doi: `10.1103/PhysRevA.93.043403`.

72. D. Xie, D. Wang, W. Gou, W. Bu, and B. Yan: 'Fast production of rubidium Bose-Einstein condensate in a dimple trap'. *JOSA B* (2018), vol. 35(3). doi: `10.1364/JOSAB.35.000500`.

73. G. Condon, M. Rabault, B. Barrett, L. Chichet, R. Arguel, H. Eneriz-Imaz, D. Naik, A. Bertoldi, B. Battelier, P. Bouyer, and A. Landragin: 'All-Optical Bose-Einstein Condensates in Microgravity'. *Physical Review Letters* (2019), vol. 123(24). doi: `10.1103/PhysRevLett.123.240402`.

74. K. B. Davis, M. .-.-O. Mewes, M. R. Andrews, N. J. van Druten, D. S. Durfee, D. M. Kurn, and W. Ketterle: 'Bose-Einstein Condensation in a Gas of Sodium Atoms'. *Phys. Rev. Lett.* (1995), vol. 75. doi: `10.1103/PhysRevLett.75.3969`.

75. U. Ernst, A. Marte, F. Schreck, J. Schuster, and G. Rempe: 'Bose-Einstein condensation in a pure Ioffe-Pritchard field configuration'. *EPL (Europhysics Letters)* (1998), vol. 41(1). doi: `10.1209/epl/i1998-00107-2`.

76. J. Arlt, O. Maragò, E. Hodby, S. A. Hopkins, G. Hechenblaikner, S. Webster, and C. J. Foot: 'Bose-Einstein condensation in a rotating anisotropic TOP trap'. *Journal of Physics B: Atomic, Molecular and Optical Physics* (1999), vol. 32(24). doi: `10.1088/0953-4075/32/24/320`.

77. H. Albers: 'Time-Averaged Optical Potentials for Creating and Shaping Bose-EinsteinCondensates'. PhD thesis. Gottfried Wilhelm Leibniz Universität Hannover, (2020). doi: `10.15488/10073`.

78. M. H. Anderson, J. R. Ensher, M. R. Matthews, C. E. Wieman, and E. A. Cornell: 'Observation of Bose-Einstein Condensation in a Dilute Atomic Vapor'. *Science* (1995), vol. 269(5221). doi: `10.1126/science.269.5221.198`.

79. D. M. Brink and C. V. Sukumar: 'Majorana spin-flip transitions in a magnetic trap'. *Phys. Rev. A* (2006), vol. 74. doi: `10.1103/PhysRevA.74.035401`.

80. D.-F. Zhang, T.-Y. Gao, L.-R. Kong, K. Li, and K.-J. Jiang: ‘Production of Rubidium Bose–Einstein Condensate in an Optically Plugged Magnetic Quadrupole Trap’. *Chinese Physics Letters* (2016), vol. 33(07). doi: `10.1088/0256-307X/33/7/076701`.

81. W. Petrich, M. H. Anderson, J. R. Ensher, and E. A. Cornell: ‘Stable, Tightly Confining Magnetic Trap for Evaporative Cooling of Neutral Atoms’. *Phys. Rev. Lett.* (1995), vol. 74. doi: `10.1103/PhysRevLett.74.3352`.

82. D. E. Pritchard: ‘Cooling Neutral Atoms in a Magnetic Trap for Precision Spectroscopy’. *Phys. Rev. Lett.* (1983), vol. 51. doi: `10.1103/PhysRevLett.51.1336`.

83. T. Esslinger, I. Bloch, and T. W. Hänsch: ‘Bose-Einstein condensation in a quadrupole-Ioffe-configuration trap’. *Phys. Rev. A* (1998), vol. 58. doi: `10.1103/PhysRevA.58.R2664`.

84. W. Tino, H. Jens, M. Michael, N. Hanns-Christoph, and G. Rudolf: ‘Bose-Einstein Condensation of Cesium’. *Science* (2003), vol. 299(5604). doi: `10.1126/science.1079699`.

85. D. Comparat, A. Fioretti, G. Stern, E. Dimova, B. L. Tolra, and P. Pillet: ‘Optimized production of large Bose-Einstein condensates’. *Phys. Rev. A* (2006), vol. 73. doi: `10.1103/PhysRevA.73.043410`.

86. S. B. Hill and J. J. McClelland: ‘Atoms on demand: Fast, deterministic production of single Cr atoms’. *Applied Physics Letters* (2003), vol. 82(18). doi: `10.1063/1.1572539`.

87. S. B. Hill and J. J. McClelland: ‘Performance of a feedback-controlled, deterministic source of single chromium atoms’. *J. Opt. Soc. Am. B* (2004), vol. 21(3). doi: `10.1364/JOSAB.21.000473`.

88. A. Hüper: ‘Accurate atom counting for entanglement-enhanced atom interferometry’. PhD thesis. Gottfried Wilhelm Leibniz Universität Hannover, (2019). doi: `10.15488/9830`.

89. B. Roy and M. Scholten: ‘High-flux cold rubidium atomic beam for strongly-coupled cavity QED’. *Journal of the Korean Physical Society* (2012), vol. 61(3). doi: `10.3938/jkps.61.359`.

90. S. Chaudhuri, S. Roy, and C. S. Unnikrishnan: ‘Realization of an intense cold Rb atomic beam based on a two-dimensional magneto-optical trap: Experiments and comparison with simulations’. *Phys. Rev. A* (2006), vol. 74. doi: `10.1103/PhysRevA.74.023406`.

91. S. Jöllenbeck, J. Mahnke, R. Randoll, W. Ertmer, J. Arlt, and C. Klempt: ‘Hexapole-compensated magneto-optical trap on a mesoscopic atom chip’. *Phys. Rev. A* (2011), vol. 83. doi: `10.1103/PhysRevA.83.043406`.

92. X. Baillard, A. Gauguet, S. Bize, P. Lemonde, P. Laurent, A. Clairon, and P. Rosenbusch: 'Interference-filter-stabilized external-cavity diode lasers'. *Optics Communications* (2006), vol. 266(2). doi: `https://doi.org/10.1016/j.optcom.2006.05.011`.

93. D. J. McCarron, S. A. King, and S. L. Cornish: 'Modulation transfer spectroscopy in atomic rubidium'. *Measurement Science and Technology* (2008), vol. 19(10). doi: `10.1088/0957-0233/19/10/105601`.

94. U. Schünemann, H. Engler, R. Grimm, M. Weidemüller, and M. Zielonkowski: 'Simple scheme for tunable frequency offset locking of two lasers'. *Review of Scientific Instruments* (1999), vol. 70(1). doi: `10.1063/1.1149573`.

95. B. Meyer, A. Idel, F. Anders, J. Peise, and C. Klempt: 'Dynamical low-noise microwave source for cold atom experiments'. *arXiv: 2003.10989 [quant-ph]* (2020), vol. doi: `10.48550/arXiv.2003.10989`.

96. B. Meyer: 'Versatile, Low-Phase-Noise Microwave Source for Cold 87Rb Experiments'. MA thesis. Institut für Quantenoptik, (2020).

97. M. Greiner, I. Bloch, T. W. Hänsch, and T. Esslinger: 'Magnetic transport of trapped cold atoms over a large distance'. *Phys. Rev. A* (2001), vol. 63. doi: `10.1103/PhysRevA.63.031401`.

98. B. Sheard: 'Magnetic transport and Bose-Einstein condensation of rubidium atoms'. PhD thesis. University of Oxford, (2010).

99. H. J. Lewandowski, D. M. Harber, D. L. Whitaker, and E. A. Cornell: 'Simplified System for Creating a Bose-Einstein Condensate'. *Journal of Low Temperature Physics* (2003), vol. 132(5). doi: `10.1023/A:1024800600621`.

100. W. D. Phillips and H. Metcalf: 'Laser Deceleration of an Atomic Beam'. *Phys. Rev. Lett.* (1982), vol. 48. doi: `10.1103/PhysRevLett.48.596`.

101. W. Ertmer, R. Blatt, J. L. Hall, and M. Zhu: 'Laser Manipulation of Atomic Beam Velocities: Demonstration of Stopped Atoms and Velocity Reversal'. *Phys. Rev. Lett.* (1985), vol. 54. doi: `10.1103/PhysRevLett.54.996`.

102. K. Dieckmann, R. J. C. Spreeuw, M. Weidemüller, and J. T. M. Walraven: 'Two-dimensional magneto-optical trap as a source of slow atoms'. *Phys. Rev. A* (1998), vol. 58. doi: `10.1103/PhysRevA.58.3891`.

103. C. Slowe, L. Vernac, and L. V. Hau: 'High flux source of cold rubidium atoms'. *Review of Scientific Instruments* (2005), vol. 76(10). doi: `10.1063/1.2069651`.

104. J. Schoser, A. Batär, R. Löw, V. Schweikhard, A. Grabowski, Y. B. Ovchinnikov, and T. Pfau: 'Intense source of cold Rb atoms from a pure two-dimensional magneto-optical trap'. *Phys. Rev. A* (2002), vol. 66. doi: `10.1103/PhysRevA.66.023410`.

105. H. J. Metcalf and P. van der Straten: 'Laser cooling and trapping of atoms'. *J. Opt. Soc. Am. B* (2003), vol. 20(5). doi: `10.1364/JOSAB.20.000887`.

106. T. Hänsch and A. Schawlow: 'Cooling of gases by laser radiation'. *Optics Communications* (1975), vol. 13(1). doi: `https://doi.org/10.1016/0030-4018(75)90159-5`.

107. J. Mahnke: 'A continuously pumped reservoir of ultracold atoms'. PhD thesis. Gottfried Wilhelm Leibniz Universität Hannover, (2015). doi: `10.15488/8526`.

108. Y. B. Ovchinnikov: 'Compact magneto-optical sources of slow atoms'. *Optics Communications* (2005), vol. 249(4). doi: `https://doi.org/10.1016/j.optcom.2005.01.047`.

109. S. Jöllenbeck: 'Eine Quelle Bose-Einstein-kondensierter Ensembles auf Basis eines mesoskopischen Atomchips'. PhD thesis. Gottfried Wilhelm Leibniz Universität Hannover, (2012). doi: `10.15488/7872`.

110. T. Walker, D. Sesko, and C. Wieman: 'Collective behavior of optically trapped neutral atoms'. *Phys. Rev. Lett.* (1990), vol. 64. doi: `10.1103/PhysRevLett.64.408`.

111. D. W. Sesko, T. G. Walker, and C. E. Wieman: 'Behavior of neutral atoms in a spontaneous force trap'. *J. Opt. Soc. Am. B* (1991), vol. 8(5). doi: `10.1364/JOSAB.8.000946`.

112. G. L. Gattobigio, T. Pohl, G. Labeyrie, and R. Kaiser: 'Scaling laws for large magneto-optical traps'. *Physica Scripta* (2010), vol. 81(2). doi: `10.1088/0031-8949/81/02/025301`.

113. S. Earnshaw: 'On the nature of the molecular forces which regulate the constitution of the luminiferous ether'. *Transactions of the Cambridge Philosophical Society* (1848), vol. 7.

114. J. Pérez-Ríos and A. S. Sanz: 'How does a magnetic trap work?' *American Journal of Physics* (2013), vol. 81(11). doi: `10.1119/1.4819167`.

115. J. Dalibard and C. Cohen-Tannoudji: 'Laser cooling below the Doppler limit by polarization gradients: simple theoretical models'. *J. Opt. Soc. Am. B* (1989), vol. 6(11). doi: `10.1364/JOSAB.6.002023`.

116. P. D. Lett, W. D. Phillips, S. L. Rolston, C. E. Tanner, R. N. Watts, and C. I. Westbrook: 'Optical molasses'. *J. Opt. Soc. Am. B* (1989), vol. 6(11). doi: `10.1364/JOSAB.6.002084`.

117. W. Ketterle, D. S. Durfee, and D. Stamper-Kurn: 'Making, probing and understanding Bose-Einstein condensates'. *arXiv:cond-mat/9904034* (1999), vol. doi: `10.48550/arXiv.cond-mat/9904034`.

118. P. O. Schmidt, S. Hensler, J. Werner, T. Binhammer, A. G rlitz, and T. Pfau: 'Continuous loading of cold atoms into a Ioffe Pritchard magnetic trap'. *Journal of Optics B: Quantum and Semiclassical Optics* (2003), vol. 5(2). doi: `10.1088/1464-4266/5/2/376`.

119. K. B. Davis, M.-O. Mewes, M. A. Joffe, M. R. Andrews, and W. Ketterle: 'Evaporative Cooling of Sodium Atoms'. *Phys. Rev. Lett.* (1995), vol. 75. doi: `10.1103/PhysRevLett.75.2909`.

120. W. Ketterle and N. V. Druten: ‘Evaporative Cooling of Trapped Atoms’. Ed. by B. Bederson and H. Walther. Vol. 37. Advances In Atomic, Molecular, and Optical Physics. 1996. doi: `https://doi.org/10.1016/S1049-250X(08)60101-9`.

121. A. Ashkin, J. M. Dziedzic, J. E. Bjorkholm, and S. Chu: ‘Observation of a single-beam gradient force optical trap for dielectric particles’. *Opt. Lett.* (1986), vol. 11(5). doi: `10.1364/OL.11.000288`.

122. R. Grimm, M. Weidemüller, and Y. B. Ovchinnikov: ‘Optical Dipole Traps for Neutral Atoms’. Ed. by B. Bederson and H. Walther. Vol. 42. Advances In Atomic, Molecular, and Optical Physics. 2000. doi: `https://doi.org/10.1016/S1049-250X(08)60186-X`.

123. Z.-Y. Ma, C. J. Foot, and S. L. Cornish: ‘Optimized evaporative cooling using a dimple potential: an efficient route to Bose–Einstein condensation’. *Journal of Physics B: Atomic, Molecular and Optical Physics* (2004), vol. 37(15). doi: `10.1088/0953-4075/37/15/013`.

124. P. W. H. Pinkse, A. Mosk, M. Weidemüller, M. W. Reynolds, T. W. Hijmans, and J. T. M. Walraven: ‘Adiabatically Changing the Phase-Space Density of a Trapped Bose Gas’. *Phys. Rev. Lett.* (1997), vol. 78. doi: `10.1103/PhysRevLett.78.990`.

125. D. M. Stamper-Kurn, H.-J. Miesner, A. P. Chikkatur, S. Inouye, J. Stenger, and W. Ketterle: ‘Reversible Formation of a Bose-Einstein Condensate’. *Phys. Rev. Lett.* (1998), vol. 81. doi: `10.1103/PhysRevLett.81.2194`.

126. D. Jacob, E. Mimoun, L. D. Sarlo, M. Weitz, J. Dalibard, and F. Gerbier: ‘Production of sodium Bose–Einstein condensates in an optical dimple trap’. *New Journal of Physics* (2011), vol. 13(6). doi: `10.1088/1367-2630/13/6/065022`.

127. S. P. Ram, S. R. Mishra, S. K. Tiwari, and H. S. Rawat: ‘Temperature and phase-space density of a cold atom cloud in a quadrupole magnetic trap’. *Journal of the Korean Physical Society* (2014), vol. 65(4). doi: `10.3938/jkps.65.462`.

128. F. Dalfovo, S. Giorgini, L. P. Pitaevskii, and S. Stringari: ‘Theory of Bose-Einstein condensation in trapped gases’. *Rev. Mod. Phys.* (1999), vol. 71. doi: `10.1103/RevModPhys.71.463`.

129. J. Szczepkowski, R. Gartman, M. Witkowski, L. Tracewski, M. Zawada, and W. Gawlik: ‘Analysis and calibration of absorptive images of Bose–Einstein condensate at nonzero temperatures’. *Review of Scientific Instruments* (2009), vol. 80(5). doi: `10.1063/1.3125051`.

130. S. K. Ruddell, D. H. White, A. Ullah, D. Baillie, and M. D. Hoogerland: ‘Calorimetry of a harmonically trapped Bose gas’. *Phys. Rev. A* (2015), vol. 92. doi: `10.1103/PhysRevA.92.063622`.

131. D. Hume, I. Stroescu, M. Joos, W. Muessel, H. Strobel, and M. Oberthaler: ‘Accurate Atom Counting in Mesoscopic Ensembles’. *Physical Review Letters* (2013), vol. 111(25). doi: `10.1103/PhysRevLett.111.253001`.

132. I. Stroescu: 'Dissipative Double-Well Potential: Mesoscopic Atom Number Detection and Cold Atom Dynamics'. PhD thesis. Ruprecht-Karls-Universität Heidelberg, (2014).

133. A. Hüper, C. Pür, M. Hetzel, J. Geng, J. Peise, I. Kruse, M. Kristensen, W. Ertmer, J. Arlt, and C. Klempt: 'Number-resolved preparation of mesoscopic atomic ensembles'. *New Journal of Physics* (2021), vol. 23(11). doi: `10.1088/1367-2630/abd058`.

134. A. Abramovici and J. Chapsky: *Feedback Control Systems: A Fast-Track Guide for Scientists and Engineers.* (2000).

135. L. Turner, K. Weber, C. Hawthorn, and R. Scholten: 'Frequency noise characterisation of narrow linewidth diode lasers'. *Optics Communications* (2002), vol. 201(4). doi: `https://doi.org/10.1016/S0030-4018(01)01689-3`.

136. Y. Salvadé and R. Dändliker: 'Limitations of interferometry due to the flicker noise of laser diodes'. *J. Opt. Soc. Am. A* (2000), vol. 17(5). doi: `10.1364/JOSAA.17.000927`.

137. T. P. Dinneen, C. D. Wallace, and P. L. Gould: 'Narrow linewidth, highly stable, tunable diode laser system'. *Optics Communications* (1992), vol. 92(4). doi: `https://doi.org/10.1016/0030-4018(92)90636-6`.

138. A. Hemmerich, D. McIntyre, D. Schropp, D. Meschede, and T. Hänsch: 'Optically stabilized narrow linewidth semiconductor laser for high resolution spectroscopy'. *Optics Communications* (1990), vol. 75(2). doi: `https://doi.org/10.1016/0030-4018(90)90239-P`.

139. R. K. Raj, D. Bloch, J. J. Snyder, G. Camy, and M. Ducloy: 'High-Frequency Optically Heterodyned Saturation Spectroscopy Via Resonant Degenerate Four-Wave Mixing'. *Physical Review Letters* (1980), vol. 44(19). Publisher: American Physical Society. doi: `10.1103/PhysRevLett.44.1251`.

140. J. J. Snyder, R. K. Raj, D. Bloch, and M. Ducloy: 'High-sensitivity nonlinear spectroscopy using a frequency-offset pump'. *Optics Letters* (1980), vol. 5(4). Publisher: Optical Society of America. doi: `10.1364/OL.5.000163`.

141. J. H. Shirley: 'Modulation transfer processes in optical heterodyne saturation spectroscopy'. *Opt. Lett.* (1982), vol. 7(11). doi: `10.1364/OL.7.000537`.

142. I. Geisel, K. Cordes, J. Mahnke, S. Jöllenbeck, J. Ostermann, J. Arlt, W. Ertmer, and C. Klempt: 'Evolutionary optimization of an experimental apparatus'. *Appl. Phys. Lett.* (2013), vol. 102(21). doi: `10.1063/1.4808213`.

143. R. M. Storn and K. Price: 'Differential Evolution - A Simple and Efficient Heuristic for global Optimization over Continuous Spaces'. *Journal of Global Optimization* (1997), vol. 11(4). doi: `10.1023/A:1008202821328`.

144. K. Price, R. M. Storn, and J. A. Lampinen: *Differential Evolution, A Practical Approach to Global Optimization.* Natural Computing Series. (2005).

145. I. Stroescu, D. B. Hume, and M. K. Oberthaler: ‘Double-Well Atom Trap for Fluorescence Detection at the Heisenberg Limit’. *Physical Review A* (2015), vol. 91(1). doi: `10.1103/PhysRevA.91.013412`.

146. A. Qu, B. Evrard, J. Dalibard, and F. Gerbier: ‘Probing Spin Correlations in a Bose-Einstein Condensate Near the Single-Atom Level’. *Phys. Rev. Lett.* (2020), vol. 125. doi: `10.1103/PhysRevLett.125.033401`.

List of Figures

1.1 Overview of experimentally demonstrated BEC production times. 3

2.1 Experimental concept 6
2.2 Ultrahigh vacuum system 9
2.3 Two-chamber setup 9
2.4 $2D^+$-MOT coil setup. 11
2.5 Coil system assembly 12
2.6 Energy level diagram of the ^{87}Rb D_2 line transition 14
2.7 Layout of the ECDL system 16
2.8 Schematic diagram of the microwave setup. 18
2.9 Detection system. 19

3.1 Principle of magneto-optical trapping. 24
3.2 $2D^+$-MOT setup. 25
3.3 3D-MOT setup. 28
3.4 3D-MOT loading rates and atom numbers for a pulsed dispenser operation. 30
3.5 3D-MOT loading rates and saturated atom numbers for different dispenser operations. 31
3.6 3D-MOT loading rates and atom numbers for a continuous dispenser operation. 31
3.7 2D-MOT frequency detuning. 32
3.8 Magnetic potential for different Zeeman states. 34
3.9 Optical molasses temperatures. 35
3.10 Optical pumping scheme. 36
3.11 MOT, optical molasses and QPT positions. 38
3.12 QPT temperature. 38
3.13 QPT lifetime. 39
3.14 Forced RF evaporation scheme. 40
3.15 Optical dipole trap setup 43
3.16 cODT loading. 45
3.17 Ramping profiles during the transfer and evaporation in the cODT. 46
3.18 Evaporation in a harmonic optical dipole potential. 47
3.19 cODT vertical trap frequency. 48
3.20 Phase space density. 49
3.21 Sequential time evolution of the atomic cloud size and shape. 51
3.22 Bimodal fits. 52

3.23 Total atom number and temperature measurement. 53
3.24 BEC fraction and PSD. 54

4.1 Fluorescence image acquisition. 57
4.2 Time trace of detected atom numbers. 58
4.3 Number-resolved single-atom detection. 59
4.4 Atom number stabilization 62
4.5 Histogram of the detected signal for the total data set of the stabilization run. 62
4.6 Loss characterization and stabilization result. 64

5.1 Detection MOT setup on the optics table. 68
5.2 Detection MOT beam outcouplers. 70
5.3 Detection MOT setup on the vacuum table. 71
5.4 Intensity stabilization block diagram. 73
5.5 VCA and AOM nonlinearity. 74
5.6 VCA array setup. 74
5.7 Bode diagrams of the open-loop transfer function. 76
5.8 Bode diagram of the maximum noise suppression. 76
5.9 Frequency stabilization block diagram. 78
5.10 MTS setup. 80
5.11 MTS sensor signal processing. 82
5.12 MTS error signal & frequency stability. 83
5.13 Relative scattering noise. 84
5.14 Single-atom counting data with the second-generation detection setup. . . . 85
5.15 Background signal characterization for large atom number statistics. 86
5.16 Single-atom counting data with the second-generation detection setup and improved position stability. 87
5.17 Background signal characterization for small atom number statistics. 88
5.18 Standard deviation of the atom number distributions. 89

A.1 Timing sequence for the preparation of a ^{87}Rb BEC. 113
A.2 Four-wave mixing resonances. 114
A.3 Single-atom counting scaling. 114
A.4 PID schematics 115
A.5 Six-way intensity stabilization schematics 116
A.6 PID schematics 117

List of Tables

1.1 Overview of experimentally achieved interferometric phase sensitivity 3

2.1 ECDL system parameters 15

3.1 QPT evaporation ramp parameters. 41
3.2 cODT evaporation ramp parameters. 46
3.3 cODT evaporation parameters of the last evaporation step. 50

A Appendix

A.1 Summary of the BEC preparation sequence

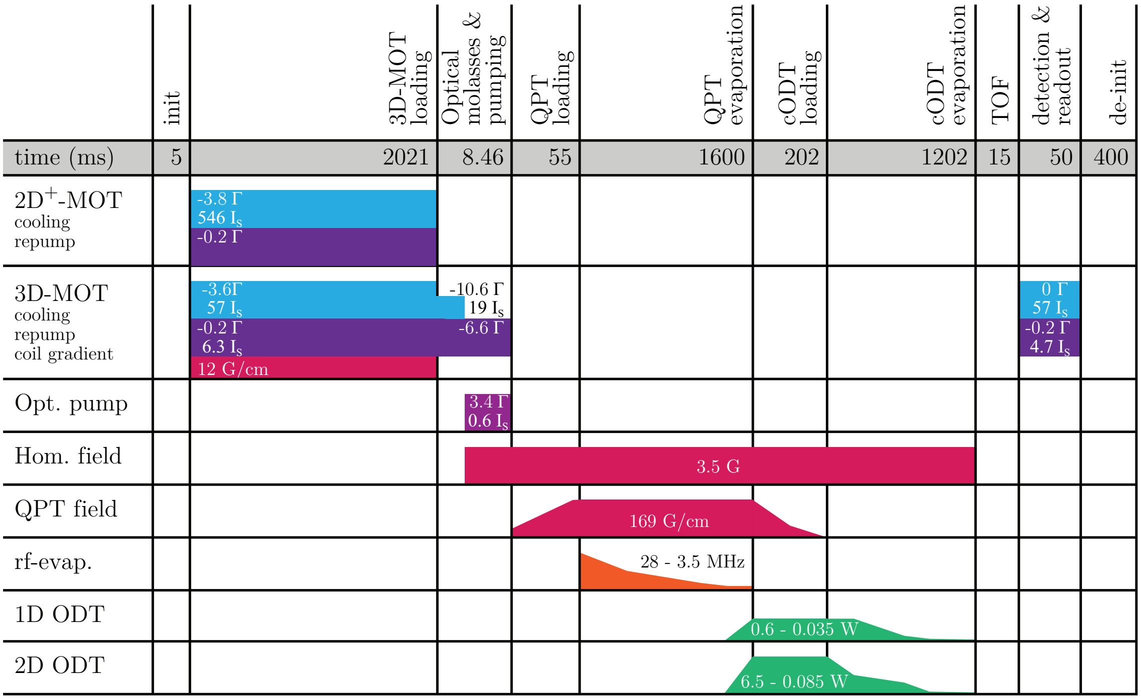
init
3D-MOT loading
Optical molasses & pumping
QPT loading
QPT evaporation
cODT loading
cODT evaporation
TOF
detection & readout
de-init
time (ms)
5
2021
8.46
55
1600
202
1202
15
50
400
2D$^+$-MOT
cooling
repump
-3.8 Γ
546 I$_s$
-0.2 Γ
3D-MOT
cooling
repump
coil gradient
-3.6Γ
57 I$_s$
-0.2 Γ
6.3 I$_s$
12 G/cm
-10.6 Γ
19 I$_s$
-6.6 Γ
0 Γ
57 I$_s$
-0.2 Γ
4.7 I$_s$
Opt. pump
3.4 Γ
0.6 I$_s$
Hom. field
3.5 G
QPT field
169 G/cm
rf-evap.
28 - 3.5 MHz
1D ODT
0.6 - 0.035 W
2D ODT
6.5 - 0.085 W

Figure A.1: Timing sequence for the preparation of a ^{87}Rb BEC. The schematic state diagram shows the timeline for the different steps of a single BEC cycle. The experimental sequence is divided into contextual chapters (top row), whereas the experimental parameters are listed in the first column. The second row shows the time (in milliseconds) needed for each chapter. The sequence is always initialized and deinitialized by setting all paramters to default values. The sequence starts with loading rubidium atoms from the 2D$^+$-MOT into the 3D-MOT. Both are operated on the $5^2\mathrm{S}_{1/2}$ to $5^2\mathrm{P}_{3/2}$ transition at 780 nm with a natural linewidth of $\Gamma = 2\pi \times 6.067\,\mathrm{MHz}$ and a saturation intensity of $I_s = 3.576\,\mathrm{mW/cm^2}$. The 2D$^+$- and 3D-MOT cooling and repump beams are detuned from the $F = 2$ to $F' = 3$ and from the $F = 2$ to $F' = 2$ as shown respectively. After the 3D-MOT loading, the atoms are prepared for optimal loading into the QPT by applying an optical molasses followed by an optical pumping pulse, which allows to transfer atoms into the magnetically sensitive $F = 2$ and $m_F = 2$ state. In the QPT the atoms undergoe an initial forced RF evaporation of 1.6 s by three RF power ramps, after which they are adiabatically loaded into a cODT. The cODT is formed by two far red-detuned 1064 nm beams with 70 nm and 35 nm waist sizes. The second evaporation step is realized by six subsequent ramps of the optical powers to final values of 85 mW and 35 mW, respectively. The atoms are finally released from the trap and detected by a resonant fluorescence pulse. The overall cycle time for the generation of a BEC takes 5.6 s.

A.2 Four-wave mixing resonances

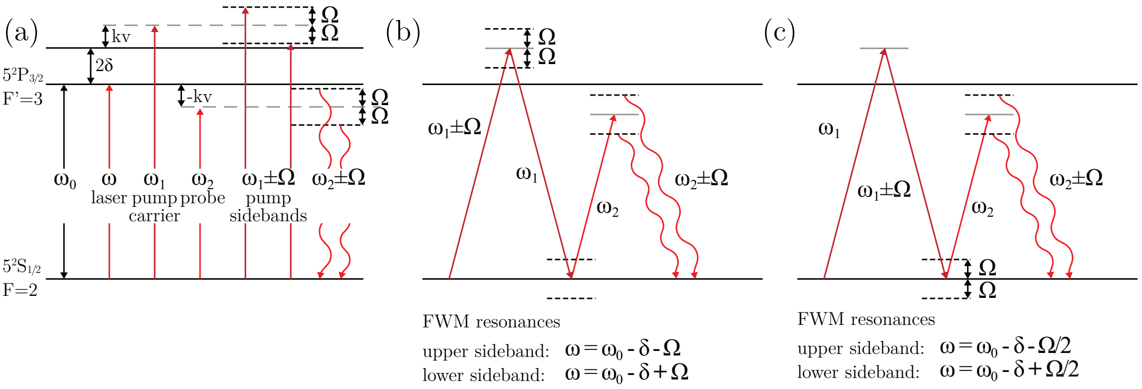
(a)
kv
2δ
$5^2P_{3/2}$
F'=3
-kv
Ω
Ω
Ω
Ω
ω_0
ω
laser
ω_1
pump
carrier
ω_2
probe
$\omega_1 \pm \Omega$
pump
sidebands
$\omega_2 \pm \Omega$
$5^2S_{1/2}$
F=2
(b)
Ω
Ω
$\omega_1 \pm \Omega$
ω_1
ω_2
$\omega_2 \pm \Omega$
FWM resonances
upper sideband: $\omega = \omega_0 - \delta - \Omega$
lower sideband: $\omega = \omega_0 - \delta + \Omega$
(c)
ω_1
$\omega_1 \pm \Omega$
ω_2
$\omega_2 \pm \Omega$
Ω
Ω
FWM resonances
upper sideband: $\omega = \omega_0 - \delta - \Omega/2$
lower sideband: $\omega = \omega_0 - \delta + \Omega/2$

Figure A.2: Four-wave mixing resonances. (a) Overview of the involved frequencies in the four-wave mixing process: ω_0 is the atomic resonance frequency, $\omega_1 = \omega + 2\delta$ is the pump carrier frequency, δ is the center frequency of the AOM, kv is the Doppler shift and Ω is the modulation frequency. All frequencies are shifted with respect to the resonance transition. (b,c) Upper and lower probe sidebands generated by the one and three photon resonance conditions. The first incident and the sum of the first three photons must be equal to the resonance frequency.

A.3 Single-atom counting measurement scaling

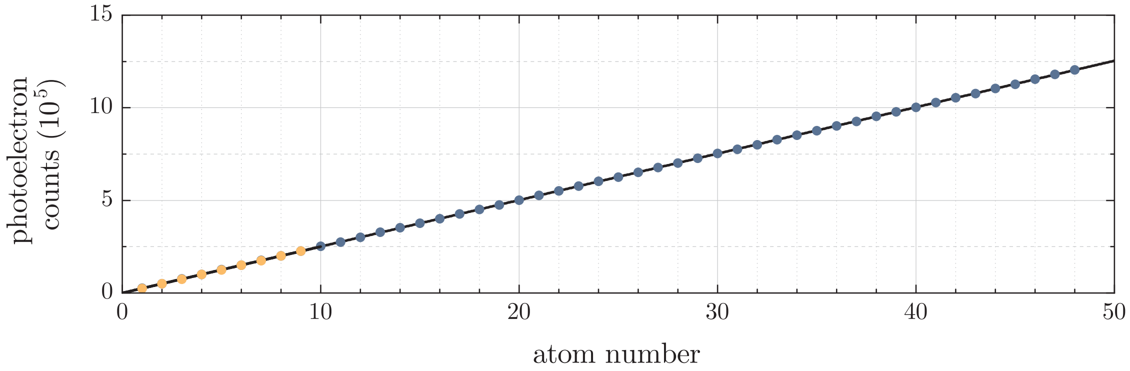

Figure A.3: Single-atom counting scaling. Calibrated scaling of the single-atom counting measurements described in Section 5.4. The blue and orange data points correspond to the first and second measurements, respectively.

A.4 Photodiode schematics

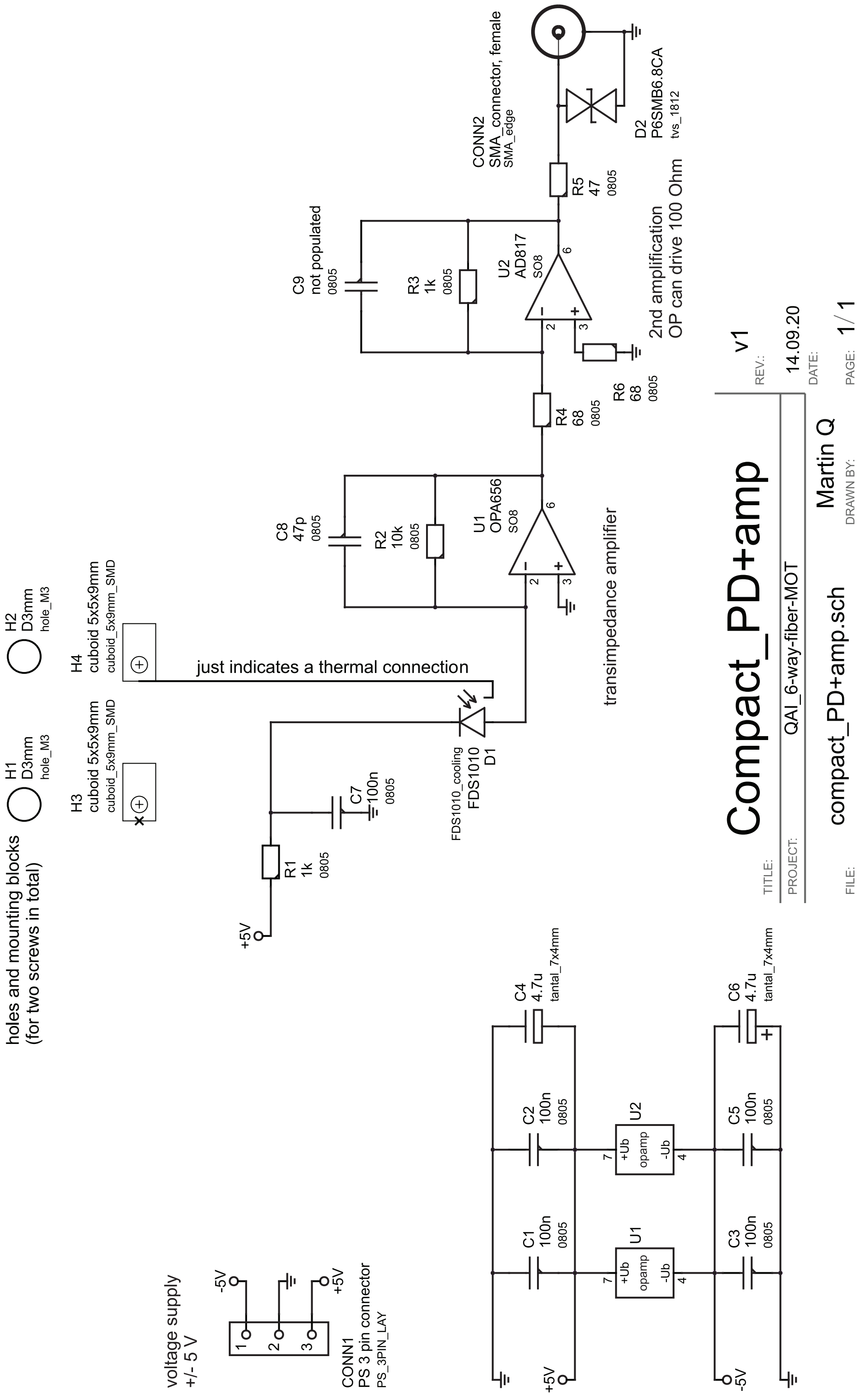
holes and mounting blocks
(for two screws in total)
H1
D3mm
hole_M3
H2
D3mm
hole_M3
H3
cuboid 5x5x9mm
cuboid_5x9mm_SMD
H4
cuboid 5x5x9mm
cuboid_5x9mm_SMD
just indicates a thermal connection
+5V
R1
1k
0805
C7
100n
0805
FDS1010_cooling
FDS1010
D1
C8
47p
0805
R2
10k
0805
U1
OPA656
SO8
2
3
6
transimpedance amplifier
R4
68
0805
C9
not populated
0805
R3
1k
0805
U2
AD817
SO8
2
3
6
R6
68
0805
2nd amplification
OP can drive 100 Ohm
R5
47
0805
CONN2
SMA_connector, female
SMA_edge
D2
P6SMB6.8CA
tvs_1812
TITLE:
Compact_PD+amp
REV.:
v1
PROJECT:
QAI_6-way-fiber-MOT
DATE:
14.09.20
FILE:
compact_PD+amp.sch
DRAWN BY:
Martin Q
PAGE:
1/1
voltage supply
+/- 5 V
-5V
+5V
1
2
3
CONN1
PS 3 pin connector
PS_3PIN_LAY
+5V
-5V
C1
100n
0805
C2
100n
0805
C4
4.7u
tantal_7x4mm
U1
U2
7
+Ub
opamp
-Ub
4
C3
100n
0805
C5
100n
0805
C6
4.7u
tantal_7x4mm

Figure A.4: PID schematics

A.5 Six-way intensity stabilization schematics

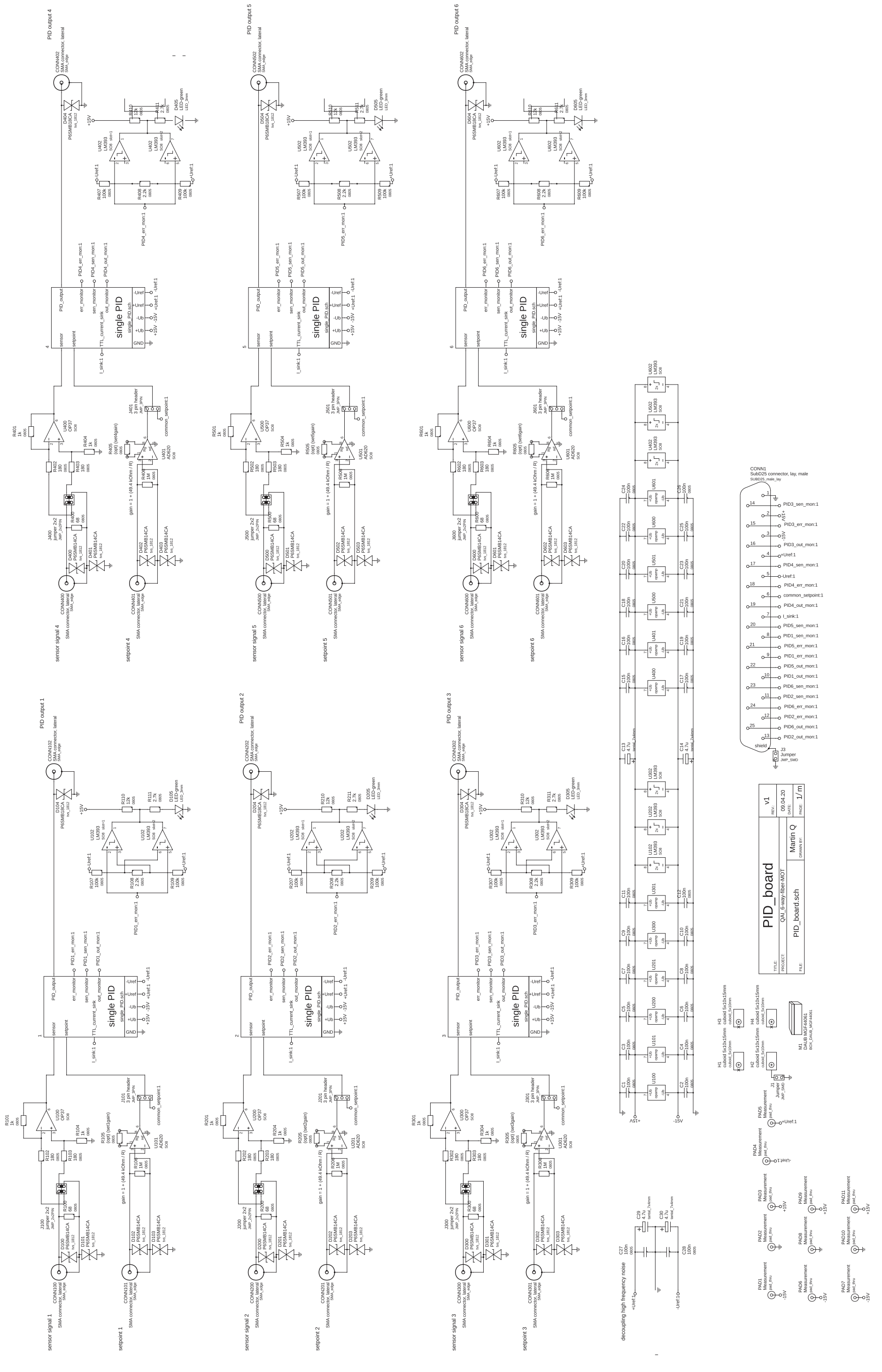

Figure A.5: Six-way intensity stabilization schematics

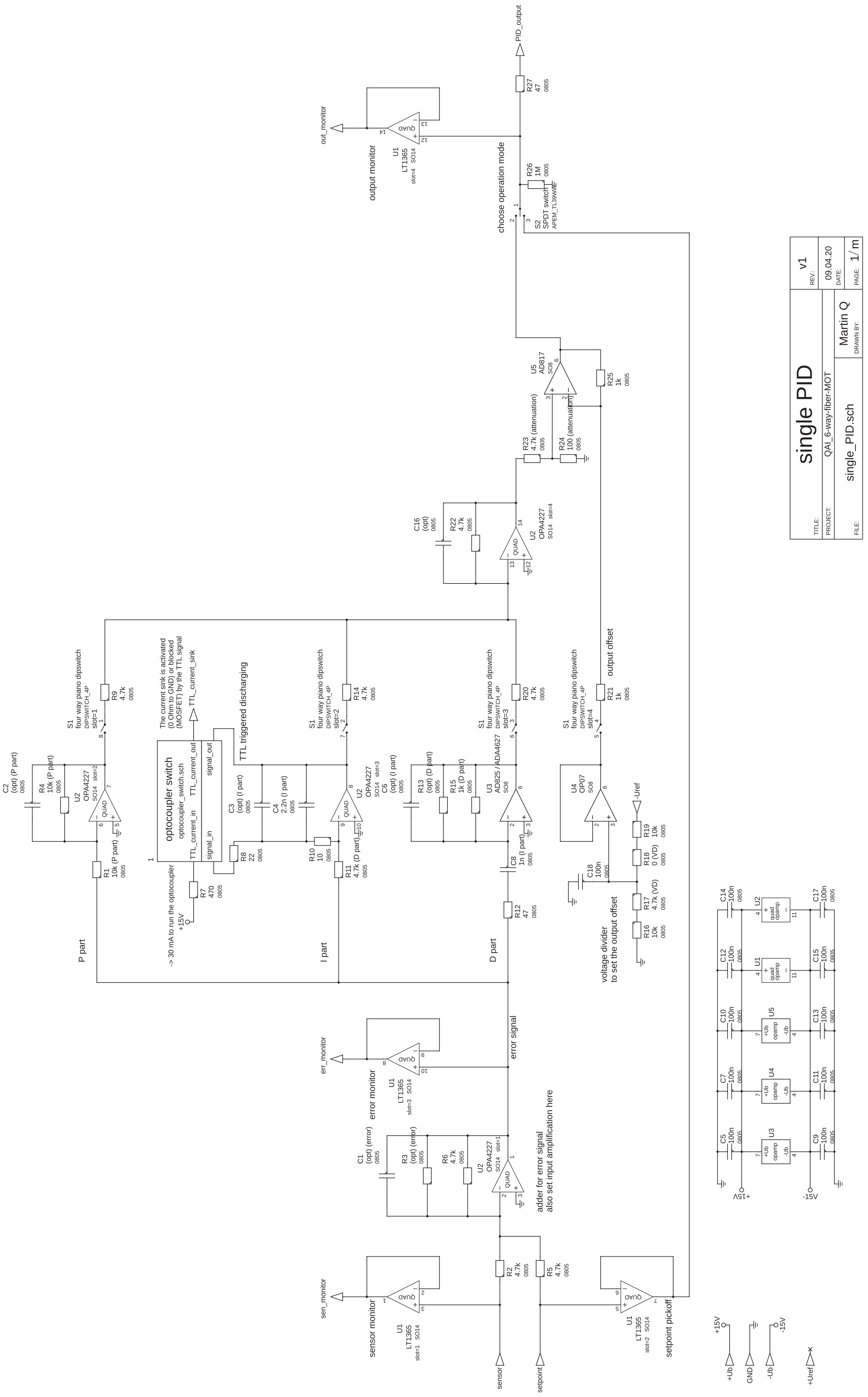
single PID
TITLE:
PROJECT: QAI_6-way-fiber-MOT
FILE: single_PID.sch
REV: v1
DATE: 09.04.20
DRAWN BY: Martin Q
PAGE: 1/ m
sensor
setpoint
sensor monitor
sen_monitor
setpoint pickoff
adder for error signal
also set input amplification here
error monitor
err_monitor
error signal
P part
I part
D part
optocoupler switch
optocoupler_switch.sch
TTL_current_in
TTL_current_out
signal_in
signal_out
TTL_current_sink
TTL triggered discharging
The current sink is activated
(0 Ohm to GND) or blocked
(MOSFET) by the TTL signal
-> 30 mA to run the optocoupler
+15V
four way piano dipswitch
DIPSWITCH_4P
output offset
voltage divider
to set the output offset
-Uref
choose operation mode
SPDT switch
output monitor
out_monitor
PID_output
U1 LT1365 SO14
U2 OPA4227 SO14
U3 AD825 / ADA4627 SO8
U4 OP07 SO8
U5 AD817 SO8
QUAD
+Ub
GND
-Ub
+Uref
+15V
-15V

Figure A.6: PID schematics

List of publications

1. M. Hetzel, L. Pezzè, C. Pür, M. Quensen, A. Hüper, J. Geng, J. Kruse, L. Santos, W. Ertmer, A. Smerzi, and C. Klempt: 'Tomography of a number-resolving detector by reconstruction of an atomic many-body quantum state'. *arXiv:2207.01270 [quant-ph]* (2022), vol. doi: `10.48550/arXiv.2207.01270`.
2. A. Hüper, C. Pür, M. Hetzel, J. Geng, J. Peise, I. Kruse, M. A. Kristensen, W. Ertmer, J. Arlt, and C. Klempt: 'Number-resolved preparation of mesoscopic atomic ensembles'. *New Journal of Physics* (2021), vol. 23. doi: `https://doi.org/10.1088/1367-2630/abd058`.

Curriculum Vitae

Personal Details

Name	Cebrail Pür
Date of birth	June 7, 1989
Place of birth	Dortmund, Germany

Education

06/2016-03/2022	Doctoral studies at Institut für Quantenoptik, Gottfried Wilhelm Leibniz Universität Hannover
10/2012-02/2016	Master's studies at Kirchhoff-Institut für Physik, Ruprecht-Karls-Universität Heidelberg
10/2008-09/2012	Bachelor's studies at Technische Universität Dortmund
06/2008	Abitur at Max-Planck-Gymnasium, Dortmund

Danksagung

Ich möchte mich bei allen Menschen für die vielfältige Unterstützung, die mir während meiner Doktorandenzeit und zum Gelingen dieser Arbeit zuteil wurde, ganz herzlich bedanken.

Ich bedanke mich bei meinem Doktorvater Herrn apl. Prof. Dr. Carsten Klempt, der mich herzlich in seine Arbeitsgruppe aufgenommen hat und mir die Möglichkeit gab meine Doktorarbeit in diesem faszinierenden Gebiet der Physik anzufertigen.

Ich danke auch Herrn Prof. Dr. Jan Arlt und Herrn Dr. Dennis Schlippert für die Übernahme der Koreferate. Herrn Prof. Dr. Luis Santos danke ich für die Übernahme des Prüfungsvorsitzes.

Besonders möchte ich mich bei meinem Kollegium, Büro- und Laborfreunden Mareike Hetzel und Martin Quensen für die gemeinsame Arbeit und ihre tatkräftige Unterstützung bedanken. Insbesondere möchte ich Dr. Andreas Hüper für seine stetige Ansprechbarkeit und große Hilfsbereitschaft, die für mich äußerst wertvoll gewesen ist, bedanken. Fabian Anders, Alexander Idel und Bernd Meyer möchte ich ebenfalls für den Austausch von Ideen und die wertvolle Zusammenarbeit bedanken.

Ich möchte auch meinen herzlichsten Dank an die Sekretärinnen aussprechen, ganz besonders Frau Ohlendorf, die meinen Promotionsablauf organisiert und unterstützt hat. Nicht zu vergessen an Frau Faber und an Frau Hünitzsch, die immer offen für Fragen und Probleme gewesen sind. Selbstverständlich auch an Frau Kaisik und an Frau Miltsch, die immer versuchen alles möglich zu machen.

Ein großes Dankeschön möchte ich dem Team der Feinmechanikwerkstatt schenken, insbesondere an Alexander Vocino, dessen Hilfsbereitschaft einen großen Beitrag zum Gelingen der Faser-MOT Kollimatorhalter geleistet hat.

Ich danke meinen Freunden aus dem Studium der Physik Hüseyin Vural, Ömer Bayraktar und Lukas Eisemann.

Ein besonderer Dank gilt meinen Eltern und Geschwistern, die mir all die Zeit die höchste Geduld und Liebe entgegengebracht haben.

Mein größter Dank gilt meiner wundervollen Ehefrau Aysun. Ich danke für Deine Geduld und Dein Verständnis für mich.

Erklärung der Selbstständigkeit

Hiermit erkläre ich, dass ich die vorliegende Arbeit selbstständig und nur unter Benutzung der angegebenen Literatur und Hilsfmittel angefertigt habe. Jeder Inhalt, der dem Wortlaut oder sinngemäß anderen Werken entnommen wurde, ist durch Angabe der Quelle als Entlehnung kenntlich gemacht. Die Arbeit hat in gleicher oder ähnlicher Form noch keiner Prüfungsbehörde vorgelegen.

Hannover, 14.01.2022

Cebrail Pür